Bimetal Temperature Compensation for Waveguide Microwave Filters

by

Brian F. Keats

A thesis
presented to the University of Waterloo
in fulfilment of the
thesis requirement for the degree of
Doctor of Philosophy
in
Electrical and Computer Engineering

Waterloo, Ontario, Canada, 2007

Abstract

Microwave communication devices have become ubiquitous in the past decade. As an increasing number of systems compete for spectrum, guard bands have shrunk to increase bandwidth efficiency. The frequency behaviour of microwave devices is affected by thermal expansion. In order to avoid interference with adjacent bands, microwave components must exhibit high temperature-stability in most communications applications.

Thermally stable materials can be used to construct temperature-stable components. However, this approach requires an expensive mass and cost trade-off. Temperature compensated aluminum resonators and filters provide major advantages in cost and mass. This work proposes that a compensating tuning screw with a temperature-dependent effective length be constructed by mounting a bimetallic compensator at the end of a mounting screw. This so-called *bimetal tuning-screw* can be used to produce temperature-compensated resonators and filters.

There are several advantages to this approach. Compensation can be tuned by adjusting the depth of the bimetal, simply by adjusting the mounting screw. Since there are no moving parts inside the cavity or filter, and the bimetal can be plated, there are no additional sources of passive intermodulation. Also, this design is simple to implement for waveguide designs in general.

In order to compensate for temperature drift, it is useful to quantify uncompensated drift. Temperature drift for a lossless linearly expanding RF component is derived from Maxwell's equations. For the lossy case, it is demonstrated that the resulting formula is approximately true, and that the quality of this approximation is excellent for practical levels of temperature range and thermal expansion.

Experimental results are provided that demonstrate bimetal compensation under uniform-temperature conditions for a single aluminum resonator. Measured drift of the compensated resonator is -0.38 ppm$/°\mathrm{C}$, compared to -23 ppm$/°\mathrm{C}$ for an uncompensated resonator. Measured drift for a bimetal-compensated 4-pole filter prototype is 2.35 ppm$/°\mathrm{C}$. A method for adjusting compensation for a filter is also provided.

Multiphysics simulations are used to examine power handling for bimetal-compensated filters. It is demonstrated that power-handling can be improved by reducing the effective length of the compensator to improve heat conduction to the cavity or filter.

Acknowledgements

I would like to take this opportunity to than Rob Gorbet and Raafat Mansour whose guidance and criticism have made every part of this research better. I would also like to thank my wife Margie whose love and support have been invaluable and apparently boundless.

Contents

List of Figures

List of Tables

Chapter 1

Introduction

The theoretical foundations for microwave engineering were laid by scientists like Maxwell, Hertz, and Marconi over a hundred years ago. The first practical applications of microwave theory emerged during the Second World War with the advent of radar. Since that time, the number of microwave applications have grown dramatically [1].

Satellite communications were some of the first commercial radio frequency (RF) applications. In the late 1960s, the Intelsat I-III satellites were deployed providing the first voice communication satellites. Subsequent Intelsat satellites used a channelized architecture, which created a need for high-performance, temperature-stable filters and multiplexers [2].

RF filters can be realized by coupling resonators. The work studied in this thesis deals with coupled resonator filters. Cavity resonators for example, can be coupled to one another using irises to produce a filter.

There has recently been an unprecedented proliferation of microwave technology in many communications applications. Unused bandwidth between channels called guard bands have been consistently reduced in order to maximize usable bandwidth [3]. This trend has generally led to tighter design constraints as more devices compete for spectrum [4].

The properties and performance of an RF device are highly dependent on its dimensions, and RF properties such as permittivity. Due to thermal expansion, the dimensions of any device are to some extent dependent on temperature. The RF properties of many materials are also temperature sensitive. The performance of any RF device will therefore exhibit a certain amount of temperature dependence, or *temperature drift*.

Most, if not all RF devices are subjected to temperature variation. Heating and cooling is caused by factors such as resistive power dissipation, ambient temperature changes, and thermal radiation. These factors are common to nearly any RF design, from satellite applications, to cable television transmission stations. Therefore, minimizing or eliminating temperature drift is a major concern for the RF designer.

Temperature drift is typically addressed by constructing components from materials with a low coefficient of thermal expansion (CTE) such as Invar [2]. However, constructing a component from Invar is more costly than using aluminum, both in terms of material and machining costs.

A mass penalty is also incurred when using Invar over aluminum, which is especially costly in satellite applications. A $24\ \mathrm{kg}$ Invar multiplexer weighs $8\ \mathrm{kg}$ when constructed from aluminum. For launch costs of \$30,000 per kilogram, deploying this aluminum multiplexer would result in \$480,000 in launch-costs savings.

If the same mass savings is replaced with fuel, life-cycle savings can instead be realized. For a satellite requiring $25\ \mathrm{kg}$ of fuel each year with annual revenues of \$80 million, the $16\ \mathrm{kg}$ mass savings represented by the aluminum multiplexer described above results in \$51 million in extra revenue. For a satellite with a 15 year life cycle, this savings represents \$16 million in present value, assuming an 8% annual discount rate. This is the motivation for the research undertaken in this thesis.

1.1 Thesis Objectives and Contributions

The primary objective of this thesis is to devise an efficient mechanism for temperature compensation, and to design and build a temperature-compensated waveguide filter constructed primarily from aluminum using this mechanism. In the process of accomplishing this major objective, there are a number of secondary goals that this research aims to accomplish. These are as follows:

- This work aims to quantify the temperature drift problem as generally as possible. Where possible, drift will be derived from first principals. Otherwise, simulation methods will be developed capable of quantifying complex environmental and structural factors that contribute to temperature drift.

- The method chosen for temperature compensation must be implementable for waveguide designs in general. This will allow for implementation of temperature compensation in existing waveguide filter designs.

- The amount of temperature compensation must be adjustable. In microwave designs where device dimensions are on the order of wavelength, small dimensional changes cause significant changes in RF response. Adjustable compensation is therefore required to account for manufacturing tolerances.

- The effect of high-power on the compensated filter must be accounted for. This requires that possible sources of passive intermodulation be addressed. The effect of local resistive heating on filter response must be quantified and minimized.

In pursuing the objectives and goals listed above, a number of contributions to the art were realized. The contributions presented in this thesis and their potential impact are described below:

- This work proposes that a bimetallic compensator mounted on a screw can be used to provide temperature compensation for waveguide filters and resonators (Chapter 4). It is demonstrated that when using this approach, compensation can be easily adjusted by turning the mounting screw, thereby adjusting the depth of the compensator. This method is simple to implement for waveguide designs in general. Applying this approach to waveguide filters will allow aluminum filters to be used in applications where Invar waveguide filters are currently used. Experimental results are provided for a compensated resonator (Chapter 6) and a compensated filter (Chapter 7). These experiments demonstrate that a bimetal tuning screw can be used to produce aluminum resonators and filters that exhibit levels of temperature drift similar to or lower than their Invar equivalents. Application of this temperature compensation approach can lead to a substantial mass and cost savings over traditional Invar filters in many areas including satellite and terrestrial radio applications.

- A method for adjusting compensation for each resonator in a Chebyshev filter is provided. This method is appropriate for any compensated design where the amount of compensation is adjustable for each resonator. This contribution provides a useful tool for implementing either the compensation approach proposed here, or any other form of adjustable compensation.

- Three multiphysics models are proposed in this work (Section 8.1). (The term multiphysics refers to models that account for coupling between two or more domains; for example, mechanical and thermal.)
  - A uniform temperature mechanical-RF simulation is provided. This model is used to simulate temperature drift in situations where the temperature distribution is uniform. The resulting temperature drift is used as the baseline performance for a given design. This contribution allows for the design and simulation of complex temperature-compensation schemes using finite element analysis. This model can also be used to model temperature drift in uncompensated resonators and filters.
  - A resistive heating simulation is proposed that models local resistive heating, given the input power and thermal boundary conditions. This simulation can be used in in lieu of or as a precursor to high-power testing. This type of simulation is useful for any microwave structure designed for high-power use. It can be used to locate areas of high resistive-heating so that they can be addressed in the design.
  - A resistively heated thermal-mechanical simulation is proposed that models RF behaviour on the deformed geometry given input power and thermal boundary conditions. This model not only solves for resistive heating for given thermal boundary conditions, but also accounts for the effect of geometry deformation on filter response. This simulation can be used to model RF performance while accounting for general environmental conditions; this includes mounting constraints, thermal conditions, and resistive heating. In temperature compensated designs in particular, it can be used to quantify the effect of local resistive heating and environmental conditions on compensation.
- Temperature drift for an arbitrary microwave structure is derived from Maxwell's equations, assuming the structure is lossless and has a uniform coefficient of thermal expansion (Section 3.1). It is also shown that the same expression for temperature drift is approximately true for lossy structures (Section 3.2). The quality of this approximation is based

on the assumption that the coefficient of thermal expansion multiplied by the temperature change is much less than unity; a valid assumption for most practical systems. The accuracy of this expression is therefore not affected by the level of loss. This expression for temperature drift is general and that can be used to quantify temperature drift for any device made from a single material that is allowed to expand freely.

- An expression is derived for the drift of the coupling coefficient due to iris expansion for a thin iris (Section 3.3). By applying this drift to a lumped element filter model, it is shown that the drift caused by iris expansion is small when compared to overall filter drift, even for a well-compensated filter. It is demonstrated that the contribution of iris expansion to temperature drift is therefore insignificant.
- A parameterized model for bimetal actuation and thermal expansion is proposed that can be used to simply model a bimetal compensated device under uniform temperature conditions (Section 4.3). This model can be implemented using microwave simulation packages that allow for parameterization of geometry (e.g. Ansoft HFSS). This approach provides a alternative to full structural simulation where the temperature distribution is uniform and bimetal actuation is unloaded.

1.2 Thesis Organization

In Chapter 2, milestones in the development of microwave technology are described. The problem of passive intermodulation is discussed. A review of the literature in the area of temperature compensation of RF components is provided. A description of bimetal theory and the equations used to predict and specify bimetal behaviour is shown.

In Chapter 3, temperature drift of uncompensated components is described. Equations describing temperature drift for a lossless uncompensated device are derived from Maxwell's equations. It is demonstrated that this equation is approximately true for a lossy device. Simulations are provided to confirm that this approximation is valid for typical materials and temperatures. An expression is derived that predicts temperature drift of the coupling coefficient for a thin iris. The metrics and conventions used in this work to specify temperature drift are described. These metrics are classified with respect to thermal conditions.

Chapter 4 provides an overview of the bimetal tuning screw that is used to provide temperature compensation. Design requirements are presented, along with two configurations that meet these requirements. The susceptibility of a bimetal tuning screw to vibration is examined using a mechanical eigenmode simulation. Adjustability of temperature compensation is demonstrated in simulation. Finally, a parameterized model for bimetal-compensated components is provided.

An experimental setup capable of performing uniform ambient temperature tests is described in Chapter 5. Measurement procedures are described, designed to relieve residual strains in a component to ensure accurate data is collected.

Chapter 6 describes the implementation of bimetal compensation for a single aluminum resonator. A prototype resonator is described along with the procedure for fixturing and adjusting the compensation. Experimental results for the compensated resonator are provided, demonstrating the effectiveness of bimetal compensation.

Bimetal compensation is applied to a waveguide filter in Chapter 7. It is demonstrated in simulation that compensation is independent from resonant frequency tuning. A method for adjusting compensation is presented, along with a description of a prototype filter. Finally, experimental results for the compensated filter are provided.

In Chapter 8, a multiphysics simulation is described that can model compensation under uniform temperature conditions. An approach to modelling RF heating is described. Finally a model is provided that can quantify temperature drift given arbitrary thermal boundary conditions for lossy compensated components under high-power. The power handling capability of bimetal compensated filters is examined using these multiphysics simulations. These results are used to refine the design to improve performance of the lossy component under high-power.

Finally, conclusions and recommendations are provided in Chapter 9.

Chapter 2

Literature Review

In this chapter, milestones in the evolution of microwave technology are presented. A description of passive intermodulation (PIM) in communications systems is provided. With an understanding of the sources of passive intermodulation, care can be taken to avoid PIM when devising approaches to temperature compensation. Industry practice and research in the field of temperature compensation of RF filters and resonators is reviewed. A description of the general behaviour of bimetals along with a description of the equations that describe their actuation are provided.

2.1 Milestones in Microwave Technology

The fundamental concepts of microwave theory were discovered over 100 years ago by scientists like Maxwell, Hertz and Marconi [1]. Starting from Faraday's theories on lines of force, Maxwell eventually published what became eponymously known as the Maxwell equations in *A Treatise on Electricity and Magnetism*. This work implied the existence of electromagnetic waves travelling at the speed of light [5]. As well as being the first field equations, Maxwell's equations unified electricity and magnetism, and are the basis of microwave engineering.

World War II was a watershed for global technological innovation, and RF technology was no exception. Technological innovation was deemed a legitimate war front on all sides, and for the first time scientists were systematically recruited for the war effort. For these reasons, World War II has sometimes been referred to as the Physicists' War [6].

Emerging radar technology provided the prospect of detecting planes and ships at distances exceeding the limits of visibility. This attracted the interest of military researchers as early as the 1920s. In the late 1930s the first major radar installation, a network of radars called Chain Home, was constructed along the vulnerable southern and eastern English coast [6]. The advent of radar provided the first impetus for research and development in RF technology.

Radar applications required wide-band, tunable receiver-filters. Waveguide filters with inductive posts were developed to satisfy this need [2]. Waveguide filters are able to handle high transmission power, and exhibit a high quality factor (Q). These filters however are large when compared to TEM (transverse electric-magnetic) transmission line filters. Since wide bandwidth filters have inherently low loss, more compact TEM transmission line filters replaced inductive post waveguide filters for radar applications [2].

The most popular implementation of TEM transmission line filters are combline filters. These filters consist of an array of parallel coupled conductors mounted in a conducting cavity as shown in Figure 2.1 [7]. In fact, combline filters are still widely used in cellular radio base stations [2]. These filters are compact, have low loss, and provide good spurious response.

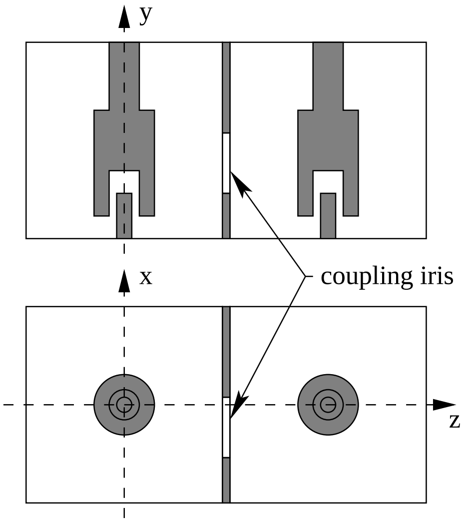

Figure 2.1: Diagram of a 2-pole combline filter, side and top view (input/output coupling not shown)

When radio was being developed in the 1890s, most physicists believed that radio waves could not travel long distances since they travel in straight lines. Guglielmo Marconi proved this notion wrong in 1894, but it was left to Arthur E. Kennelly and Oliver Heaviside to propose that the long radio waves used by Marconi were bouncing off an atmospheric layer of ions. When later proven to exist, this layer was named the ionosphere [8]. The concept of bouncing communications signals from earth to space foreshadowed the modern communications satellite where signals are relayed from earth to space and back to communicate over large distances.

Shorter-wave microwaves can support more bandwidth than the radio waves used in early wireless communication. However, the ionosphere is transparent to microwaves. Transmitting microwaves over long distances therefore requires either a series of relays, or another object in space to reflect the waves.

The first attempt to relay microwaves in space came in 1946 with Project Diana which succeeded in using the moon to reflect radio waves. In 1960, the US launched Echo I, the first satellite designed specifically for microwave communications. Echo I was a passive satellite, that simply reflected microwaves back to earth [9]. Subsequent communications satellites were active designs which filtered, mixed, amplified, and retransmitted the signal making Echo I both the first, and last passive communications satellite.

Satellite communications would develop into one of the first major civilian applications of microwave technology. The Telstar satellite, launched in 1962, was able to transmit telephone, facsimile, and television signals. Due to its low, (and therefore fast) orbit, Telstar was only able to transmit over 10 minute intervals while in sight of its three ground stations [9].

The early Intelsat satellites launched in the late 1960s proved the commercial viability of satellite voice communications. Intelsat I was the first geosynchronous satellite that orbited at the same period as the earth, and thus appeared stationary to base stations. Since geosynchronous orbit allows for unlimited transmission times, this has become the standard orbit for most communications satellites.

Intelsat IV was the first communications satellite to use a channelized architecture [2]. A typical channelized architecture is shown in Figure 2.2 [10]. At the satellite, the uplink signal is low-power due to atmospheric attenuation. The downlink signal however is amplified by the satellite and therefore high-power. In order to avoid interference, the uplink and downlink signals are transmitted on different bands. In this example, the 500 MHz uplink band ($5.925 - 6.425$ GHz)

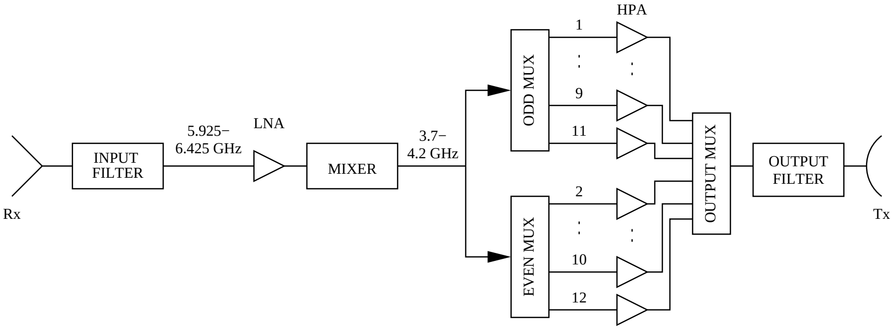

Figure 2.2: A typical satellite-communications architecture

is filtered and amplified using a low-noise amplifier (LNA). The input signal is then mixed down to the downlink band ($3.7 - 4.2$ GHz). An input multiplexer splits the signal into 36 MHz channels. Each channel is amplified using a high-power amplifier (HPA) and recombined. The filtered signal is sent to the downlink antenna [2].

Insertion loss of the input filter, output filter, and multiplexer must be minimized in order to maximize bandwidth efficiency for the satellite. Low-loss filters using iris-coupled Invar resonators were used to construct the uplink/downlink filters and multiplexers. A typical channel filter for an output multiplexer weighed close to 4 kg. The mass of these filters was later reduced using thin-walled Invar cavities [10].

The development of dual-mode filters in the 1970s proved to be a major advance for satellite communications [11, 12]. Dual-mode filters use perpendicular modes to allow a single physical cavity to function as two electrical cavities. A typical dual-mode in-line waveguide filter is shown in Figure 2.3.

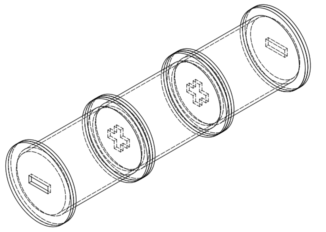

Figure 2.3: A dual-mode in-line waveguide filter

By halving the number of physical cavities, dual-mode filters provide a substantial mass and space savings. Dual-mode filters also allow coupling between non-adjacent cavities. This allows for simpler realization of more complex filter functions, which provides improved performance; specifically lower attenuation in the passband and improved selectivity [12].

Triple- and quadruple-mode resonators have also been produced. These designs have proven to be very sensitive to manufacturing tolerances and have shown poor thermal stability. Although triple-mode filters have been deployed in satellite multiplexers, filters employing more than three modes per cavity have not as yet been deployed [10].

Dielectric resonators provided another major advance in filter technology. Although work on dielectric resonators goes back to the 1930s, high performance thermally-stable dielectric materials were not available until the 1970s [13, 14]. Since electric fields are concentrated inside a dielectric, dielectric filters provided a mass and volume reduction. The dual-mode dielectric filter presented by Fiedziuszko [14] is an important example of dielectric filter advancement.

Many see high-temperature superconductive (HTS) designs as the next frontier in microwave filters [2]. A very small filter with near-infinite unloaded Q can be constructed from HTS, provided it is cooled cryogenically to $77\ \mathrm{K}$. Despite the gains in performance and space that HTS designs offer, concerns about the reliability and added complexity of cryogenic cooling has slowed implementation of these designs in space applications.

2.2 Passive Intermodulation

Linearity is a crucial property for wireless communication systems. It is linearity, and more specifically the superposition principle, that makes wireless communication possible. Superposition permits the combination and extraction of modulated communications channels.

Like most engineering assumptions, the linearity assumption often is not perfect. In some situations, nonlinearity is tolerable; for example, nonlinear amplification in frequency-modulated systems. In many situations however, nonlinearity can cause serious problems in communications systems.

When two or more signals are mixed in a nonlinear device, intermodulation products are produced. These intermodulation products are a problem when they occur within the passband of that system, or an adjacent system.

Intermodulation products occur in three main areas [15]. The inherent nonlinearity of power amplifiers and mixers results in intermodulation products at the transmitter and receiver input stages. In passive, nominally linear components, intermodulation is produced by nonlinear aspects such as, nonlinear metallic contacts, poor or corroded connections, and nonlinear materials. This is referred to as *passive intermodulation* (PIM). While the nonlinearities in the receiver and transmitter can be minimized by system isolation, this is not the case for intermodulation products in the passive components.

Dealing with passive intermodulation has been a problem in communications systems for nearly seventy years. The earliest reference available describing passive intermodulation is in the *RCA review* from 1937 [16].

PIM was first observed in space applications in the Lincoln Laboratories satellites LES-5 and LES-6 in the late 1960s [10]. When devising methods for temperature compensation, the problem of passive intermodulation must be considered. In order to address the temperature compensation problem without incurring passive nonlinearity, an understanding of the mechanisms of PIM is useful.

2.2.1 Intermodulation Theory

In order to understand the PIM problem, it is important to understand the basic mechanism of intermodulation.

In general, the transfer function of a nonlinear device can be written as a Taylor series [1].

$$v_{out} = a_0 + a_1 v_{in} + a_2 v_{in}^2 + a_3 v_{in}^3 + \cdots \tag{2.1}$$

This assumes a memoryless device.

The coefficients of the Taylor series a_n, depend on the properties of the nonlinear component. Consider the case where the input voltage can be represented by three sinusoids.

$$v_{in} = V_1 \cos(\omega_1 t) + V_2 \cos(\omega_2 t) + V_3 \cos(\omega_3 t) \tag{2.2}$$

For simplicity, consider only the first three terms of the nonlinear transfer function.

$$v_{out} = a_0 + a_1 v_{in} + a_2 v_{in}^2 \tag{2.3}$$

The output voltage can be determined by substituting Equation 2.2 into the simplified transfer function from Equation 2.3.

$$\begin{aligned} v_{out} &= a_0 + a_1(V_1 \cos\omega_1 t + V_2 \cos\omega_2 t + V_3 \cos\omega_3 t) + \\ &\quad a_2(V_1^2 \cos^2\omega_1 t + V_1 V_2 \cos\omega_1 t \cos\omega_2 t + V_1 V_3 \cos\omega_1 t \cos\omega_3 t + \\ &\quad V_1 V_2 \cos\omega_1 t \cos\omega_2 t + V_2^2 \cos^2\omega_2 t + V_2 V_3 \cos\omega_2 t \cos\omega_3 t + \\ &\quad V_1 V_3 \cos\omega_1 t \cos\omega_3 t + V_2 V_3 \cos\omega_2 t \cos\omega_3 t + V_3^2 \cos^2\omega_3 t) \end{aligned} \tag{2.4}$$

The higher-order sinusoidal terms from Equation 2.4 can be reduced to first order sinusoids using the following identities.

$$\begin{aligned} \cos A \cos B &= \frac{1}{2}\left(\cos(A-B) + \cos(A+B)\right) \\ \cos^2 A &= \frac{1}{2}\left(1 + \cos 2A\right) \end{aligned}$$

The intermodulation will therefore occur at the following frequencies.

$$f_{im} = mf_1 + nf_2 + pf_3 \tag{2.5}$$

where m and n and p are integers, and

$$\begin{gathered} |m| \leq 2, \\ |n| \leq 2, \\ |p| \leq 2, \\ (|m| + |n| + |p|) < 2 \end{gathered}$$

It can be shown that when all the terms in Equation 2.1 are considered, Equation 2.5 describes the intermodulation frequencies where m, n and p are any positive or negative integer. The sum $(|m| + |n| + |p|)$ defines the order of the intermodulation product [15].

This analysis can be generalized for a k^{th} order nonlinearity, with coefficients m_i. The order of intermodulation becomes [17].

$$N = \sum_{i=1}^{M} |m_i| \tag{2.6}$$

and the output frequencies are,

$$f_o = \sum_{i=1}^{M} m_i f_i \tag{2.7}$$

where m_i is the set of all positive and negative integers less than the order of nonlinearity.

This analysis can be used to determine the number of in-band intermodulation products. Figure 2.4 shows the number of in-band intermodulation products for orders of intermodulation from third to ninth, versus the number of channels.

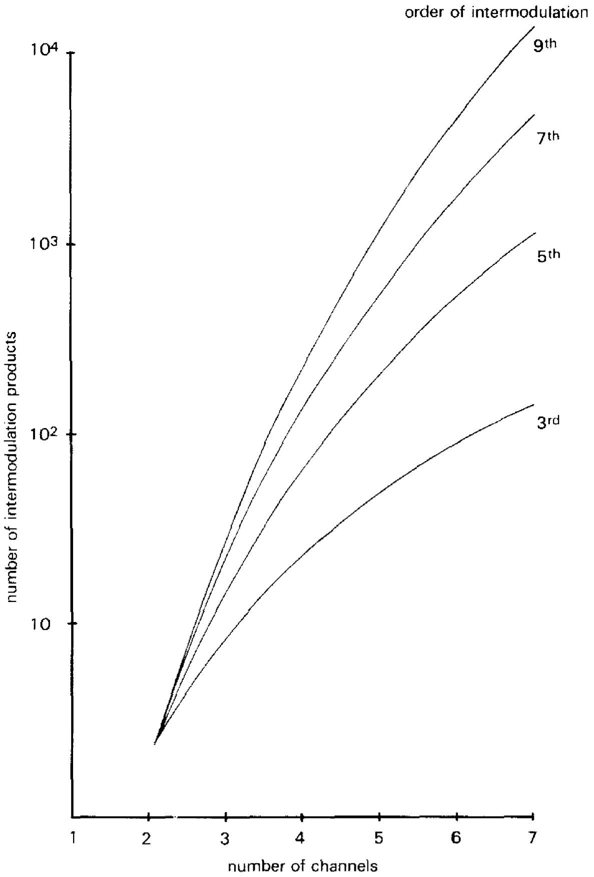

Figure 2.4: In-band intermodulation products [15]

2.2.2 Sources of Intermodulation

There are many potential sources of passive intermodulation. Identifying the source of PIM can be difficult. In an early description of intermodulation in the *RCA review*, a case was described where opening a window eliminated the intermodulation [16]. It is therefore important to recognize potential sources of PIM. The sources of PIM can generally be divided into two categories: contact nonlinearity, and material nonlinearity.

Contact Nonlinearity

It has long been understood that poor electrical contact between conductors can cause PIM [16]. In fact, this is the most common source of PIM in most applications [15]. There are a number of issues that can result in problems with electrical connections.

A poor mechanical interface will produce poor electrical connection. Excellent surface finish and workmanship for mating parts is required to ensure good electrical connection. When pieces are properly manufactured, a poor mechanical interface is still possible if assembly is not performed properly. For these reasons, stringent standards are in place for manufacturing and assembly of parts that are potential sources of PIM [2].

Thin oxide layers or corrosion can also cause poor contact between components. Oxide layers are present on the surface of most metals. This problem is more apparent in certain materials that corrode or oxidize easily. For example, a $10 - 100$Å thick aluminum-oxide layer will form spontaneously on a clean aluminum surface [17]. Electron tunnelling and semiconductor action through these oxide layers also causes nonlinearities where they are present at a connection.

PIM can also be caused by microscopic cracks on the surface of a material. Voltages across these cracks can result in currents that produce PIM [10]. These cracks can be caused by stressing the material.

Dirt and other contamination can also cause PIM [18]. This can be caused by hydrocarbons or flux on the surface of the conductor.

Material Nonlinearity

Material nonlinearity is a bulk material property that cannot generally be avoided except by avoiding nonlinear materials themselves.

Ferromagnetic materials and carbon fibres for example exhibit nonlinear electrical properties. Ferromagnetic nonlinearity is also hysteretic. This further complicates the PIM problem, since the standard Taylor series analysis of the PIM phenomenon assumes memoryless, and thus non-hysteretic nonlinearity.

Although many sources of PIM have been identified, it is important to note that the specifics of each mechanism, and indeed the mechanisms themselves are often not well understood [15].

2.2.3 Minimizing PIM

Addressing the PIM problem is complex. A large number of potential sources of PIM have been identified, and some of them are not well understood. General guidelines are required to deal with the various PIM sources at both the design and manufacturing stages.

- **Workmanship:** Workmanship may be the most important aspect of minimizing PIM. Precise mechanical tolerances must be adhered to. High quality surface finishes are required. During assembly, surfaces must be clean and free of debris. Contacts must be protected from corrosion and oxidation over their lifetime particularly for ground based applications [17].

- **Metal-to-metal contacts:** Contacts between metals, particularly dissimilar metals, must be minimized. This means that where possible, components should be constructed from a single piece [19]. Where metal-to-metal contacts between dissimilar metals cannot be avoided, an insulator or an alternative current path should be provided. Exposure of metal contacts to radiated signals must also be minimized.

- **Bolted joints:** The number of bolted joints must be reduced where possible. Where bolted joints are necessary, mating faces must be held together at high pressures, at least $70\mathrm{MPa}$ [19]. Pressure can break down the oxide layer on the mating face, which increases conduction and reduces PIM. In lieu of bolted joints, bonded joints should be used where possible.

- **Nonlinear materials:** Nonlinear materials must not be used near the current path. This excludes ferromagnetic materials, graphite, and plastics from current path applications

[15, 10]. In some cases, nonlinear materials coated with conducting materials are used. For example, in the 1970s conductor-coated graphite materials began to replace Invar as a waveguide structure [14, 20]. Since that time however Invar components have replaced graphites in most designs as Invar production techniques have advanced.

- **Cleanliness:** Great care must be taken to ensure that parts are clean [19]. It is good practice to clean parts immediately before assembly.
- **Current density:** Current densities must be minimized. This can be accomplished by increasing the contact area, and using larger conductors [15].
- **Thermal considerations:** Thermal expansion induces stress and strain to a structure. This can cause deflection at contact surfaces, which can cause nonlinearity. Temperature change, and in particular temperature gradients, must therefore be minimized [15].
- **Cavity perturbation:** Tuning screws in the current path can cause PIM, and should be avoided where possible. Where tuning screws are required, they must be tight [15]. Once tuning is completed, the tuning screw can be tensioned and epoxied in place, from outside the structure.
- **Connector cables:** Cable lengths should be minimized. Low PIM cables should always be used. Coaxial cables with steel conductors should be avoided. Minimize cable bending, particularly at the base of the connector [17].
- **Nonlinear components:** Nonlinear components should be avoided wherever possible. Components to be avoided in low-PIM applications include lumped dummy loads, circulators, isolators, and some semiconductor devices [15].
- **Isolation:** PIM from high-power transmit components interfering with low-power receive components is a common problem. The transmit and receive systems must be well isolated, either through filtering, or physical separation [15].
- **Frequency planning:** Intermodulation frequencies should be considered in the frequency planning stages. Even higher-order products can cause interference between transmit and receive systems due to high disparity in power levels [15].

2.2.4 Modelling PIM

Little work has been on modelling passive intermodulation. This is not surprising given that the causes of PIM are complex and poorly understood. Also, it is difficult to isolate a particular PIM source experimentally.

For the case of PIM at waveguide connections, Vicente recently reported a model for predicting PIM [21]. Surface roughness means that the contact between the waveguides is never perfect. The interface surface can be divided into metal contact zones (a-spots), and non-metal-contact zones. Furthermore, the oxides or sulphides that form on all metals mean that contact is further reduced.

Experimental work has shown that PIM tends to be relatively independent of clamping force up to a certain threshold, after which PIM drops off sharply. It has been postulated that this drop-off is associated with the rupture of the oxide layer.

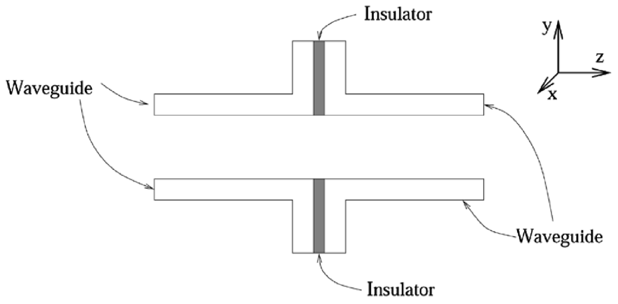

Figure 2.5: Side view of a waveguide connection. The dielectric connection is not to scale, and roughness is not shown. [21]

Figure 2.5 describes the system under consideration. The insulating dielectric (not to scale) describes the oxide layer.

Three steps are required to produce a PIM model. A surface model is used to calculate the contact area as a function of applied load. An electric contact model is proposed for contact described in the mechanical model. Finally, PIM excitation is applied.

Surface models generally assume that surface peaks, or asperities, are spherical and statistically distributed. The Greenwood and Williamson (GW) surface model was chosen for this study. This model assumes isotropy of the surface, uniform asperity density, and random asperity heights.

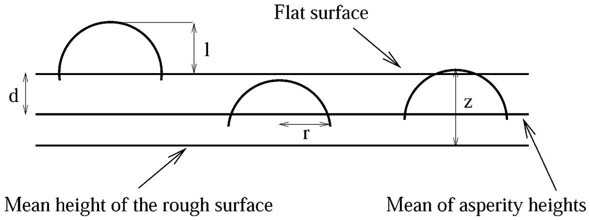

Figure 2.6: Greenwood and Williamson (GW) surface model [21]

This model predicts that the contact between two rough surfaces is equivalent to the contact between an infinitely hard surface, and a rough surface of Young's modulus E'. This model is shown in Figure 2.6. The distance l is the interference distance, or the distance the asperity has penetrated the flat surface. The roughness can be described by the standard deviation of the surface heights σ, the microasperity density η, and the asperity radius r.

Using this model to predict the contact area, an electrical analysis is performed for two cases: one where an insulating oxide layer exists, and one with metal-on-metal contact. A cracking model for the oxide layer is used to denote where each model is used.

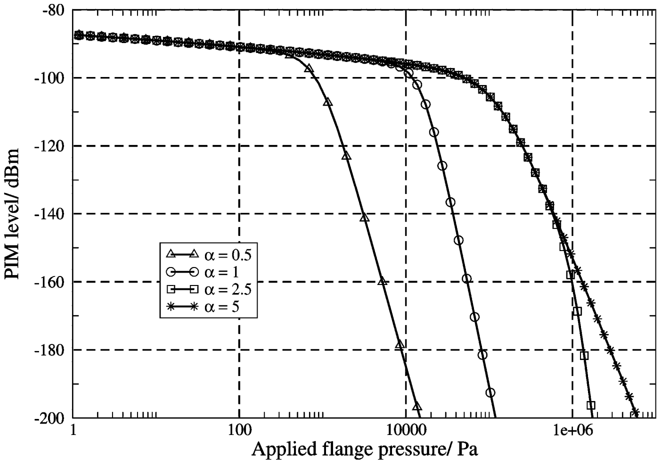

Figure 2.7: Third-order PIM level for three different surface topographies [21]

Figure 2.7 shows the third order PIM for three different surface topographies. The trend of these results match previous experimental measurements. This model has not however been fully validated experimentally.

2.3 Temperature Stable Resonator and Filter Design

Research on the topic of temperature compensation for microwave devices can be split into three broad categories:

- Limiting designs to using only materials with high thermal stability with respect to dimension and RF properties.
- Attempting to control a component's temperature, removing the root cause of temperature drift.
- Designing a device using materials with specific dimensional and/or property drift, in such a way that net temperature drift is low.

Each of these approaches has inherent advantages and disadvantages. Some important work in the field of thermally stable RF design using each approach is presented here.

2.3.1 Thermal Stability and Material Science

The simplest way to ensure low temperature drift in a microwave filter is to use materials with high thermal stability. Conductors must be dimensionally stable. Dielectrics must be both dimensionally stable, and have a stable dielectric constant.

Early designs requiring high thermal stability used Invar conductor [2]. Invar is an iron-nickel alloy that exhibits exceptionally high dimensional stability. The coefficient of thermal expansion (CTE) of Invar is approximately 1.6 ppm$/^{\circ}\mathrm{C}$ (depending on the alloy). For comparison, the CTE of aluminum is 23 ppm$/^{\circ}\mathrm{C}$. It will be shown in Chapter 3 that the absolute value of the frequency-drift coefficient is approximately equal to the CTE. An Invar resonator or filter will therefore exhibit a 93% reduction in temperature drift.

When compared to other conductors such as aluminum and copper, Invar has a number of drawbacks. A major drawback in many applications is its mass; the density of Invar is

$8050\ \mathrm{kg/m^3}$. By comparison, the density of aluminum is $2700\ \mathrm{kg/m^3}$, nearly $1/3$ the weight by volume. This is a major penalty in space applications where mass reduction is critical.

The poor machinability of Invar is another drawback. During machining, Invar can exhibit work hardening that can lead to warping. It also has a tendency to break up during machining. For these reasons, constructing components from Invar is difficult and expensive.

Another design concern when using Invar conductor is heat dissipation. Resistive heating is a major source of heat in the high power applications where waveguide filters are commonly used. Heat generated inside the cavity walls must be dissipated to the environment efficiently in order to minimize temperature drift.

Since the thermal conductivity of Invar is $10\ \mathrm{W/mK}$, it conducts heat less efficiently than other metals. The thermal conductivity of aluminum and copper are $200\ \mathrm{W/mK}$ and $400\ \mathrm{W/mK}$ respectively. Invar will act as an insulator when compared to these materials, trapping heat inside a waveguide [22, 23].

Invar filters deployed on the early Intelsat satellites were implemented using standard 0.064 inch thick walls and standard flanges [10]. The first step taken to address the mass problem was to reduce the wall thickness to less than 0.030 inches.

In the 1970s and 80s, composite materials began to replace Invar in some designs [14, 10, 20]. These composites consisted of a graphite structure, with a high conductivity layer of silver to serve as a conductor. These plastic fibre composites are lightweight, and exhibit dimensional stability that meets or exceeds that of Invar.

Although graphite waveguides are lightweight and have high thermal stability, manufacturing issues hinder their implementation. Graphite waveguides require elaborate quality control, and are more difficult to manufacture than modern Invar waveguides. For these reasons, graphite filters are rarely used today.

In the 1970s, dielectrics exhibiting high thermal stability, suitable for microwave frequencies were beginning to be developed [10]. Although it had been known for many years that dielectric resonators could be used to produce compact, low-loss filters, poor thermal properties had precluded their use.

Fiedziuszko proposed the first dielectric filter that demonstrated substantial improvement over existing technology in [14]. A dual-mode dielectric filter was proposed. This design was made possible by the development of thermally stable, low loss ceramic dielectrics.

The configuration proposed by Fiedziuszko is similar to metal-wall dual-mode cavity filters. It consists of a series of cylindrical cavities, each supporting two perpendicular modes. The resonant frequency of each mode is tuned by two screws at $90°$ to one another. Coupling between modes within each cavity is provided by a coupling screw between the perpendicular tuning screws at $45°$. Fiedziuszko's diagram of this filter is shown in Figure 2.8.

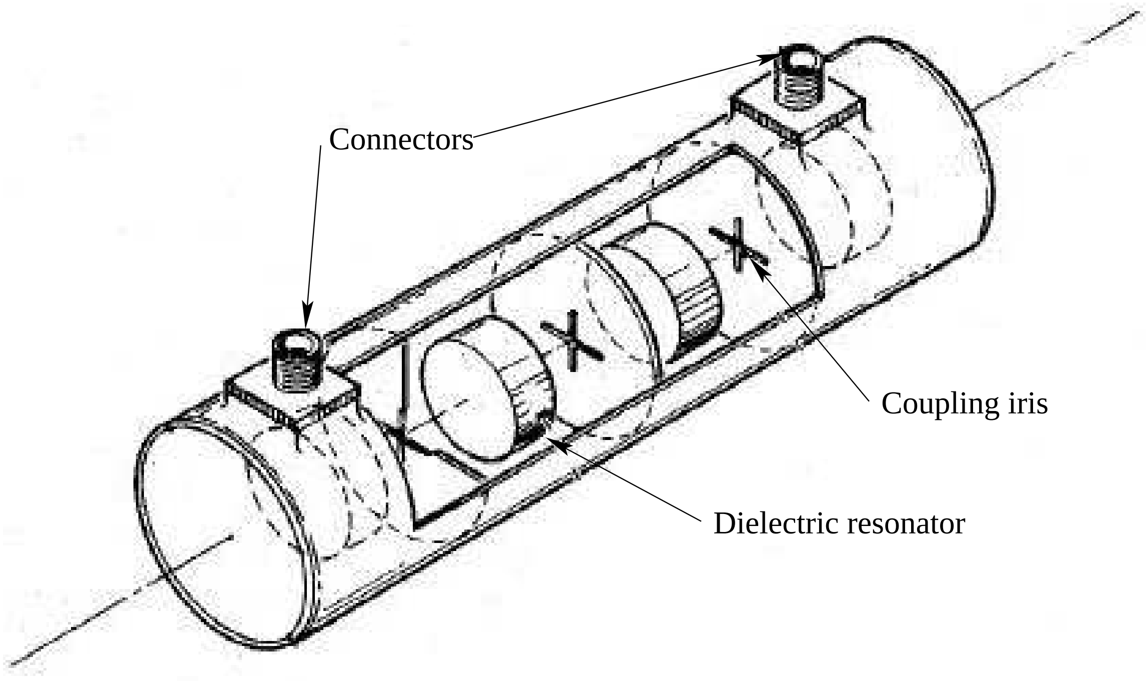

Figure 2.8: Diagram of a dual-mode dielectric filter [14]

In this design, dielectric cylinders are mounted coaxially in each cavity. The dielectric is mounted with a low-loss, stable material to ensure low temperature drift.

Since the fields are concentrated inside the dielectric, a substantial volume savings is achieved. An 8-pole filter described in [14] provides a 12 times reduction in volume when compared to an 8-pole dual-mode cavity filter.

Again, since the fields are concentrated inside the dielectric, the effect of the enclosure's thermal expansion is greatly reduced. The temperature drift of the dielectric is the dominant factor in thermal performance. By using a dielectric with a slightly negative temperature coefficient, near perfect temperature compensation is possible.

Since expansion of the cavity walls is no longer the dominant factor in thermal performance, thin-walled Invar or graphite technologies are not required. The filter presented in [14] represents approximately $30 - 40\%$ of the weight of a comparable graphite filter, and $18 - 25\%$ of a thin-walled Invar filter.

Dual-mode dielectric filters are widely implemented in industry, however they are not suitable for all applications. Resonant cavity filters are still often used for their power handling capability. Where dielectric filters are appropriate, this design is also limited to dielectrics with high thermal stability. Low-loss dielectrics such as sapphire cannot be used because of their poor thermal stability.

2.3.2 Temperature Control in RF Designs

Thermal drift in RF components can also be reduced by attempting to control temperature. Research that implements this approach using both active and passive cooling is presented here.

In [22], Atia proposed a dual-mode cavity filter that uses a heat exchanger to reject heat more efficiently. A dual-mode TE_{113} cavity filter is proposed. The cavity walls are constructed from Invar.

Due to the poor thermal conductivity of Invar, heat tends to get trapped inside the Invar cavity. In order to alleviate this problem, Atia proposes that thick copper irises attached to an external heat exchanger be used to conduct heat out of the cavity. The high thermal conductivity of copper, along with the large surface area of the heat exchanger allows heat to be dissipated more efficiently. A cross section of the proposed filter is shown in Figure 2.9.

The filter shown in Figure 2.9 exhibits a dramatic reduction in temperature rise at a given power level. At $400\ \mathrm{W}$, temperature increase is reduced by an order of magnitude when compared to an all-Invar filter. Adding a heat exchanger however results in an increase in mass and volume over a traditional filter. Also, this approach requires low ambient temperature to provide an effective heat sink.

In [24], Rosowsky and Wolk propose a satellite multiplexer that dissipates heat by means of heat pipes. This multiplexer uses Invar waveguide to construct the filter portion of the multiplexer. Heat pipes containing NH_3 are attached to the Invar cavities.

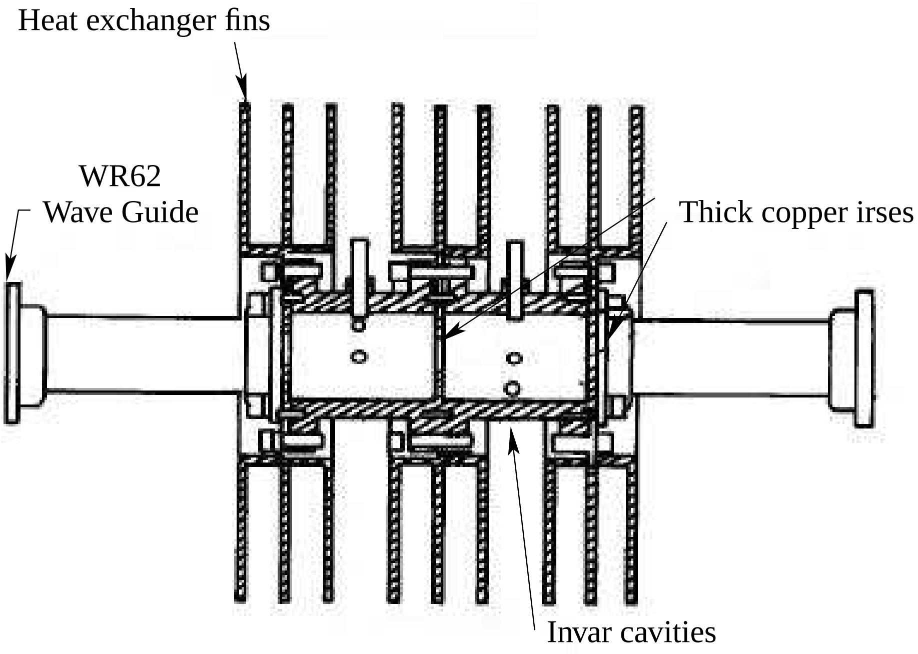

Figure 2.9: Bandpass filter with heat exchanger [22]

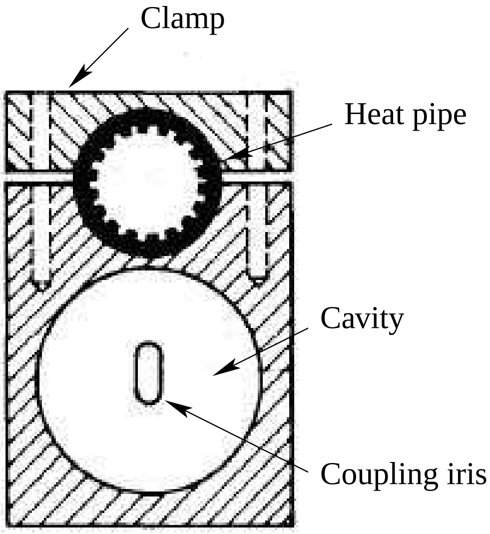

Figure 2.10: Cross-section of a heat-pipe cooled waveguide [24]

As the NH_3 is heated, it evaporates and travels to the evaporation zone, near the perimeter of the satellite. Heat is dissipated by radiation, the NH_3 condenses, and the cycle continues. Since the medium in the heat pipes is transported by capillary action, no moving parts are required. A cross section of the waveguide and heat pipe are shown in Figure 2.10.

A large contact area is needed between the cavity and heat pipe. TE_{113} dual-mode filter would provide the best electrical performance for this configuration. This filter however is too small to provide sufficient contact area between the filter and the cooling pipes. A TE_{112} single-mode cylindrical filter is used instead. This increased size adds mass to the filter.

In order to reduce the temperature of the irises, they are constructed from pure silver. This allows for more efficient heat conduction when compared to Invar. The cavities are constructed from Invar so that the drift in resonant frequency is reduced.

There has been substantial research on the subject of high-temperature superconductors (HTS) to realize microwave filters [25, 26]. These designs use cryogenic cooling to achieve miniaturization and performance gain. This approach can be used to realize a filter with near-infinite unloaded Q. Temperature must be controlled actively to 77K using a cryogenic cooler. Questions about the long-term reliability of cryogenic coolers have prevented wide-spread implementation of this approach.

2.3.3 Net Thermal Stability Approach

A third category of thermal compensation attempts to maximize the net thermal stability, while using materials with low thermal stability. This involves choosing appropriate materials for parts of a resonator geometry so that net temperature drift is reduced.

One such design is the hybrid mode dielectric resonator described in [27, 28]. The structure of this resonator, shown in Figure 2.11, was proposed by Karp [29] and later used by Fiedziuszko for oscillator applications [30]. It consists of two dielectric resonators, each connected to a threaded rod. The threaded rods are considered to be dielectrics with low loss, and a lower dielectric constant than the resonator. The threaded rods are mounted on a cylindrical conducting enclosure. A wide tuning range can be achieved by turning the threaded rods (tuning rods), which moves the dielectric resonators along the enclosure axis.

It is assumed that all components are allowed to expand freely. Consider a change in temperature ΔT from an ambient temperature T_o. The dimensions and dielectric constants will vary

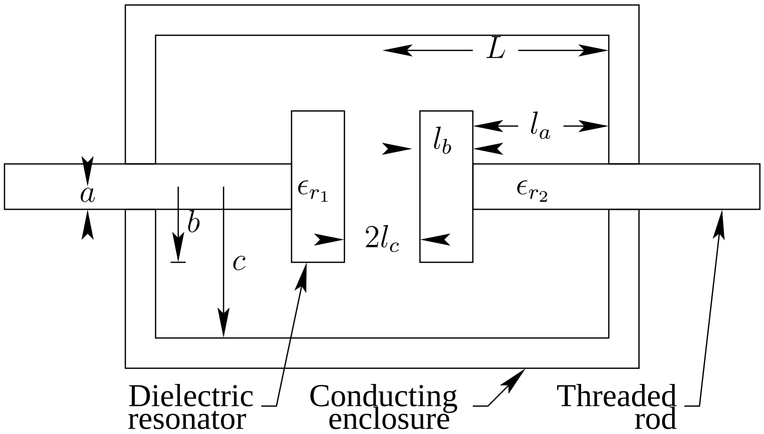

Figure 2.11: Tunable temperature-compensated hybrid dielectric-resonator

according to,

$$\begin{aligned}
l_a &= l_{ao}(1+\alpha_a \Delta T) & a &= a_o(1+\alpha_a \Delta T) \\
l_b &= l_{bo}(1+\alpha_b \Delta T) & b &= b_o(1+\alpha_b \Delta T) \\
L &= L_o(1+\alpha_c \Delta T) & c &= c_o(1+\alpha_c \Delta T) \\
\epsilon_{r_1} &= \epsilon_{r_{1o}}(1+\tau_b \Delta T) & \epsilon_{r_2} &= \epsilon_{r_{2o}}(1+\tau_a \Delta T)
\end{aligned}$$

$$l_c = (L_o - l_{bo} - l_{ao}) + \Delta T(\alpha_c L_o - \alpha_b l_{ob} - \alpha_a l_{ao}) \tag{2.8}$$

where α_a, α_b, and α_c are the linear CTEs of the tuning rod, the dielectric resonator, and the enclosure respectively. The dielectric temperature coefficients of the tuning rod and dielectric resonator are τ_a, and τ_b respectively. The terms l_{ao}, a_o, l_{bo}, b_o, L_o, and c_o are the nominal dimensions at ambient temperature. The nominal permittivity of the dielectric resonator is $\epsilon_{r_{1o}}$, and the nominal permittivity of the tuning rod is $\epsilon_{r_{2o}}$. This analysis assumes linear expansion, and linear temperature dependence of the dielectric constants.

The temperature drift of the entire structure's resonant-frequency is dominated by two factors: the overall temperature coefficient of the dielectric (which is a function of the dielectric temperature coefficient τ_b, and the CTE of the dielectric resonator α_b); and the variation of the gaps between the dielectric resonators l_c. The gap variation is largely determined by the CTE of the enclosure α_c, the CTE of the tuning rod α_a, and the tuning distance l_{ao}.

By choosing appropriate materials, temperature drift caused by variation in l_c can be reduced or eliminated. This is accomplished by choosing the enclosure material, the tuning rod material, and dimensions such that the second term of Equation 2.8 is cancelled. This will minimize temperature drift for a given dielectric resonator.

Combline resonators and filters have been widely used in communication systems since Matthaie presented the theoretical basis for their design in [31, 32]. Combline filters are well suited to moderate- and narrow-band applications. Figure 2.12 shows a typical combline resonator.

In [33, 20], it was proposed that combline resonators can be designed for temperature stability. It can be shown that the cavity resonance is heavily dependant on the capacitance between the tuning screw and the partial resonator rod, and that a negative temperature characteristic for this capacitance will result in a thermally stable resonance [33]. By using materials for the housing and tuning screw whose CTEs are significantly different, the temperature coefficient of the capacitance can be substantially negative.

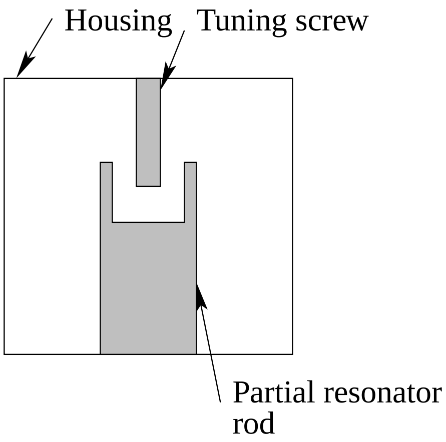

Figure 2.12: Cross-section of a temperature-compensated combline resonator

Realizing a temperature compensated resonator using this approach required time-consuming empirical work. Zaki later proposed a mode matching approach incorporating perturbation techniques that allowed for temperature stabilization in simulation [4]. Tuning the resonant frequency of a compensated cavity however degrades the compensation, which complicates implementation of these resonators in filters. This approach works well for applications suitable to combline resonators.

Another common approach to reducing temperature drift is to constrain cavity expansion. The work described in [34, 35] proposes two related designs that use this approach. The first design, shown in Figures 2.13 and 2.14 uses a control-arm constructed from a low CTE material such as Invar to constrain the expansion of one or more of the cavity surfaces. The deflection of the cavity walls will reduce the electric length of the cavity which reduces its resonant frequency.

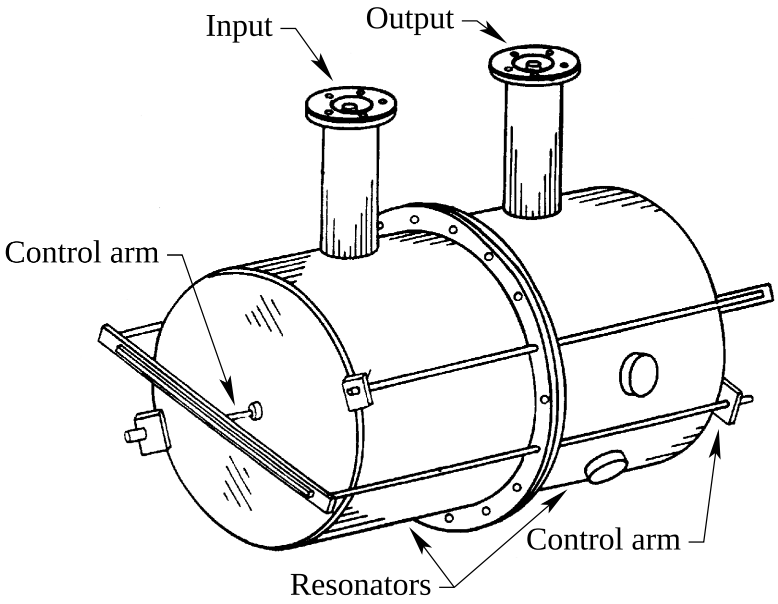

Figure 2.13: Sketch of a constrained-expansion temperature-compensated cavity filter [34]

The amount of temperature compensation depends on several factors: the size and shape of the cavity; the pre-tensioning of the control-arm; the CTE of the cavities and control-arm; the placement of the control-arm; and the thickness of the deformed walls. The single parameter that can be easily modified for tuning is the tension in the control-arm. This design is sensitive to the thickness of the deflected walls. The appropriate thickness of the wall must be determined in the design phase.

Finding an appropriate material for the control-arm is also an issue with this design. Invar can be used because of its extremely low CTE. However Invar is expensive and very difficult to machine.

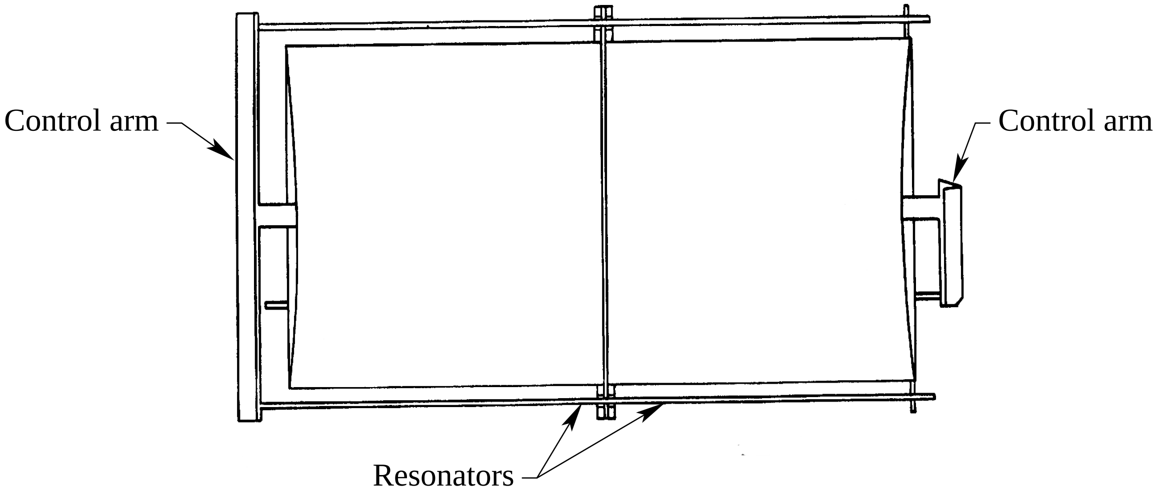

Figure 2.14: Sketch of a constrained-expansion temperature-compensated cavity filter, 2D view [34]

Another design described in [35, 34] proposes a cavity resonator with one domed wall constructed from a material with a relatively low CTE such as copper, as shown in Figure 2.15. The cavity will expand at a faster rate than the domed end cap. Since the edge of the dome is fixed to the cavity by the retaining ring, this expansion will cause the dome to deflect inward. This inward deflection compensates for the expansion of the cavity.

The temperature drift of the cavity shown in Figure 2.15 will depend on the CTE of the cavity, the CTE of the dome, and the thickness and shape of the dome. The dome will need to be much thinner than the other cavity walls. The only way to tune the compensation of such a resonator is to change the thickness and shape of the dome by machining it.

A 1999 patent filed by Lundquist [36] proposes another temperature compensated filter based on differential expansion. This design, shown in Figure 2.16 uses a high-expansion iris that protrudes into the cavity. By constructing the protruding iris from a material with a substantially higher coefficient of thermal expansion when compared to the cavity walls, the increasing protrusion of the iris into the cavity shortens its electric length, thus compensating for the expansion of the cavity walls.

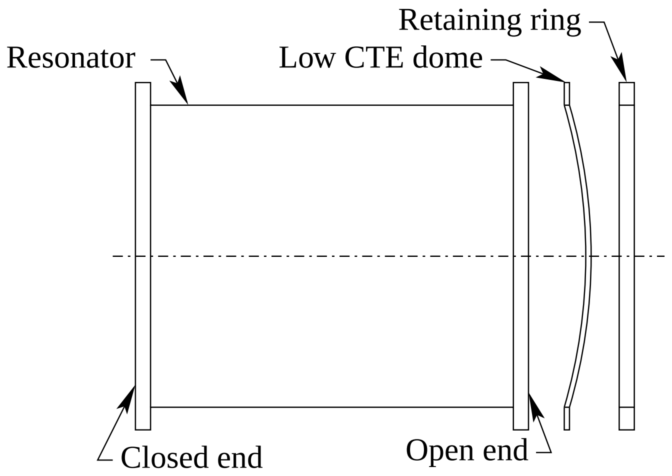

Figure 2.15: Domed-wall temperature-compensated resonator

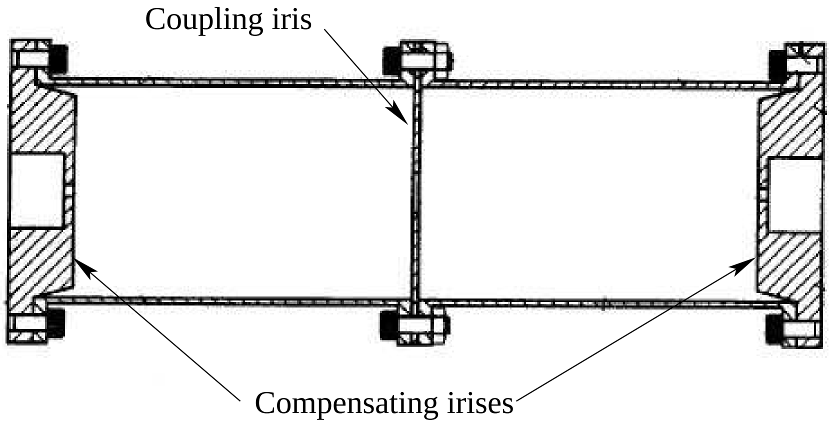

Figure 2.16: Temperature-compensated filter with a high-expansion iris [36]

Compensation in this design is driven by the differential coefficients of thermal expansion of the compensating iris and the walls. It is therefore necessary to find a material with an extremely high coefficient of thermal expansion. Furthermore, these compensating irises can only be used on the filter ends since it would have a reciprocal effect on resonance on the other side of the iris, thus increasing temperature drift.

Fitzpatrick proposed a constrained expansion design in [37]. This filter, shown in Figure 2.17, uses an external compensator to deflect the end-wall of a dual-mode cavity. By constructing the compensator from a low CTE material, the end wall will deflect inward reducing the electric length of the cavity, counteracting the effect of cavity expansion.

The amount of compensation will depend on the end-wall thickness, as well as the differential CTE of the control arm and cavity. By adjusting the tension in the control arm, compensation can be adjusted. Tuning range of the compensation however is limited, and care must be taken to avoid plastic deformation of the end wall which can lead to hysteresis.

Shape-memory alloys (SMA) are an interesting class of materials that can revert to a memorized shape when heated. This property can be used to provide useful work when a bias force is applied. This configuration is usually used in conjunction with resistive heating to construct an actuator [38, 39]. If an SMA actuator is driven by ambient temperature change however, this configuration can be used to produce a thermally-driven actuator.

Such a thermally-driven SMA actuator can be used to produce a temperature compensated resonator or filter. In [40, 41, 42], an SMA temperature compensator is proposed. The compensator, shown in Figure 2.18, consists of tuning rod enclosed by a housing which is screwed into the cavity wall. The motion of the tuning rod in and out of the cavity is facilitated by two linear bearings mounted in the housing. As temperature increases, a shape-memory alloy spring expands to its memorized shape, compressing the bias spring. This decreases the penetration of the tuning rod into the cavity, compensating for the effect of overall cavity expansion.

This design however, introduces a potential source of passive intermodulation at the weak contact between the tuning rod and the lower bearing. Furthermore, the actuation of shape-memory alloys is hysteretic with respect to temperature. There is an inherent drift associated with this hysteresis, even if the forward and reverse temperature paths are perfectly compensated. For the level of hysteresis exhibited by currently available materials, this means that a resonator compensated in this fashion cannot achieve drift at or below that of an Invar cavity.

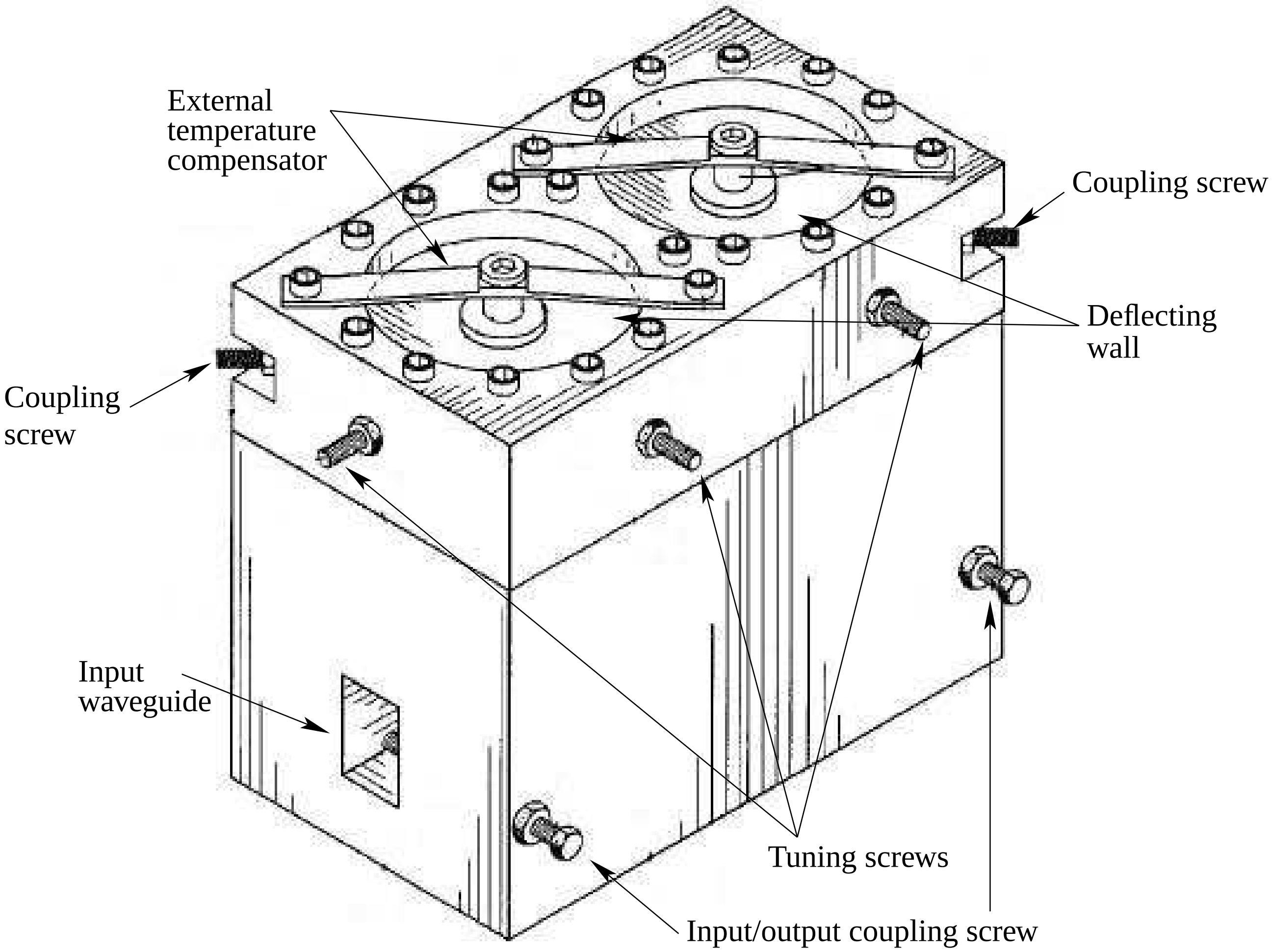

Figure 2.17: Temperature-compensated filter with external compensator [37]

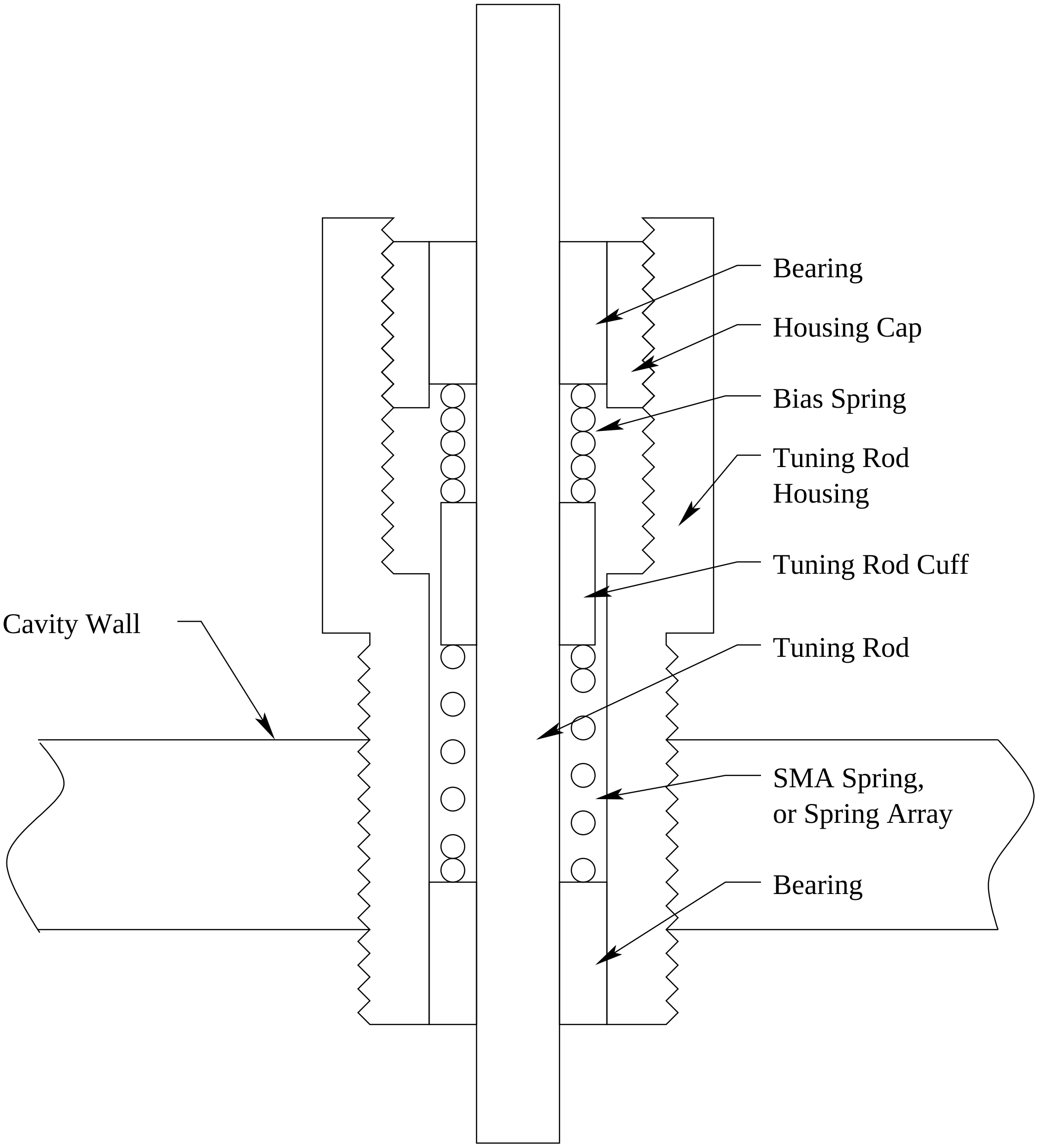

Figure 2.18: Diagram of a shape-memory alloy compensator

A bimetal is a planar component with two or more layers with substantially different coefficients of thermal expansion (CTE). The differential expansion in the planar direction causes a substantial out-of-plane deflection. There have been a number of temperature compensation schemes based on bimetallic actuators.

An early proposal for bimetal temperature compensation was presented by Basil in 1977 [43]. The proposed resonator, shown in Figure 2.19, has bimetallic walls consisting of an interior silver layer, and an external Invar layer. Since the entire cavity wall is a bimetal element well constrained at the edges, the amount of deflection is limited. Furthermore, since the cavity is principally constructed from Invar there is little mass savings. Also the temperature drift of a comparable all-Invar cavity is already quite low.

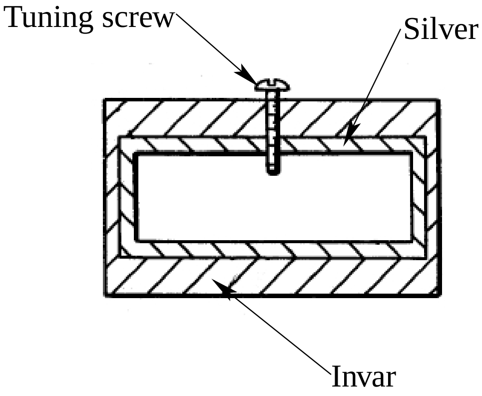

Figure 2.19: Compensated cavity with bimetallic walls [43]

In 1983 Jachowski proposed a bimetal compensator mounted on the cavity wall [44]. The wall-mounted compensator, shown in Figure 2.20 is designed to provide decreasing cavity perturbation as temperature increases, thereby counteracting the effect of cavity expansion.

The level of perturbation provided by a bimetal for a given temperature change is a function of the bimetal length. The amount of compensation is very sensitive to manufacturing tolerances with respect to the length of the bimetal. It is therefore required that bimetal compensation be adjustable.

Compensation adjustment is provided by the adjustment screw shown in Figure 2.20. This approach to tuning however is problematic in many applications. The weak contact between the

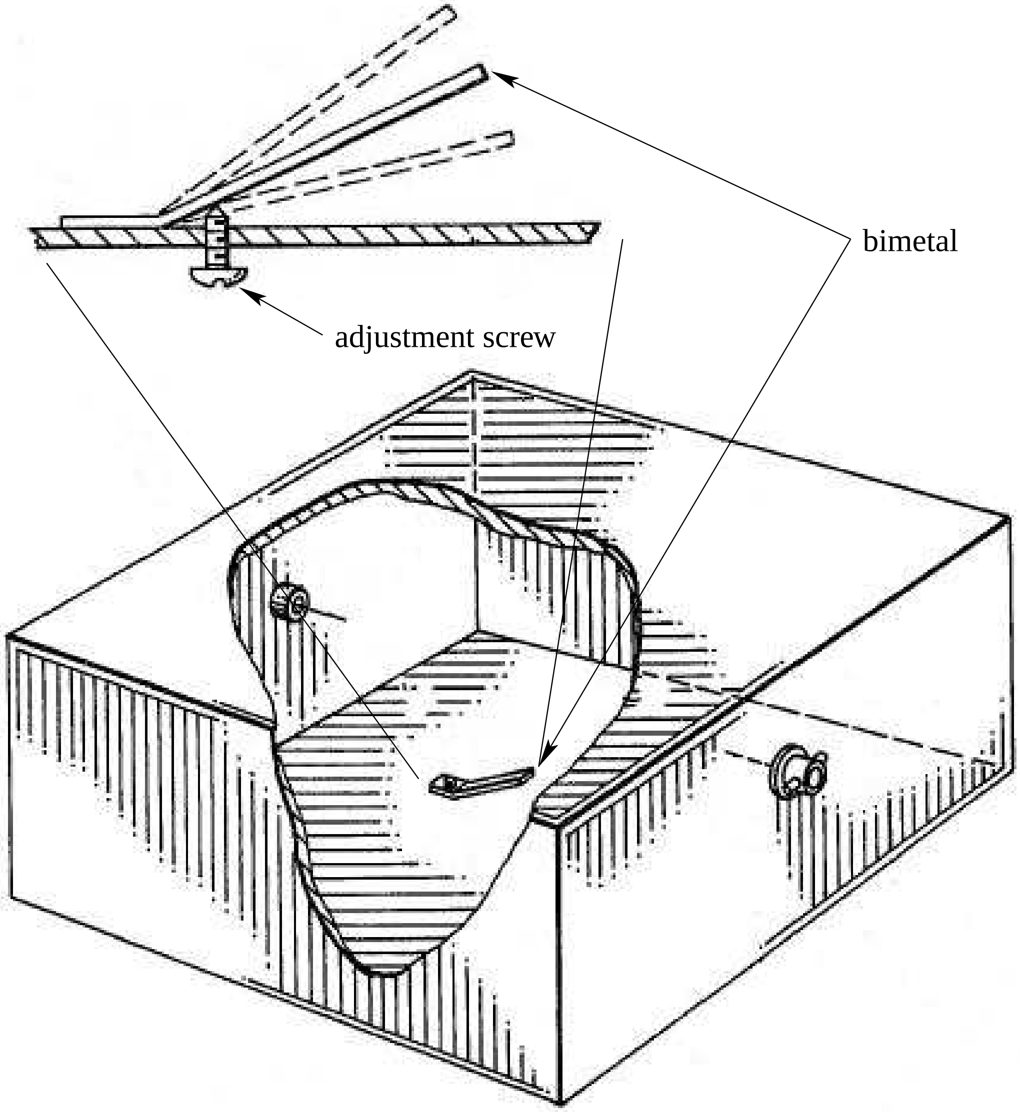

Figure 2.20: Wall mounted bimetal compensator [44]

adjustment screw and the bimetal is a potential source of passive intermodulation (PIM) which is a major issue in many applications.

In [45], a bimetal-compensated coupling iris is proposed by Kich. One embodiment of this iris is shown in Figure 2.21. In this embodiment, the electric length of the cavity is modified by the bimetal actuator, rather than perturbing the side wall. The opposite actuation is therefore required to compensate for cavity expansion; the bimetal must actuate into cavity with increasing temperature. The embodiment described in Figure 2.21 shows a weak intermetallic contact between the bimetal and iris wall, which can produce passive intermodulation.

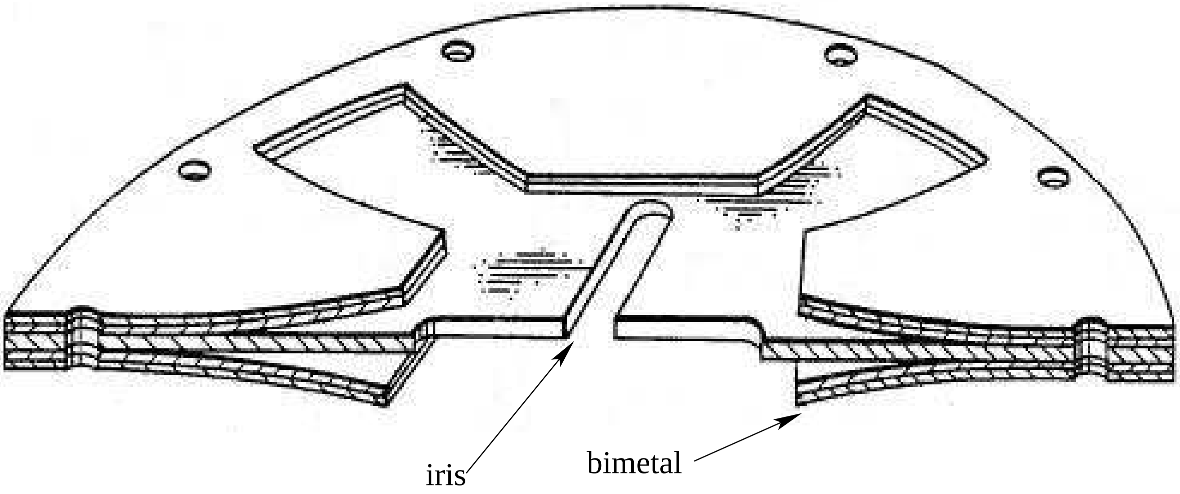

Figure 2.21: Cross-section of a bimetal compensated iris [45]

Kich also proposes a variable diameter tuning screw using bimetal elements, shown in Figure 2.22. The level of perturbation available for the given embodiment will be very limited, since the curved cross-section of the bimetal element will result in increased stiffness (and therefore reduced deflection).

Another proposed bimetal compensator is shown in Figure 2.23. This bimetal compensator proposed by Schmid in [46] uses an annular bimetal stack to provide actuation. The bimetal stack actuates against a fixed housing that is screwed into the cavity end plate.

The bias screw shown in Figure 2.23 maintains tension on the tuning screw to keep it mated to the bimetal stack. As temperature increases, the bimetal stack expands compressing the bias

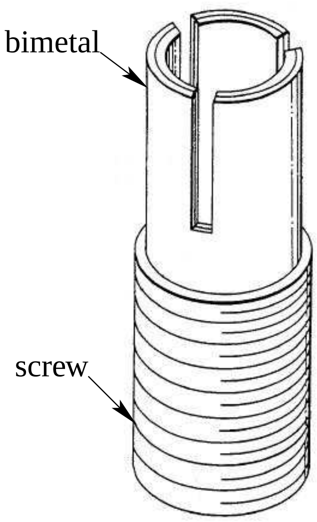

Figure 2.22: Variable diameter bimetal tuning element [45]

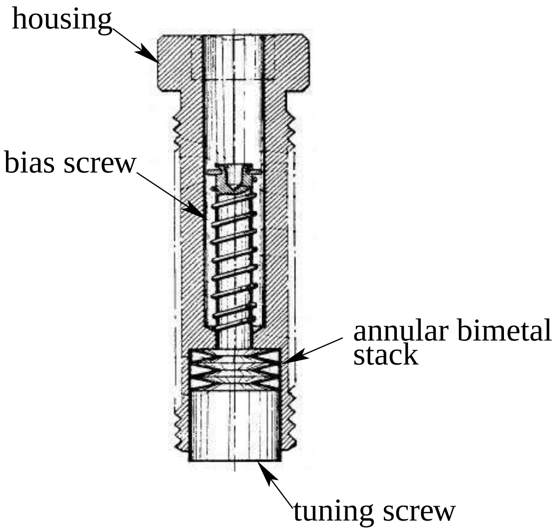

Figure 2.23: Annular bimetal tuning screw [46]

spring, and pushing the tuning screw further into the cavity. Since the tuning screw is mounted in the end wall, the actuation reduces the electric length as temperature increases, compensating for the expansion of the cavity.

By using a housing and tuning screw to mount the bimetal portion of the actuator outside the resonator, a small gap is crated between the tuning screw and housing. Such gaps can cause passive intermodulation in high-power applications, resulting in non-linear filter behaviour.

A compensator with the means of actuation positioned outside of cavity will pose a potential PIM problem at the point of insertion (c.f. Figures 2.18 and 2.23). Thomson proposed a bimetallic compensator in [47] that uses a bellows to eliminate this interface.

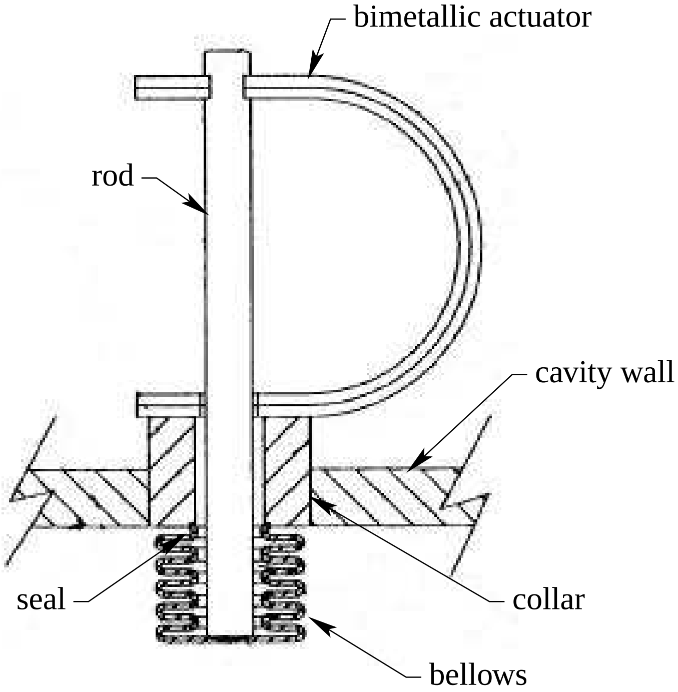

Figure 2.24: Bimetal-actuated compensator with bellows [47]

The bellows, shown in Figure 2.24, is attached to a collar with a seal (generally a weld or solder). The collar is mounted in the side-wall of the cavity or filter. A bimetallic actuator is anchored to the collar outside the cavity, and actuates a rod enclosed by the collar. As temperature decreases, the bellows is pushed further into the cavity, compensating for the overall expansion of the cavity or filter.

Although this design eliminates the PIM problem, it raises other design issues. The bellows and seal must be conductors. It is difficult to construct the bellows from a conductor material and achieve sufficient deflection without inducing plastic deformation, which results in hysteresis with respect to temperature. Also, there must be sufficient thermal coupling between the bimetal and the cavity to ensure that the compensation does not lag the filter drift.

2.4 Bimetal Theory

A bimetal is a two-layer material, each layer having a different coefficient of thermal expansion (CTE). When heated, the differential expansion in the layers of the bimetal result in a large out-of-plane deflection [48]. Bimetals are most commonly used commercially in thermostats or temperature sensors, and are often referred to as thermostatic bimetals.

Timoshenko provided the first detailed investigation of bimetal behaviour in [49]. This analysis provides a means to describe the complete bimetal travel over a given operating-temperature range. This analysis assumes that the difference between the CTEs of each material remains constant over the operating-temperature range. It is further assumed that the width of the bimetal strip is small, and that friction forces at the bimetal supports are negligible. This work is used as the basis for specifying actuation in commercial bimetals.

Timoshenko's analysis from [49] is as follows. Consider the bimetal strip shown in Figure 2.25 under uniform heating from T_o to T. The CTEs of layers I and II are α_1 and α_2 respectively, and $\alpha_2 > \alpha_1$. The width of the strip is unity.

Consider the elemental section op shown in Figure 2.25. Since section op is at equilibrium, the following is true for the tensile forces P_i and bending moments M_i in each layer:

$$P_1 = P_2 = P \tag{2.9}$$

$$M_1 = P_1 \tfrac{t_1}{2}, \; M_2 = P_2 \tfrac{t_2}{2}. \tag{2.10}$$

Rearranging (2.10) to find t_1 and t_2, and given that $t_1 + t_2 = t$, then,

$$\frac{2M_1}{P_1} + \frac{2M_2}{P_2} = t. \tag{2.11}$$

Substituting (2.9) into (2.11),

$$M_1 + M_2 = P\frac{t}{2}. \tag{2.12}$$

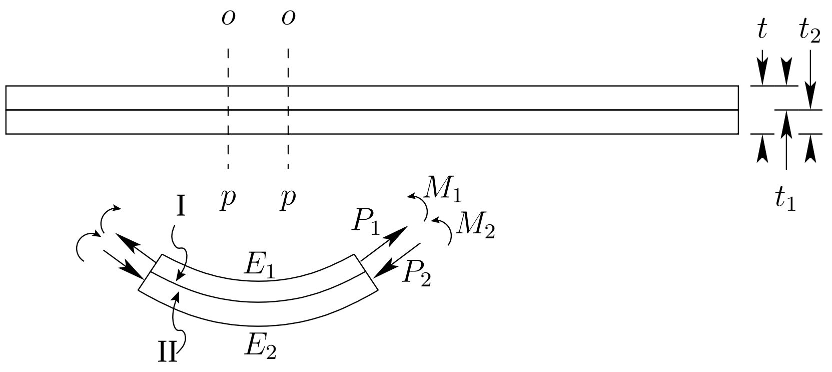

Figure 2.25: Bimetal under uniform heating [49]

If the radius of the curved strip is R, then the bending moments can be expressed in terms of the moduli E and second moments of inertia I as follows:

$$M_1 = \frac{E_1 I_1}{R}, \; M_2 = \frac{E_2 I_2}{R}$$

which substituted into (2.12) produces,

$$\begin{aligned} \frac{Pt}{2} &= \frac{E_1 I_1 + E_2 I_2}{R} \\ P &= \frac{2(E_1 I_1 + E_2 I_2)}{tR}. \end{aligned} \tag{2.13}$$

In order to solve for the radius of curvature, another equation for R and P is required. Consider the interface between the two metals. The elongation of the surface at the interface must be equal on each side. For a temperature difference $\Delta T = T = T_o$ therefore,

$$\alpha_1 \Delta T + \frac{P_1}{E_1 t_1} + \frac{t_1}{2R} = \alpha_2 \Delta T - \frac{P_2}{E_2 t_2} - \frac{t_2}{2R}. \tag{2.14}$$

The first term on each side of (2.14) accounts for the unit elongation due to thermal expansion, the second term is from elongation from the axial forces P_1 and P_2, and the third term accounts for the difference in elongation from the neutral axis of each side to the interface due to bending.

Substituting (2.13) into (2.14), and given (2.9),

$$\frac{t}{2R} + \frac{2(E_1 I_1 + E_2 I_2)}{tR} \left(\frac{1}{E_1 t_1} + \frac{1}{E_2 t_2} \right) = (\alpha_2 - \alpha_1)\, \Delta T,$$

and solving for the curvature,

$$\frac{1}{R} = \frac{(\alpha_2 - \alpha_1)\Delta T}{\frac{t}{2} + \frac{2(E_1 I_1 + E_2 I_2)}{t}\left(\frac{1}{E_1 t_1} + \frac{1}{E_2 t_2}\right)}. \tag{2.15}$$

Let,

$$\frac{t_1}{t_2} = m\ ,\ \frac{E_1}{E_2} = n,$$

and given that the second moment of inertia for each rectangular beam is,

$$I_1 = \frac{{t_1}^3}{12}\ ,\ I_2 = \frac{{t_2}^3}{12}.$$

Equation 2.15 can be simplified as follows.

$$\begin{aligned}
\frac{1}{R} &= \frac{(\alpha_2 - \alpha_1)\Delta T}{\frac{t}{2} + \frac{({t_1}^3 E_1 + {t_2}^3 E_2)}{6t}\left(\frac{1}{E_1 t_1} + \frac{1}{E_2 t_2}\right)} \\
&= \frac{6(\alpha_2 - \alpha_1)\Delta T}{t\left(3 + \frac{({t_1}^3 E_1 + {t_2}^3 E_2)}{(t_1 + t_2)^2}\left(\frac{1}{E_1 t_1} + \frac{1}{E_2 t_2}\right)\right)} \\
&= \frac{6(\alpha_2 - \alpha_1)\Delta T}{t\left(3 + \frac{\left(\frac{1}{E_2 {t_2}^3}\right)({t_1}^3 E_1 + {t_2}^3 E_2)}{\left(\frac{1}{{t_2}^2}\right)(t_1 + t_2)^2}(E_2 t_2)\left(\frac{1}{E_1 t_1} + \frac{1}{E_2 t_2}\right)\right)} \\
&= \frac{6\left(\alpha_2 - \alpha_1\right)\Delta T}{t\left(3 + \frac{m^3 n + 1}{(1+m)^2}\left(\frac{1}{mn} + 1\right)\right)} \\
&= \frac{6\left(\alpha_2 - \alpha_1\right)\Delta T\left(1 + m\right)^2}{t\left(3\left(1 + m\right)^2 + (mn)\left(\frac{1}{mn} + 1\right)\left(\frac{1}{mn}\right)\left(m^3 n + 1\right)\right)} \\
&= \frac{6\left(\alpha_2 - \alpha_1\right)\Delta T\left(1 + m\right)^2}{t\left(3\left(1 + m\right)^2 + \left(1 + mn\right)\left(m^2 + \frac{1}{mn}\right)\right)} \qquad (2.16)
\end{aligned}$$

It is often the case in industrial applications that the layer thicknesses are equal or nearly equal. So assuming $m = 1$, (2.16) simplifies to,

$$\begin{aligned}
\frac{1}{R} &= \frac{24\left(\alpha_2 - \alpha_1\right)\Delta T}{h\left(12 + \left(1 + n\right)\left(1 + \frac{1}{n}\right)\right)} \\
&= \frac{24\left(\alpha_2 - \alpha_1\right)\Delta T}{h\left(14 + n + \frac{1}{n}\right)}.
\end{aligned}$$

Consider the effect of the moduli on actuation. If the layer moduli are equal, the curvature is,

$$\frac{1}{R} = \frac{3\left(\alpha_2 - \alpha_1\right)\Delta T}{2t}. \tag{2.17}$$

Alternatively, if one material modulus is twice the other, $n = 2$ or $n = 1/2$. In both cases,

$$\frac{1}{R} = \frac{48\left(\alpha_2 - \alpha_1\right)\Delta T}{33t}. \tag{2.18}$$

So for a 100% change in the modulus fraction, the difference in the bimetal curvature is about 3%. Actuation is therefore principally dependent on differential expansion, and relatively independent of material modulus.

The bimetal curvature indexed to temperature change is defined as the specific deflection, or flexivity k. Flexivity is given by,

$$k = \frac{t}{\Delta T R} = \frac{6\left(\alpha_2 - \alpha_1\right)\left(1+m\right)^2}{\left(3\left(1+m\right)^2 + \left(1+mn\right)\left(m^2 + \frac{1}{mn}\right)\right)}.$$

More commonly, it is assumed that $m = n = 1$, and flexivity is,

$$k = \frac{t}{\Delta T R} = \frac{3}{2}\left(\alpha_2 - \alpha_1\right). \tag{2.19}$$

For commercially produced bimetals, flexivity is generally specified directly by the manufacturer rather than calculated. The flexivity is very useful in determining actuation for any number of bimetal configurations. Consider for example a simply supported bimetal shown in Figure 2.26.

The deflection d of a simply supported beam can be found in terms of the flexivity k, the temperature change ΔT, the bimetal length L, and the thickness of the low CTE side t_1. Consider the right-angle triangle from Figure 2.26 [48].

$$\begin{aligned} \left(R - t_1 - d\right)^2 + \left(\frac{L}{2}\right)^2 &= \left(R - t_1\right)^2 \\ 2dt_1 + d^2 + \frac{L^2}{4} &= 2Rd \\ \frac{1}{R} &= \frac{8d}{L^2 + 4d^2 + 8dt_1} \end{aligned}$$

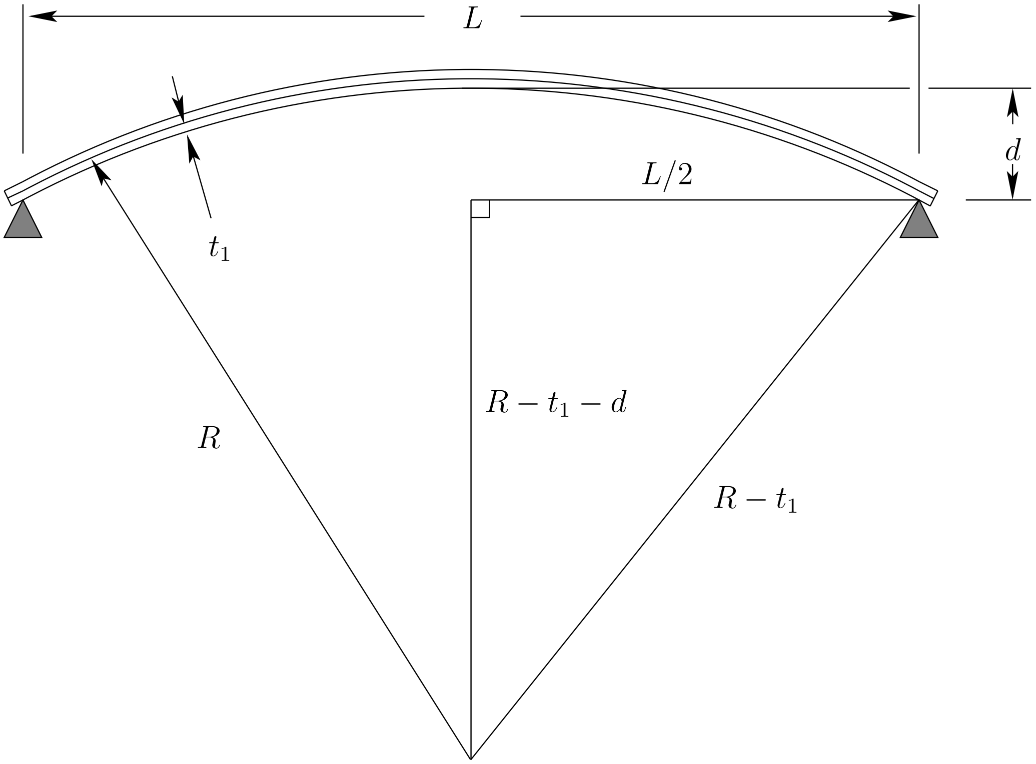

Figure 2.26: Simply supported bimetal strip

Assuming that the deflection d and thickness t are less than 10% of the length of the strip, then the terms $8dt_1$ and $4d^2$ are negligible so,

$$d = \frac{L^2}{8R}. \tag{2.20}$$

Substituting (2.19) into (2.20) the deflection can be written in terms of flexivity,

$$d = \frac{kL^2 \Delta T}{8t}. \tag{2.21}$$

A cantilevered configuration as illustrated in Figure 2.27 is also common in bimetal applications. It is generally assumed that the radius of curvature is constant. This assumption is not strictly true due to the effect of the end constraint.

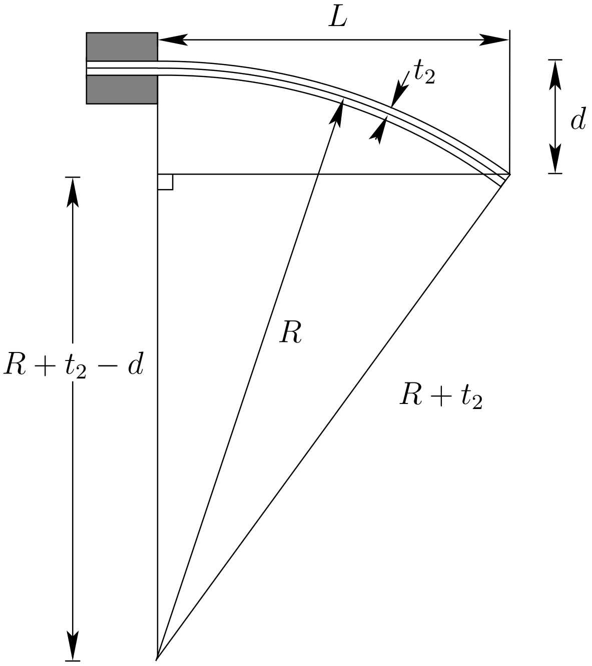

Figure 2.27: Cantilevered bimetal strip

Solving for the curvature using the right angle triangle from Figure 2.27,

$$\begin{aligned} (R + t_2 - d)^2 + L^2 &= (R + t_2)^2 \\ L^2 + d^2 - 2t_2 d &= 2Rd \\ \frac{1}{R} &= \frac{2d}{L^2 + d^2 + 2dt_2}. \end{aligned}$$

Again, assuming that the deflection d and thickness t are less than 10% of the length of the strip, then the terms $2dt_1$ and d^2 are negligible then,

$$d = \frac{L^2}{2R}. \tag{2.22}$$

Substituting (2.19) into (2.22) the deflection can be written in terms of flexivity,

$$d = \frac{kL^2\Delta T}{2t}. \tag{2.23}$$

Specific deflection is often used as an alternative to flexivity for specifying the actuation of a bimetal. The specific deflection a is defined for a cantilevered bimetal as,

$$a = \frac{dt}{L^2\Delta T}. \tag{2.24}$$

The tip deflection written in terms of the specific deflection is,

$$d = \frac{aL^2\Delta T}{t}. \tag{2.25}$$

The actuation of a bimetal can be specified in terms of either flexivity k, or specific deflection a. The derivation of the flexivity (2.19) contains a number of assumptions. In practice, flexivity and specific deflection are derived experimentally. Standard experimental determination of flexivity is provided in ASTM B388 [50] and DIN 1715 [51].

Flexivity is determined by measuring deflection for a simply supported bimetal. The design formula from ASTM B288 differs from (2.21) to account for some of the assumptions used in its derivation. The design formula is as follows.

$$d = \frac{0.1325kL^2\Delta T}{t}$$

Specific deflection is determined by measuring tip deflection for a cantilevered bimetal. From (2.23) and (2.25), the specific deflection is theoretically half the flexivity. The specific deflection measurement will account for the effect of end constraints, unlike the derivation above. To account for end effects, the relationship between flexivity and specific deflection is commonly defined as [52, 53],

$$a = 0.53k. \tag{2.26}$$

Using the modified relationship between flexivity and specific deflection, the equation for the tip deflection of a cantilevered beam (2.23) becomes

$$d = \frac{0.53kL^2\Delta T}{t}, \tag{2.27}$$

while (2.25) is unchanged.

In practice the specific deflection can be temperature dependent. A specified flexivity of specific deflection should also include a temperature range over which it is valid.

Note that the behaviour of various other bimetal components are specified in terms of specific deflection or flexivity; some examples include coils or u-shaped elements [52, 54].

Chapter 3

Quantifying Temperature Drift

In this chapter, an equation describing temperature drift in a lossless source-free region is derived from Maxwell's equations. This equation is valid for any passive component with a uniform coefficient of thermal expansion; for example resonators, filters, and multiplexers constructed from a single material. Using Maxwell's equations it is demonstrated that the same equation closely approximates temperature drift for a lossy source-free region for practical expansion coefficients. An approximate model for the contribution of iris expansion to temperature drift is described. HFSS simulations are presented to validate this approximation. The metrics used in this work to quantify temperature drift are described.

3.1 Generalized Temperature Drift in a Lossless Source-Free Medium

It is important to understand and quantify the temperature drift problem before attempting to address it. A thorough understanding of temperature drift is important when designing methods to counteract it.

Consider a passive RF device where the field boundaries are provided by a structure with a single linear coefficient of thermal expansion (CTE). This category includes almost any passive RF device including waveguides, filters, and multiplexers provided they are constructed from materials with a single linear CTE.

Assuming the device is allowed to expand freely, the normal strain ε and shear strain τ for linear expansion are given by [55]

$$\varepsilon_x = \varepsilon_y = \varepsilon_z = \alpha \Delta T$$
$$\tau_x = \tau_y = \tau_z = 0$$

for a CTE α and a temperature change ΔT.

Assuming the device is lossless, Maxwell's wave equations must be satisfied [56].

$$\begin{aligned} \nabla^2 \mathbf{E} &= -k^2 \mathbf{E} \\ \nabla^2 \mathbf{H} &= -k^2 \mathbf{H} \end{aligned} \tag{3.1}$$

where the phase constant k is given by

$$k = 2\pi f \sqrt{\mu \varepsilon}. \tag{3.2}$$

In rectangular coordinates, the electric field can be separated into component vector fields as follows,

$$\mathbf{E}(x, y, z) = \hat{a}_x E_x(x, y, z) + \hat{a}_y E_y(x, y, z) + \hat{a}_z E_z(x, y, z) \tag{3.3}$$

where $(\hat{a}_x, \hat{a}_y, \hat{a}_z)$ are unit direction vectors.

Substituting (3.3) into (3.1),

$$\nabla^2 \mathbf{E} + k^2 \mathbf{E} = \nabla^2 (\hat{a}_x E_x + \hat{a}_y E_y + \hat{a}_z E_z) + k^2 (\hat{a}_x E_x + \hat{a}_y E_y + \hat{a}_z E_z) = 0$$

reducing the vector wave equation to three scalar wave equations.

$$\nabla^2 E_x(x, y, z) + k^2 E_x(x, y, z) = 0 \tag{3.4}$$
$$\nabla^2 E_y(x, y, z) + k^2 E_y(x, y, z) = 0 \tag{3.5}$$
$$\nabla^2 E_z(x, y, z) + k^2 E_z(x, y, z) = 0 \tag{3.6}$$

Since the scalar wave equations above are of the same form, the solution forms will be similar. Expanding (3.4),

$$\nabla^2 E_x(x, y, z) + k^2 E_x(x, y, z) = \frac{\partial^2 E_x}{\partial x^2} + \frac{\partial^2 E_x}{\partial y^2} + \frac{\partial^2 E_x}{\partial z^2} + k^2 E_x = 0. \tag{3.7}$$

Using separation of variables, assume that any solution to $E_x(x, y, z)$ can be written as,

$$E_x(x, y, z) = f(x)g(y)h(z). \tag{3.8}$$

This assumes that the x, y, z variations of E_x are separable.

Substituting (3.8) into (3.7),

$$\begin{aligned} gh\frac{d^2f}{dx^2} + fh\frac{d^2g}{dy^2} + fg\frac{d^2h}{dz^2} &= -fghk^2 \\ \frac{1}{f}\frac{d^2f}{dx^2} + \frac{1}{g}\frac{d^2g}{dy^2} + \frac{1}{h}\frac{d^2h}{dz^2} &= -k^2. \end{aligned} \tag{3.9}$$

Each term on the left hand side of (3.9) is a function of an independent variable. For the sum of these terms to equal the constant $-k^2$, each term must itself be a constant. These constants are defined as follows:

$$k_x^2 = -\frac{1}{f}\frac{d^2f}{dx^2} \quad \Rightarrow \quad \frac{d^2f}{dx^2} = -k_x^2 f \tag{3.10}$$

$$k_y^2 = -\frac{1}{g}\frac{d^2g}{dy^2} \quad \Rightarrow \quad \frac{d^2g}{dy^2} = -k_y^2 g \tag{3.11}$$

$$k_z^2 = -\frac{1}{h}\frac{d^2h}{dz^2} \quad \Rightarrow \quad \frac{d^2h}{dz^2} = -k_z^2 h. \tag{3.12}$$

Equation 3.9 then becomes,

$$k_x^2 + k_y^2 + k_z^2 = k^2. \tag{3.13}$$

The solutions to (3.10) (3.11) (3.12) and (3.13) can take a number of forms. If there is a travelling wave in the x-direction, the form of $f(x)$ is [56],

$$f_1(x) = A_1 e^{-jk_x x} + B_1 e^{+jk_x x}, \tag{3.14}$$

where A_1 and B_1 are constant coefficients. If there is a standing wave in the x-direction, the form of $f(x)$ will be,

$$f_2(x) = C_1 \cos(k_x x) + D_1 \sin(k_x x), \tag{3.15}$$

where C_1 and D_1 are constant coefficients. Standing and travelling waves include fields for many practical applications such as resonators, filters, and multiplexers.

Similarly, the forms of $g(y)$ and $h(z)$ for travelling and standing waves respectively are,

$$\begin{aligned} g_1(y) &= A_2 e^{-jk_y y} + B_2 e^{+jk_y y} \\ g_2(y) &= C_2 \cos(k_y y) + D_2 \sin(k_y y) \\ h_1(z) &= A_3 e^{-jk_z z} + B_3 e^{+jk_z z} \\ h_2(z) &= C_3 \cos(k_z z) + D_3 \sin(k_z z). \end{aligned}$$

For the linear expansion case described above, the geometry is expanding uniformly in each direction.

Consider the expanded geometry after a temperature change ΔT described on a scaled coordinate system (x', y', z') where,

$$x' = (1 + \alpha\Delta T)x \tag{3.16}$$

$$y' = (1 + \alpha\Delta T)y \tag{3.17}$$

$$z' = (1 + \alpha\Delta T)z. \tag{3.18}$$

The solution to the wave equation described in the (x', y', z') coordinate system is identical to the original solution since the scaling of the coordinate system accounts for the expansion of the geometry.

Let the phase constant after a temperature change ΔT be,

$$k'^2 = k_x'^2 + k_y'^2 + k_z'^2. \tag{3.19}$$

Consider a travelling wave in the x-direction after a temperature change ΔT. This behaviour is described by (3.14), which re-written in the expanded coordinate system is,

$$f_1 = A_1 e^{-jk_x' x'} + B_1 e^{+jk_x' x'} = A_1 e^{-jk_x x} + B_1 e^{+jk_x x}. \tag{3.20}$$

Transposing the left hand side of (3.20) back to (x, y, z) using (3.16), (3.17), and (3.18),

$$A_1 e^{-jk_x'(1+\alpha\Delta T)x} + B_1 e^{+jk_x'(1+\alpha\Delta T)x} = A_1 e^{-jk_x x} + B_1 e^{+jk_x x}.$$

By inspection,

$$k_x = k_x'(1 + \alpha\Delta T). \tag{3.21}$$

Alternatively consider a standing wave in the x-direction. This behaviour is described by (3.15), which re-written in the expanded coordinate system is,

$$f_2 = C_1 \cos(k'_x x') + D_1 \sin(k'_x x') = C_1 \cos(k_x x) + D_1 \sin(k_x x). \tag{3.22}$$

Transposing the left hand side of (3.22) to the (x, y, z) coordinate system using (3.16), (3.17), and (3.18),

$$C_1 \cos(k'_x(1 + \alpha\Delta T)x) + D_1 \sin(k'_x(1 + \alpha\Delta T)x) = C_1 \cos(k_x x) + D_1 \sin(k_x x).$$

By inspection,

$$k_x = k'_x(1 + \alpha\Delta T). \tag{3.23}$$

Since (3.21) (3.23) are identical, the same relationship exists for both standing and travelling waves.

It can similarly be shown in the y and z direction that,

$$k_y = k'_y(1 + \alpha\Delta T) \tag{3.24}$$

$$k_z = k'_z(1 + \alpha\Delta T). \tag{3.25}$$

Substituting (3.23) (3.24) and (3.25) into (3.13),

$$\begin{aligned} ((1 + \alpha\Delta T)k'_x)^2 + ((1 + \alpha\Delta T)k'_y)^2 + ((1 + \alpha\Delta T)k'_z)^2 &= k^2 \\ ((1 + \alpha\Delta T)^2(k'^2_x + k'^2_y + k'^2_z)^2 &= k^2, \end{aligned}$$

and substituting (3.19),

$$\begin{aligned} ((1 + \alpha\Delta T)^2(k')^2 &= k^2 \\ k' &= \frac{k}{1 + \alpha\Delta T}, \end{aligned} \tag{3.26}$$

Defining $f(\Delta T)$ as the frequency after temperature change ΔT then,

$$k' = 2\pi f(\Delta T)\sqrt{\mu\epsilon}. \tag{3.27}$$

Substituting (3.27) and (3.2) into (3.26),

$$f(\Delta T) = \frac{f}{1 + \alpha\Delta T}. \tag{3.28}$$

Consider a frequency point of interest f_o (for example a band edge frequency or centre frequency for a filter, or resonant frequency for a cavity). A change of ΔT will cause a frequency shift of,

$$\begin{aligned}\Delta f = f(\Delta T) - f_o &= \frac{f_o}{1+\alpha\Delta T} - f_o \\ &= \frac{-\alpha\Delta T f_o}{1+\alpha\Delta T}.\end{aligned} \tag{3.29}$$

The fractional frequency change with respect to temperature change, or temperature drift, is given by,

$$\delta = \frac{\Delta f}{f_o \Delta T}.$$

Substituting (3.29),

$$\delta = \frac{-\alpha}{1+\alpha\Delta T}. \tag{3.30}$$

When the CTE α is small (as is commonly the case), the denominator of (3.30) is nearly unity, The temperature drift is therefore approximately $-\alpha$. Consider for example an aluminum filter with a CTE of $23\,\mathrm{ppm}/^{\circ}\mathrm{C}$. The temperature drift for the filter over a $100\ ^{\circ}\mathrm{C}$ temperature change is therefore,

$$\delta = \frac{-23 \times 10^{-6}}{1 + -23 \times 10^{-6} \cdot 100} = -23.05 \times 10^{-6} \cong -\alpha.$$

The temperature drift is therefore approximately linear with respect to temperature.

3.2 Generalized Temperature Drift in a Lossy Source-Free Medium

The derivation above assumes wave propagation in a lossless medium. Consider the component wave equations for a lossy medium [56],

$$\begin{aligned}\nabla^2 E_x(x,y,z) - \gamma^2 E_x(x,y,z) &= 0 \\ \nabla^2 E_y(x,y,z) - \gamma^2 E_y(x,y,z) &= 0 \\ \nabla^2 E_z(x,y,z) - \gamma^2 E_z(x,y,z) &= 0\end{aligned}$$

where the propagation constant γ is,

$$\gamma^2 = j\omega\mu\left(\sigma + j\omega\varepsilon\right). \tag{3.31}$$

The wave equations in a lossy medium are analogous to the lossless wave equations (3.4), (3.5), and (3.6) with $\gamma \propto k$. It can easily be shown using the procedure described above that,

$$\gamma' = \frac{\gamma}{1+\alpha\Delta T}, \tag{3.32}$$

where γ' is the attenuation constant after a temperature change ΔT.

Substituting (3.31) into the square of (3.32),

$$j\omega'\mu\sigma - \omega'^2\mu\varepsilon = \frac{j\omega\mu\sigma}{\left(1+\alpha\Delta T\right)^2} - \frac{\omega^2\mu\varepsilon}{\left(1+\alpha\Delta T\right)^2} \tag{3.33}$$

where ω' is the angular frequency after a temperature change ΔT.

Assume that (3.28) is approximately true for a lossy source-free medium so,

$$\begin{aligned} f(\Delta T) &= \frac{f}{1+\alpha\Delta T} \\ \omega' &= \frac{\omega}{1+\alpha\Delta T}. \end{aligned} \tag{3.34}$$

To test this hypothesis, substitute (3.34) into (3.33).

$$\begin{aligned} \frac{j\omega\mu\sigma}{1+\alpha\Delta T} - \frac{\omega^2\mu\varepsilon}{\left(1+\alpha\Delta T\right)^2} &= \frac{j\omega\mu\sigma}{\left(1+\alpha\Delta T\right)^2} - \frac{\omega^2\mu\varepsilon}{\left(1+\alpha\Delta T\right)^2} \\ \frac{j\omega\mu\sigma}{1+\alpha\Delta T} &= \frac{j\omega\mu\sigma}{\left(1+\alpha\Delta T\right)^2} \end{aligned} \tag{3.35}$$

Since $(1+\alpha\Delta T) \cong 1$, then $(1+\alpha\Delta T) \cong (1+\alpha\Delta T)^2$. Therefore (3.35) is approximately true, confirming the above hypothesis.

Equation 3.28 is therefore strictly true for the lossless source-free case, and approximately true for the lossy source-free case. This approximation improves as $\alpha\Delta T$ approaches zero. From (3.35) it can be seen that this approximation is equally valid for high or low loss for a given CTE.

Consider for example the four-pole inductive-iris aluminum waveguide filter shown in Figure 3.1. This WR62 filter (0.311" height, 0.622" width) has resonator lengths 0.42", 0.467", 0.467" and 0.42". Iris widths are 0.2975", 0.19", 0.19" and 0.2975".

The CTE of aluminum is $23\ \mathrm{ppm}/^{\circ}\mathrm{C}$ [55], and the conductivity is $2.326 \times 10^{7}\ \mathrm{S}/\mathrm{m}$ [57]. Assuming linear unconstrained expansion, the geometry after a temperature change ΔT will be scaled by a factor of $(1 + \alpha\Delta T)$.

In Ansoft HFSS, the geometry can therefore be specified in terms of the CTE and the temperature change. This parameterized geometry can then be used to simulate filter response after a temperature change ΔT.

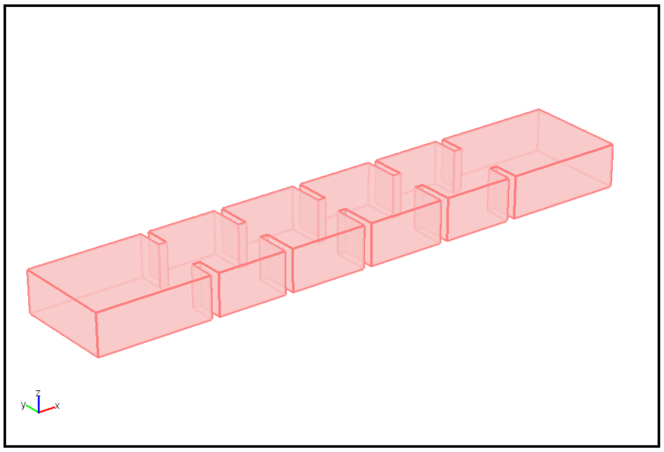

Figure 3.1: An inductive iris WR62 waveguide filter

Figure 3.2 shows the simulated filter response on the nominal geometry, the simulated filter response on geometry after a $100\ ^{\circ}\mathrm{C}$ temperature change, and the calculated filter response using (3.28). Figure 3.2 clearly shows that (3.28) provides an excellent approximation of the filter drift for a CTE of $23\ \mathrm{ppm}/^{\circ}\mathrm{C}$. Since the calculated drift shows excellent agreement for a high CTE material like aluminum, it can be concluded that (3.28) can be used to calculate temperature drift for any passive device with a uniform CTE.

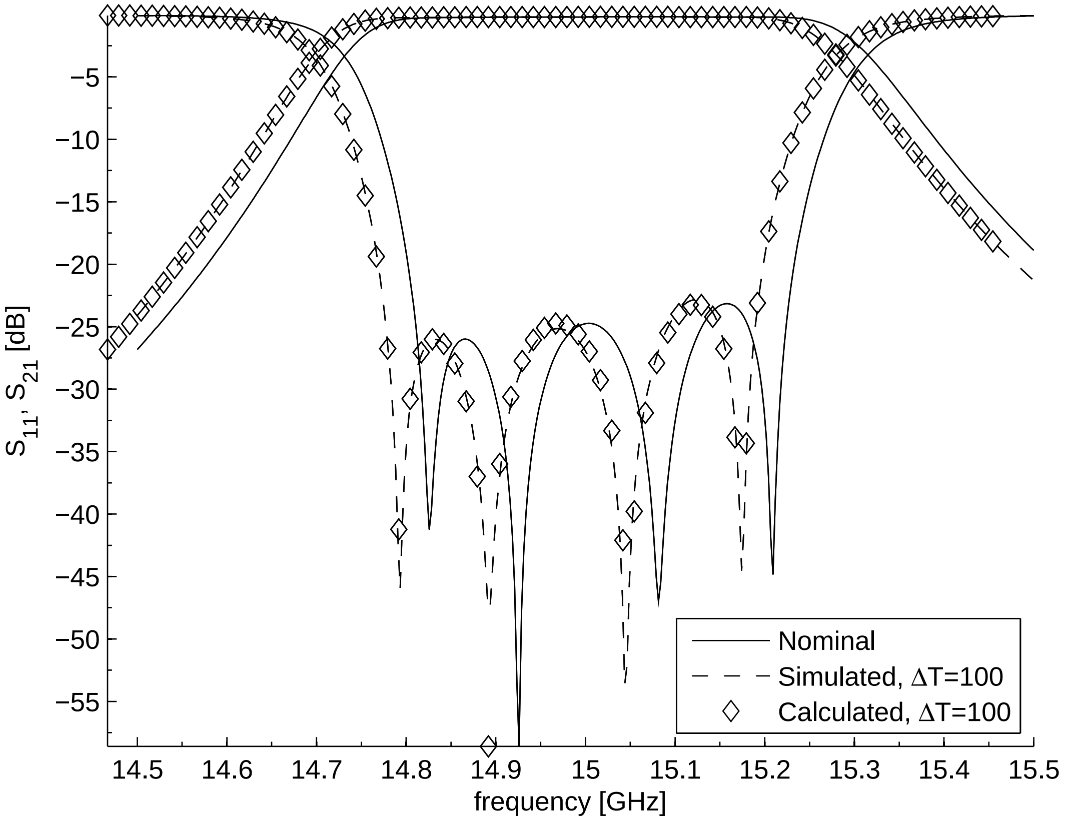

Figure 3.2: Drift for a lossy aluminum filter

3.3 Iris Expansion and Coupling Drift

Consider a coupled-resonator filter in which the resonators are perfectly compensated. If resonance is perfectly corrected, does the effect of iris expansion on coupling cause significant temperature drift?

Coupling and input resistance can be expressed in terms of the coupling coefficient M, which is proportional to the magnetic polarizability [58].

Consider a rectangular iris with length a and width b. In [59], Cohn shows that the term M/a^3 is constant for a given aspect ratio b/a for a thin iris. These values are determined for a range of aspect ratios in [59] and more recently in [60]. Similar relationships have been derived for other iris shapes.

Assuming unconstrained linear expansion, thermal expansion does not change the aspect ratio of the iris. Therefore, the term M/a^3 is also constant with respect to temperature.

The coupling $M(\Delta T)$ after some temperature change ΔT is,

$$\frac{M(\Delta T)}{[a(1+\alpha\Delta T)]^3} = \frac{M}{a^3}$$

where α is the CTE of the iris material. The ratio of the pre- and post-expansion coupling is,

$$\frac{M(\Delta T)}{M} = (1+\alpha\Delta T)^3 \tag{3.36}$$

According to Equation 3.36, the coupling for a rectangular iris constructed from aluminum ($\alpha = 23$ ppm/°C) will increase by 0.7% with a 100 °C temperature increase. A temperature increase of 145 °C produces a 1% increase in the coupling coefficient.

The coupling drift predicted by Equation 3.36 can be confirmed using full wave EM simulations. The coupling coefficient is determined by calculating the eigenfrequencies f_m and f_e for a cavity, replacing the centre of the iris with a magnetic wall, and electric wall respectively. The coupling coefficient is then,

$$k = \frac{f_e - f_m}{f_e + f_m} \tag{3.37}$$

Consider a WR-62 waveguide cavity, 0.661 inches in length, with a rectangular iris 0.2 inches by 0.1 inches. A finite element eigenfrequency simulation finds that,

$$f_e = 13.0256\text{GHz}\ ,\ f_m = 12.78595\text{GHz}$$

From Equation 3.37, the coupling coefficient is,

$$k = 0.009285$$

For an aluminum iris ($\alpha = 23$ ppm$/°\mathrm{C}$) experiencing a $145°\mathrm{C}$ temperature increase, the iris dimensions increase by a factor of $(1 + \alpha\Delta T)$. A perfectly compensated cavity is assumed, so the cavity dimensions are left unchanged. A simulation similar to that performed on the nominal iris provides the coupling coefficient,

$$k = 0.009378$$

which corresponds to a 1% increase in coupling, as predicted by Equation 3.36.

It is useful to determine the effect of a 1% increase in coupling on filter response. Consider a four-pole cavity filter with no transmission zeros and the following characteristics: an $1200\ \mathrm{MHz}$ centre frequency, $120\ \mathrm{MHz}$ bandwidth, and $0.01\ \mathrm{dB}$ passband ripple.

Using the coupling-matrix model, the diagonal elements of the coupling matrix are zero for tuned resonators. By scaling the coupling coefficients and input/output resistance by a factor of $(1 + \alpha\Delta T)^3$, the effect of coupling drift can be modelled.

The drift of the coupling coefficients caused by iris expansion causes the lower band-edge frequency of this filter to drift by -0.12 ppm$/°\mathrm{C}$. The upper band-edge drifts by $+0.12$ ppm$/°\mathrm{C}$, each over a $145\ °\mathrm{C}$ temperature change. An uncompensated aluminum filter will drift at -23 ppm$/°\mathrm{C}$. The isolated drift from iris expansion is unlikely to be a significant factor in the temperature drift problem.

Furthermore, near-perfect compensation of the resonators would be required for the drift caused by iris expansion to be even distinguishable. The contribution to temperature drift of iris expansion in a waveguide filter can therefore be ignored when compensating for temperature drift.

3.4 Metrics for Temperature Drift

When studying temperature drift and temperature compensation, it is important to have clearly defined metrics for measuring and describing drift. In this work, temperature-drift metrics are classified with respect to the thermal conditions of the piece under test.

3.4.1 Uniform Temperature Distribution

An uncompensated device constructed from a single material that is allowed to expand linearly will drift according to Equation 3.28. Equation 3.28 states that a frequency point of interest f_o will vary with temperature change ΔT according to,

$$f(\Delta T) = \frac{f_o}{(1 + \alpha \Delta T)}$$

where α is the linear coefficient of thermal expansion. This equation is valid for any frequency point of interest; for example band-edges or centre frequency for a filter, or resonant frequency for a cavity.

Since $\alpha \Delta T$ is much less than unity, $f(\Delta T)$ is approximately linear with respect to ΔT (c.f. (3.29)). Temperature drift is defined as the slope of the frequency-temperature curve indexed to some nominal frequency. The nominal frequency f_o is defined as the frequency where ΔT is zero.

Temperature drift is therefore defined as,

$$\delta = \frac{\Delta f}{f_o \Delta T}.$$

Figure 3.3 shows the resonant frequency drift of a rectangular aluminum resonant cavity in simulation (HFSS).

The units of temperature drift are $^{\circ}\mathrm{C}^{-1}$. However, drift is most often specified in parts per million per degree Celsius (ppm/$^{\circ}$C). This allows typical values for temperature drift to be expressed in whole numbers.

A compensated resonator or filter may not exhibit a linear response with respect to temperature. In some cases, the frequency will deviate both positively and negatively from its nominal value. Consider the temperature response of a compensated resonator shown in Figure 3.4.

Positive deviation from the nominal frequency is denoted by Δf_p, and negative deviation by Δf_n. The largest of the two deviations is denoted by Δf_{max} whose sign corresponds to the direction of frequency change. The positive, negative and maximum drifts are given by,

$$\delta_p = \frac{\Delta f_p}{f_o \Delta T},\ \delta_n = \frac{\Delta f_n}{f_o \Delta T},\ \delta_{max} = \frac{\Delta f_{max}}{f_o \Delta T} \tag{3.38}$$

The following conventions will be applied in this work for specifying non-linear temperature drift.

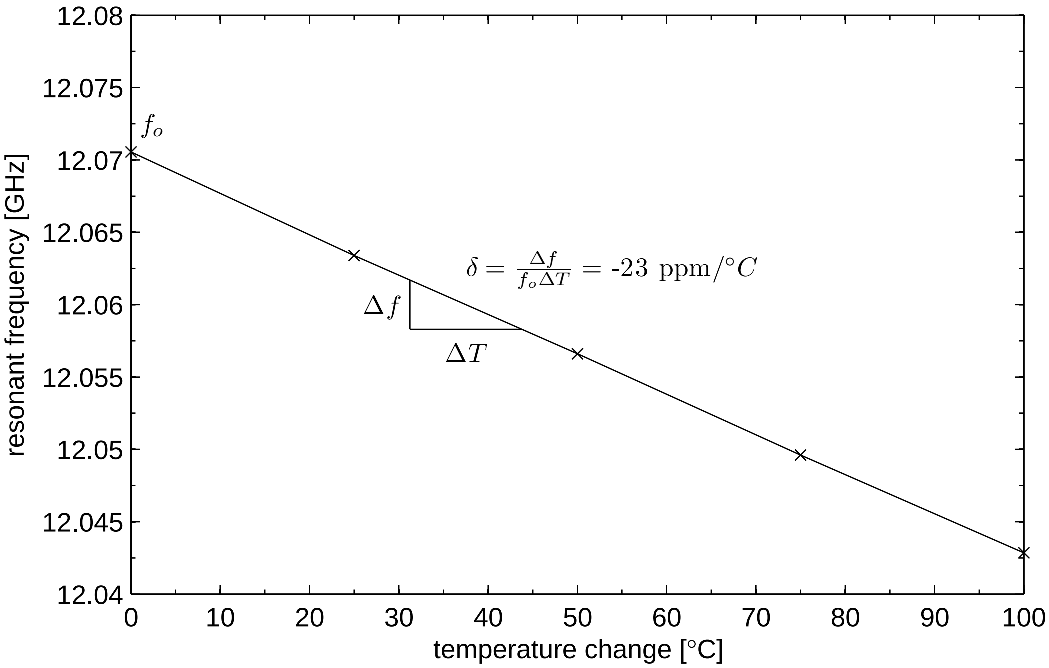

Figure 3.3: Temperature drift calculation for an uncompensated aluminum resonator

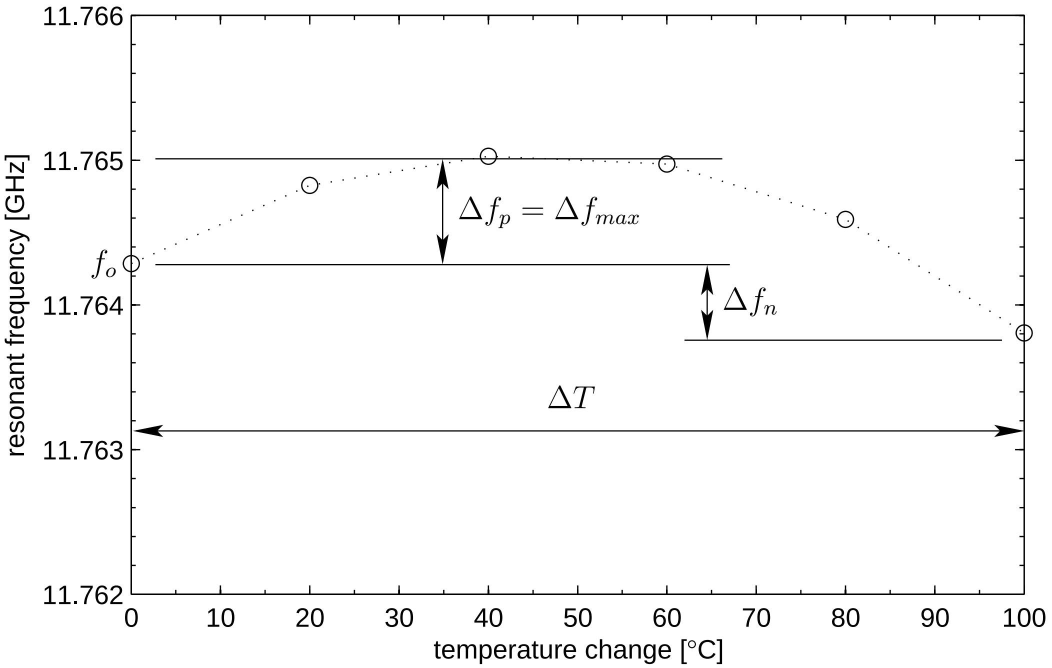

Figure 3.4: Temperature drift calculation for a compensated resonator

- If drift is in only one direction, a single drift is given, with the sign denoting the direction of drift, the same as the linear case.
- If frequency deviates both positively and negatively from the nominal frequency, drift will be specified in one of two ways.
    - Both the positive and negative deviation from the nominal frequency will be specified.
    - Alternatively, the largest deviation from the nominal frequency will be given and referred to as the *maximum drift* with the sign denoting the direction of drift. When for example a negative maximum drift is given, it is implied that there is also an unspecified (but lesser) positive deviation from the nominal frequency.

For example, the temperature drift from Figure 3.4 can be specified as either: a maximum drift of 0.63 ppm/$^\circ\mathrm{C}$ over a $100\ ^\circ\mathrm{C}$ temperature change; or as having a drift of positive 0.63 ppm/$^\circ\mathrm{C}$ and negative 0.41 ppm/$^\circ\mathrm{C}$ over a $100\ ^\circ\mathrm{C}$ temperature change.

Note that for uncompensated components, temperature drift is nearly linear in the temperature ranges expected in most RF applications. The temperature range over which drift is specified is therefore unimportant for uncompensated components; temperature drift is the same from 0 to $80\ ^\circ\mathrm{C}$ as it is from 50 to $120\ ^\circ\mathrm{C}$. This may not be the case for compensated components. It is therefore important to specify the temperature range over which drift is calculated for compensated components.

3.4.2 Non-uniform Temperature Distribution

In applications where complex thermal conditions occur, temperature distribution can be highly non-uniform. In temperature-compensated devices, this non-uniform temperature distribution can have undesirable effects on the temperature response of a device. A new definition of temperature drift is required that can quantify temperature drift under complex thermal situations.

Resistive heating is the largest contributor to non-uniform heating in RF components. Under constant input power, a modified definition of temperature drift can be used under certain thermal conditions.

Constant Input Power

In certain applications, the thermal conditions for a device can be parameterized in terms of a single varying temperature. By defining temperature drift with respect to the varying temperature parameter, the definition of temperature drift described in Section 3.4.1 can be retained. Care must be taken when comparing two devices using this approach; both devices must be subjected to the same input power and thermal conditions.

Consider for example a filter on a satellite mounted on a large heat-sink. The filter will be radiating to other equipment on the satellite whose average temperature is that of the heat sink denoted by T_{ext}.

If the heat sink is considered infinitely large, its effect can be modelled by setting the mounting faces of the filter to the temperature of the heat sink T_{ext}. All external boundaries are radiating to T_{ext}. The heat flux at the internal boundaries will be given by the resistive heating at the interior walls.

Frequency points can then be calculated over a range of external temperatures, or whichever temperature is used to parameterize thermal boundary conditions. Temperature drift is defined as in (3.38), only ΔT refers to the change in external temperature as opposed to device temperature.

$$\delta = \frac{\Delta f}{f_o \Delta T_{ext}}.$$

Generalized Temperature Drift

In some cases, it is useful to define temperature drift over a range of thermal conditions, and for a range of input power. Where input power and thermal conditions are varying, it no longer makes sense to index temperature drift to temperature change.

For these more general cases, drift can be specified in terms of normalized frequency change.

$$\delta = \frac{\Delta f}{f_o}.$$

When using this definition, the temperature range and range of input power must be specified explicitly. Where drift is not indexed to temperature change, it will be referred to in this work as *frequency drift* as opposed to temperature drift.

For example consider a compensated filter whose centre frequency drifts as shown in Figure 3.5. Again, the positive and negative drift can either be explicitly specified, or the maximum drift can be specified alone.

The filter behaviour from Figure 3.5 would be described as having either: a maximum frequency drift of -393 ppm; or a frequency drift of positive 138 ppm and negative 393 ppm in this case, input power ranging from 0.001 to 100 W, and external temperatures from 20 to 120 °C. When specifying frequency drift, the range of input power and external temperature should also be specified.

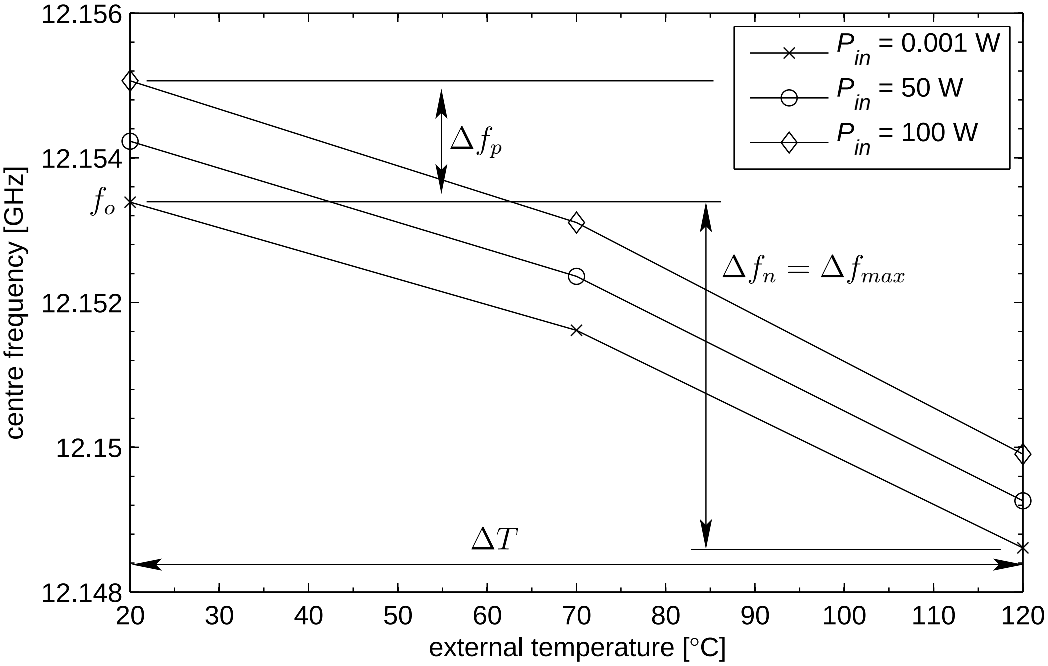

Figure 3.5: Temperature drift calculation of a compensated filter for a range of input power

Chapter 4

Bimetal Tuning Screw

Design requirements for a temperature compensation scheme are presented in this chapter. A general configuration for a variable length tuning screw is proposed that addresses these design requirements. The susceptibility of this design to vibration is evaluated using mechanical eigenmode simulation. Compensation adjustment is demonstrated in simulation for a bimetal tuning screw using Ansoft HFSS. A parameterized model is presented that can model bimetal actuation and the expansion of a compensated component.

Existing mechanisms for temperature compensation of resonators and filters presented in patents and literature tend to suffer from certain shortcomings. Some approaches provide little or no adjustment of the temperature compensation [36, 34, 43]. Adjustable compensation can account for manufacturing tolerances which can strongly influence compensation. Other approaches are inherently restricted to a particular design [28, 4], or introduce excessive mass or power consumption [22, 24, 25]. Finally, some approaches introduce possible sources of passive intermodulation [44, 46].

The following design constraints were considered when developing an approach to temperature compensation.

- **General approach:** The compensation must be general enough to be applicable to a variety resonators and filters.

- **Sufficient compensation:** There must be sufficient compensation to produce a compensated component constructed primarily from aluminum (CTE of 23 ppm$/^\circ\mathrm{C}$).

- **Adjustable compensation:** Compensation should be adjustable to account for manufacturing tolerances.

- **Limit PIM:** The approach to compensation must not present a major risk of passive intermodulation.

It is proposed that a tuning screw combined with a bimetal element can be used to produce a tuning screw with a variable effective length. Inserting a tuning screw into the side wall of a resonant cavity reduces the resonant frequency [1]. Equation 3.28 shows that an increase in temperature also results in a reduction in resonant frequency. A compensating variable length tuning screw must therefore exhibit a negative correlation between length and temperature change. This same configuration when applied to resonators in a filter, produces a compensated filter.

The configuration of the bimetal element can take a number of forms. In order for the bimetal tuning screw to exhibit a negative length-temperature correlation, the bimetal must actuate towards the cavity wall; the low-CTE layer must therefore face the cavity wall.

Possibly the simplest configuration is a cantilevered bimetal as shown in Figure 4.1. The bimetal mounting screw is flattened at the base before an angled faced is added. The facet increases the actuating length of the bimetal. A cantilevered bimetal element is mounted on a tuning screw using a spot weld so that the bimetal length is perpendicular to the edge between the facet and mounting face.

The effective length of the bimetal is l_b which is measured from the edge of the mounting face to the tip of the bimetal. This is the portion of the bimetal that is mechanically able to actuate. The width of the mounting face is w.

Another possible configuration is a double-sided bimetal, shown in Figure 4.2. This configuration is essentially two cantilevered bimetals, with two facets. A two-sided bimetal will provide more perturbation for a given effective length l_b.

4.1 Mechanical resonance

In many applications, a filter will be subjected to vibration; satellite applications in particular must survive vibration during launch. In order to gauge the bimetal tuning screw's susceptibility to vibration, it is useful to calculate its mechanical resonant frequency. The model geometry

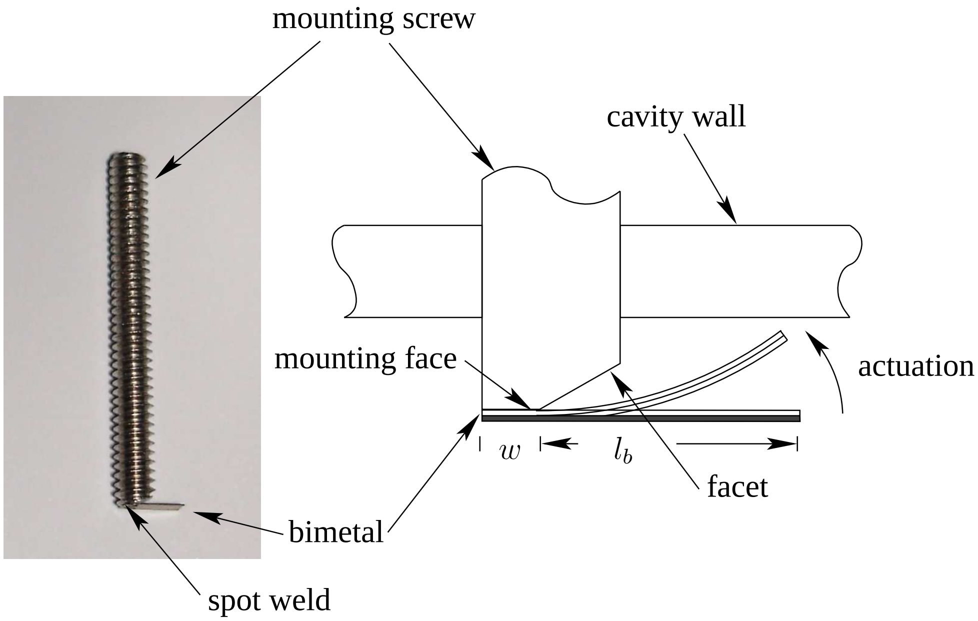

Figure 4.1: Cantilevered bimetal tuning screw, photo and diagram

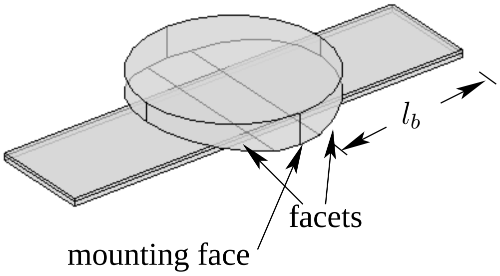

Figure 4.2: Double-sided bimetal tuning screw

used to simulate the mechanical resonance is shown in Figure 4.3. The geometry is based on the cantilevered compensator shown in Figure 4.1.

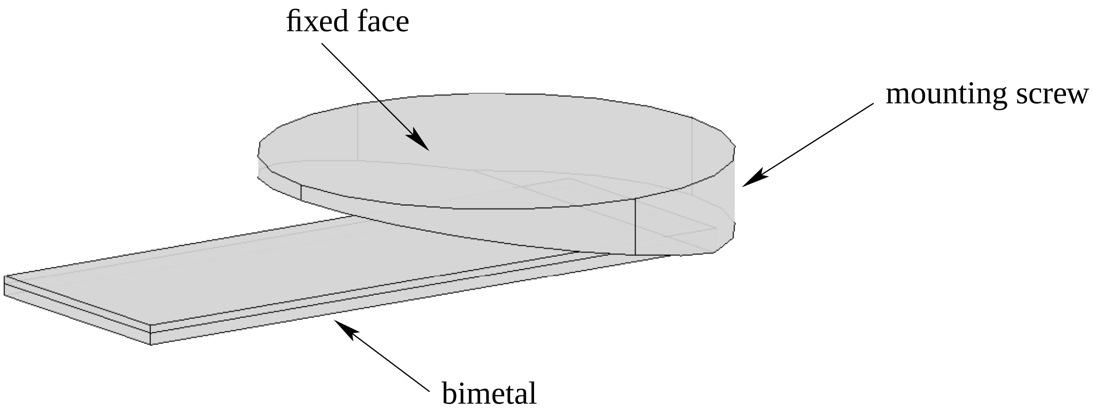

Figure 4.3: Cantilevered bimetal model for mechanical resonance simulation

The length of the bimetal mounting screw measured from the top to the mounting face is $1\ \mathrm{mm}$, and the width of the mounting face w is 0.02975”. The facet is angled at $10°$ to horizontal.

The bimetal material properties are from a commercial bimetal supplied by Engineering Materials Solutions, Truflex P675R [61], used throughout this work. The thickness of the high-expansion side (HES) is 0.03”, with a modulus of $12.41\ \mathrm{GPa}$, and a density of $7197\ \mathrm{kg/m^3}$. The thickness of the low-expansion side (LES) is 0.02”, with a modulus of $147.55\ \mathrm{GPa}$, and a density of $8110\ \mathrm{kg/m^3}$. The bimetal mounting screw diameter is 0.119”, and material properties for 3003 aluminum are used ($147.55\ \mathrm{GPa}$ modulus, $8110\ \mathrm{kg/m^3}$ density [57]).

Figure 4.4 shows the mechanical resonance for the geometry shown in Figure 4.3 over a range of bimetal lengths. It can be seen that mechanical resonance is over $2500\ \mathrm{Hz}$ for bimetal lengths below $4\ \mathrm{mm}$. The bimetal lengths shown in Figure 4.4 cover the range of lengths that will be practical for bimetal compensation.

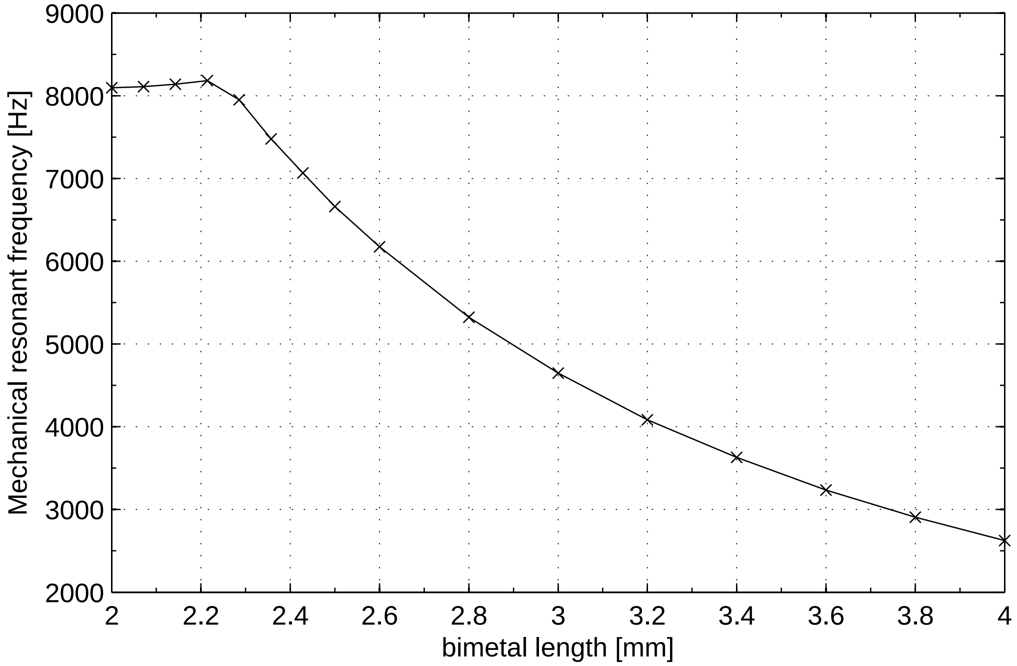

Figure 4.4: Bimetal length sweep for first mode of mechanical resonance

A typical mechanical test for space qualification will comprise two types of vibration tests; sinusoidal and random [62]. In [62], frequency is gradually increased from 10 to 100 Hz. Since the fundamental mechanical resonance of the bimetal compensator is so much higher than test frequencies, the magnitude of any resonant excitation will be small.

4.2 Modelling Compensation Adjustment

Manufacturing tolerances have significant impact on microwave components. If compensation is easily adjustable, the level of compensation can be modified to account for these effects. For the bimetal tuning screw described here, increasing the length of a bimetal strip will provide increased actuation, and thus increased compensation. Once a bimetal tuning screw has been constructed, the amount of compensation can also be tuned by adjusting the depth of the bimetal screw.

Since the field nearer the centre of a resonator is stronger than the field near the walls. A bimetal tuning screw actuating at this increased depth will therefore provide increased field perturbation, and therefore increased compensation. This tunability allows for adjustment of compensation during the filter tuning process, so that manufacturing tolerances can be accounted for.

Consider a bimetal tuning screw with a diameter d, and tp threads per inch. The depth of the bimetal tuning screw can be parameterized as follows to model the turning of the mounting screw. Assume that the bimetal is parallel to the cavity length for a rotation angle $\beta = 0$, as shown in Figure 4.5.

The nominal bimetal depth is bd_o, measured form the cavity wall to the top of the bimetal strip. The bimetal depth can be parameterized with respect to screw rotation angle β as,

$$bd = bd_o + \frac{\beta}{tp \times 360}.$$

All cavity dimensions expand linearly by a factor of $(1 + \alpha \Delta T)$.

The actuation of the bimetal can also be parameterized with respect to ΔT, and either flexivity or specific deflection. By assuming a constant radius of curvature, and using (2.27) or (2.25), the actuation of the bimetal can be fully parameterized. This model can be implemented in Ansoft

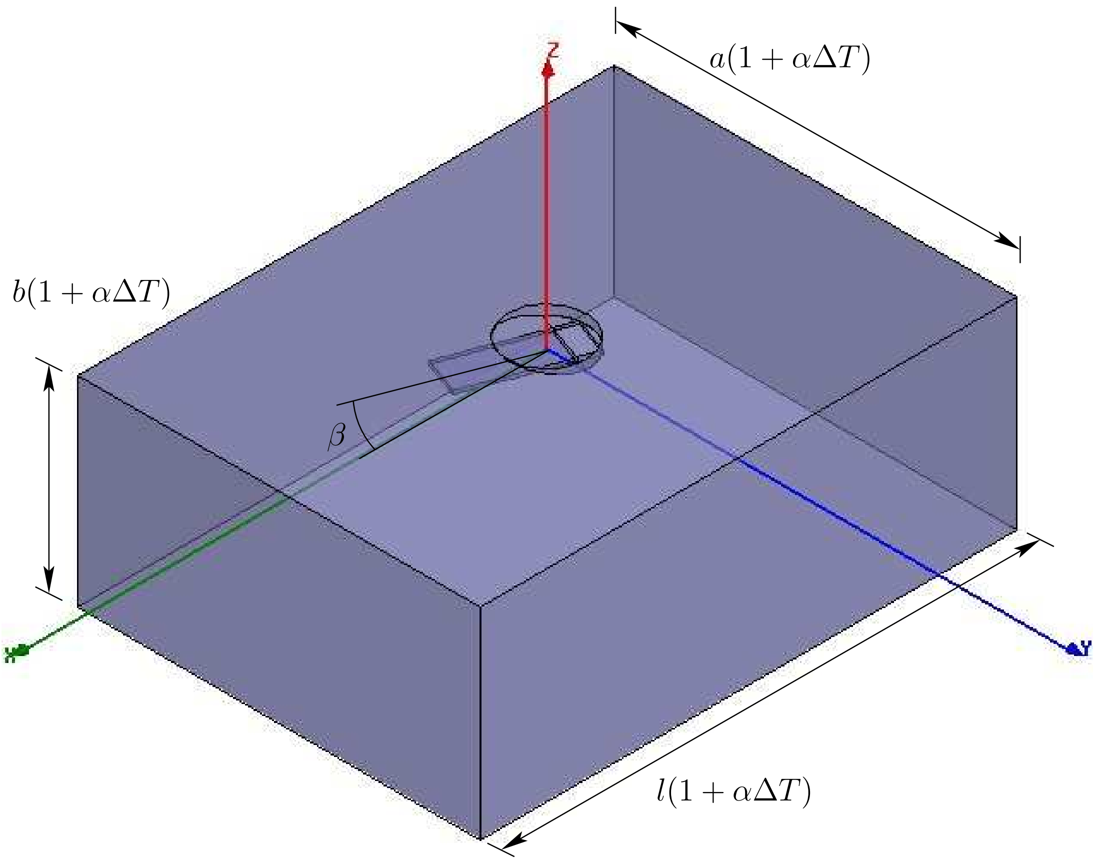

Figure 4.5: Parameterized model for simulating compensation tuning

HFSS since it allows for parameterized geometries. (This modelling approach is described in detail in section 4.3.)

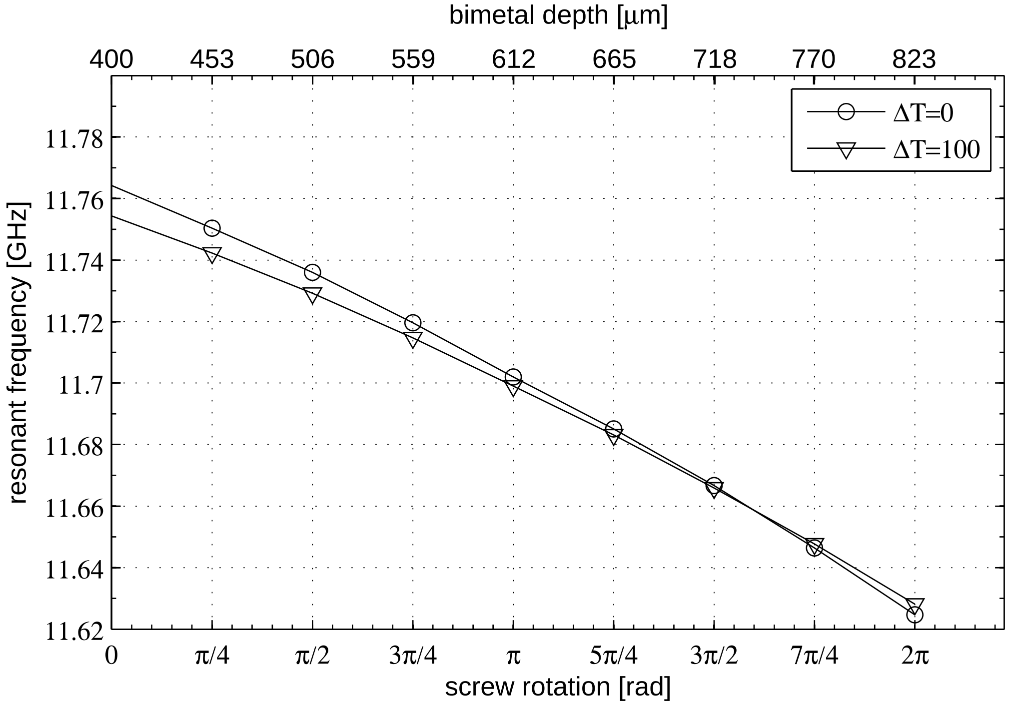

Figure 4.6: Resonant frequency v.s. bimetal mounting-screw rotation

Figure 4.6 shows the simulated resonant frequency for one full bimetal rotation using the model described above, at $\Delta T = 0\ ^\circ\mathrm{C}$ and at $\Delta T = 100\ ^\circ\mathrm{C}$. The bimetal diameter d is 0.122 inches, and tp is 60 threads per inch. A nominal depth of 0.4 mm is used with a bimetal length of 3.8 mm, and a flexivity of 2.07×10^{-5} °F^{-1}. A WR62 cavity is used, so the cavity width is 0.311" and the height is 0.622". The nominal cavity length is 0.83". The difference between the two lines at each point denotes the drift (although the drift is not linear with respect to temperature). The cavity is compensated at the intersection between the two lines.

It can be seen from Figure 4.6 that the cavity is compensated at a screw rotation between 270° and 315°. Figure 4.7 shows the resonant frequency with respect to temperature at a rotation of 270°.

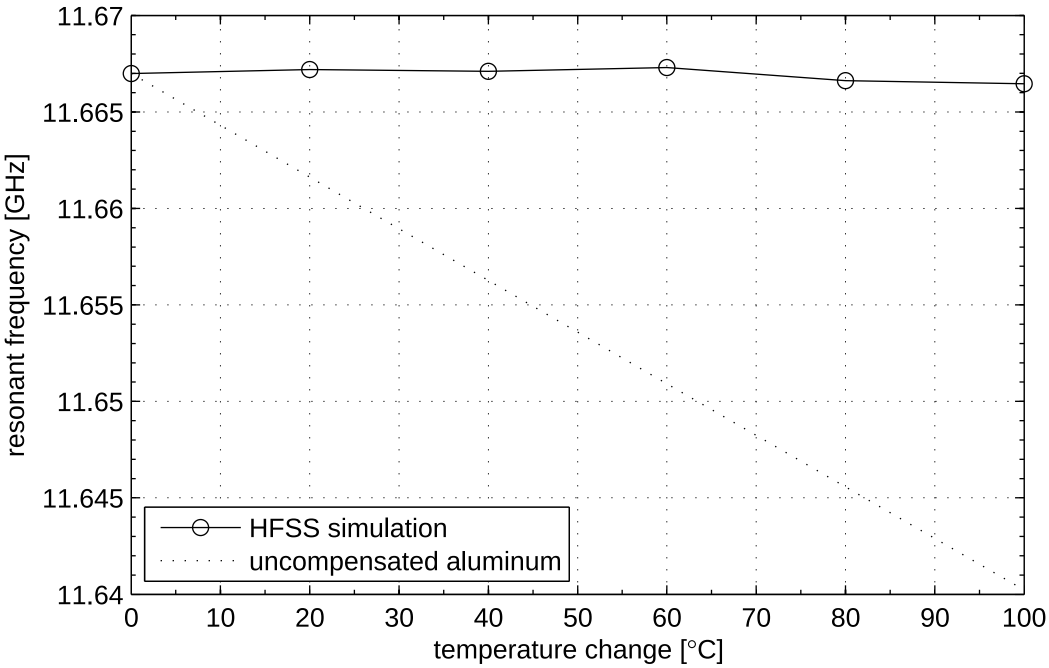

Figure 4.7: Temperature sweep with bimetal mounting-screw positioned at 270°

Field perturbation in the side wall of a cavity will decrease resonant frequency [1]. Increasing the depth of the bimetal without rotation will therefore smoothly decrease resonant frequency. Since a screw is used to change the bimetal depth, rotation will also occur. From Figure 4.6 it can be seen that the perturbation response of the resonant frequency is smooth, despite bimetal rotation. Any effect of rotation is overwhelmed by the depth change.

It can be seen that any variation in resonant frequency caused by the rotation of the cantilevered bimetal is masked by the effect of the depth change. Rotating the bimetal mounting screw can therefore be used as an effective method for adjusting compensation.

4.3 A parameterized model for a bimetal-compensated resonator

Consider a cantilevered bimetal inserted into the side of a rectangular resonant cavity through the broad wall as described in Chapter 4. The resonant frequency of a cavity decreases as it thermally expands. Side-wall perturbation also decreases resonant frequency. In order to compensate for temperature drift, the bimetal actuation should therefore provide lower perturbation as temperature increases. The low CTE side must therefore face the cavity wall, so that the bimetal actuates towards the wall.

Figure 4.8 shows the bimetal strip in a relative coordinate system where actuation occurs in the positive z-direction. The bimetal length and width are in the positive x- and y-directions respectively. The origin of the coordinate system is at the bimetal's end-constraint, on the low-CTE side of the bimetal, closer to the cavity wall.

Assuming a constant radius of curvature, and a known specific deflection a, the entire bimetal geometry can be specified in terms of a uniform temperature change ΔT, the active bimetal length L, and thickness t.

From (2.23) and (2.24) the radius of curvature can be written in terms of the flexivity k as follows.

$$R = \frac{t}{k\Delta T}$$

Substituting (2.26),

$$R = \frac{0.53t}{a\Delta T} \tag{4.1}$$

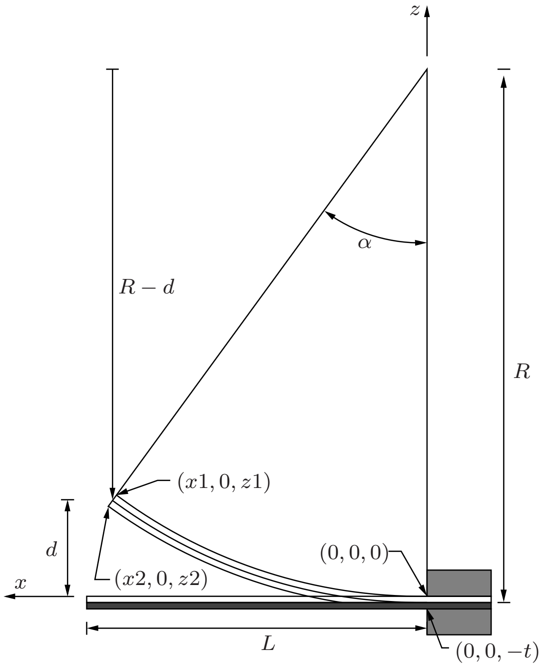

Figure 4.8: Parameterized bimetal geometry

Given the radius and the bimetal length, the radian measure of the arc-length is,

$$\alpha = \frac{L}{R}$$

The end points of the actuated bimetal $x1$, $z1$, $x2$, and $z2$ can be found as follows.

$$\begin{aligned} x1 &= (R - t/2)\sin(\alpha) \\ x2 &= (R + t/2)\sin(\alpha) \\ z1 &= d - t/2(1 - \cos(\alpha)) \\ z2 &= d - t/2(1 + \cos(\alpha)) \end{aligned}$$

These equations, along with (4.1) provide a full accounting of bimetal actuation given the specific deflection a, temperature change ΔT and the bimetal dimensions.

This parameterized model can be implemented in a full-wave RF simulator that allows for parameterized geometries (for example Ansoft HFSS). Assuming linear expansion, the remaining geometry will expand by a factor of $(1 + \alpha\Delta T)$.

Chapter 5

Experimental Setup and Measurement Procedures

An experimental setup capable of performing uniform-temperature tests is described. This test setup records and displays real-time temperature measurements, while allowing the user to control testing using software or hardware controls (or any combination thereof). This allows testing to be set up then run remotely using remote access software. The problem of post-assembly residual strains is discussed, as well as the resulting measurement hysteresis. Temperature cycling regimes designed to relieve these stresses are proposed and evaluated experimentally. General guidelines are proposed for appropriate pre-test temperature cycling. All measurements were carried out at the Centre for Integrated RF Engineering (CIRFE) at the University of Waterloo.

5.1 Experimental Setup

At test setup is required that can perform uniform-temperature tests on temperature compensated resonators and filters. The requirements for the experimental setup are as follows:

- Active heating and cooling with a range of at least $-20\ ^\circ\mathrm{C}$ to $100\ ^\circ\mathrm{C}$
- Automated data acquisition
- Programmable temperature profiles

- Test piece and ambient temperature measurement
- RF measurement capability
- Portable data format
- Remote access and control

An environmental chamber is required to provide heating and cooling. Commercially available environmental chambers offer a number of cooling methods including liquid carbon-dioxide, liquid nitrogen, and mechanical cooling. Mechanically cooled models can achieve sufficient cooling for this application. This type of cooling is also more convenient than liquid gas cooling since a gas supply is not required. For these reasons, mechanical cooling was chosen for this application. Resistive electric heating is generally used in all models.

A MicroClimate® bench-top test chamber from Cincinnati Sub-Zero was chosen; model MCB-1.2-.33-.33-H/AC [63]. Specifications for the environmental chamber are shown in Table 5.1.

The environmental chamber is controlled using a built-in Watlow 96 controller. This controller can be used to run programmable temperature cycles. An RS-485 interface can be used to run the controller remotely. This interface can be used to manually adjust and read the setpoint, read the ambient temperature, start and stop programs, as well as most other functions of the controller.

RF measurements are taken with an Agilent 8722ES vector network analyzer (VNA) which uses $3.5\ \mathrm{mm}$ coaxial test ports. The frequency range of the 8722ES is $50\ \mathrm{MHz}$ to $40\ \mathrm{GHz}$. This VNA can be controlled, and data can be read using a general purpose interface bus (GPIB) connection [64]. The programming specification is freely available so that custom software can be written by the user.

Work piece temperature will lag ambient temperature, and must therefore be measured to ensure thermal steady-state. A Fluke Omega HH506RA thermometer with a type K thermocouple is used to measure work-piece temperature. This dual-input thermometer and data-logger has a $0.1\ ^\circ\mathrm{C}$ resolution. Temperature data can be read from the thermometer using an RS-232 connection.

A diagram of the experimental setup is shown in Figure 5.1. A MATLAB program was designed to control the environmental chamber, and to acquire and store all data. The software

Table 5.1: CSZ environmental chamber specifications

Model	MCB-1.2-.33-.33-H/AC
Internal Volume	1.2 cubic feet
Temperature range	−73 °C to 190 °C
Cooling performance	−40 °C in 25 min −54 °C in 35 min −68 °C in 60 min, from 24 °C
Heating performance	24 °C to 94 °C 10 min 24 °C to 190 °C 35 min −34 °C to 24 °C 10 min −68 °C to 24 °C 15 min
Temperature stability	±0.5 °C from −50 °C to 190 °C ±1 °C below −50 °C
Controller	Watlow 96 programmable controller, RS-485 interface
Access ports	Standard 2” port located in the left wall
Electrical	115 V, 15 A, 10 ft. cord

reads and sets the setpoint for the environmental chamber through an RS-485 connection. The user can adjust the setpoint manually using the chamber's push-button controls, or using the data-logger software.

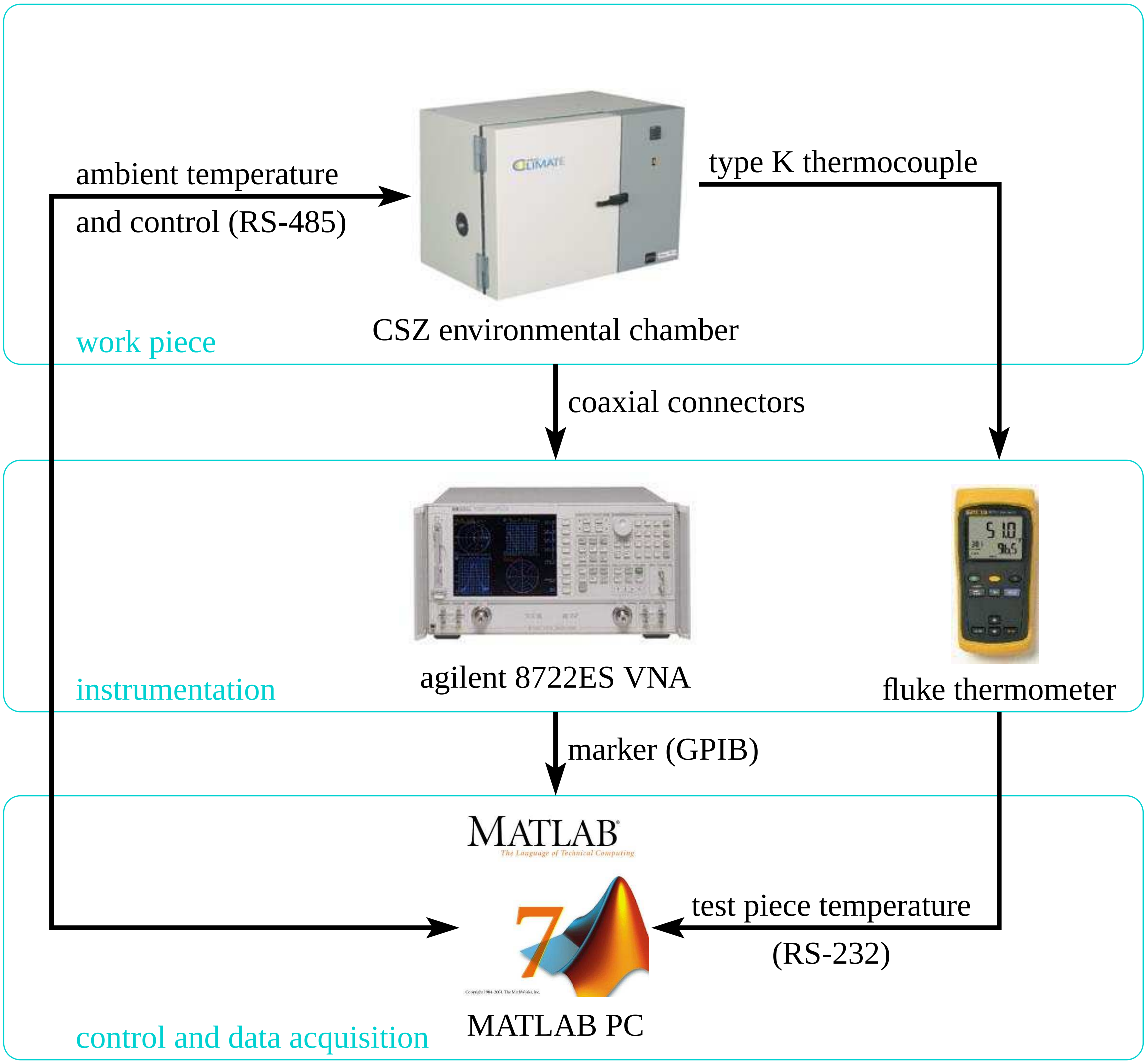

Figure 5.1: Experimental setup diagram

The work-piece temperature is read by the Fluke thermometer via a thermocouple. In some early testing, the thermocouple was affixed to the work-piece using a spot weld. Subsequently the thermocouple was affixed to the work-piece with Kapton® tape. This provided a less permanent bond, while retaining good thermal contact and retaining the bond's heat resistance. The software reads the work-piece temperature using an RS-232 connection.

The VNA is connected to the work-piece (generally a resonator or filter) with copper coaxial connectors. The VNA marker is read using a GPIB connection. The marker can be set manually by the user, or set automatically using a marker search; for example, when reading S_{11} for a resonator, a minimum marker search will measure the resonance.

All data is saved in a comma-separated plain text file, or optionally an Excel spreadsheet. The text-based comma-separated format is preferred; using portable text-based data storage ensures that data can be more easily post-processed using other software.

The data-logger software both stores, plots, and optionally displays results in real-time. Since each point is appended to the data-file immediately rather than being stored in memory, any unexpected interruption of the software does not result in complete data loss. Furthermore, the results can be observed and analysed as they are read.

Having calibrated the VNA and started the data-logger software, testing can be managed entirely from the computer, using the push-button controls on the CSZ environmental chamber, or a combination of the two. The ability to run tests entirely from the computer allows the user to manage and observe tests remotely using remote access software such as the open-source VNC [65] or Microsoft's proprietary Remote Desktop [66].

Since thermal systems tend to exhibit large time constants, testing can be extremely time consuming. The ability of this test setup to be automated and run remotely is a major advantage as it allows for unattended testing. Long tests can therefore be setup then run unattended, while allowing the user to check results, and if necessary manually adjust the testing remotely.

5.2 Experimental Procedures

Resonant frequency and filter measurements are extremely sensitive to dimensional change. Proper experimental procedures must be followed to ensure that accurate measurements are taken.

After assembly, a resonator or filter will have some residual strains that can affect thermal expansion. This can result in resonant frequency hysteresis with respect to temperature. In industry, temperature cycling is performed before any testing to relieve residual strains. This pre-cycle will eliminate any hysteresis caused by residual stresses.

Consider the temperature cycling described in Table 5.2. This pre-cycle has a $100\ ^\circ\mathrm{C}$ temperature range, with a temperature ramp of $10\ ^\circ\mathrm{C/min}$. Between temperature ramps, the setpoint is held constant for $2\ \mathrm{min}$. Holding the piece at a constant temperature is referred to as a soak.

Table 5.2: Initial pre-testing temperature cycle

Step	**Type**	**Time**	**Details**
1.	ramp	$6\ \mathrm{min}$	20 to $80\ ^\circ\mathrm{C}$, $10\ ^\circ\mathrm{C/min}$
2.	soak	$2\ \mathrm{min}$	to
3.	ramp	$10\ \mathrm{min}$	80 to $-20\ ^\circ\mathrm{C}$, $10\ ^\circ\mathrm{C/min}$
4.	soak	$2\ \mathrm{min}$	to
5.	ramp	$10\ \mathrm{min}$	-20 to $80\ ^\circ\mathrm{C}$, $10\ ^\circ\mathrm{C/min}$
6.	soak	$2\ \mathrm{min}$	to
7.	ramp	$10\ \mathrm{min}$	80 to $-20\ ^\circ\mathrm{C}$, $10\ ^\circ\mathrm{C/min}$
Total		**42 min**	

This pre-cycle was applied to an uncompensated aluminum resonator. After cycling, resonant frequency was measured with respect to temperature. The results from this testing are shown in Figure 5.2. The expected temperature drift for an uncompensated aluminum resonator with a coefficient of thermal expansion of 23 ppm/$^\circ\mathrm{C}$ is also shown. The results exhibit substantial hysteresis indicating residual strains have not been fully relieved.

Using a $10\ ^\circ\mathrm{C/min}$ temperature ramp and a $2\ \mathrm{min}$ soak does not allow sufficient time for the ambient and device temperatures to reach the ramp limits. The effective cycling range is therefore less than $100\ ^\circ\mathrm{C}$.

A longer pre-cycle is described in Table 5.3 that was designed to improve strain relief. This cycle soaks for $5\ \mathrm{min}$ between ramps to allow more time for device and ambient temperatures to reach the ramp limits. This cycle is also longer than the previous pre-cycle at $116\ \ \mathrm{min}$ from $42\ \ \mathrm{min}$.

The pre-cycle described in Table 5.3 was again applied to an uncompensated aluminum resonator. The results following this pre-cycle are shown in Figure 5.3, which shows the resonant

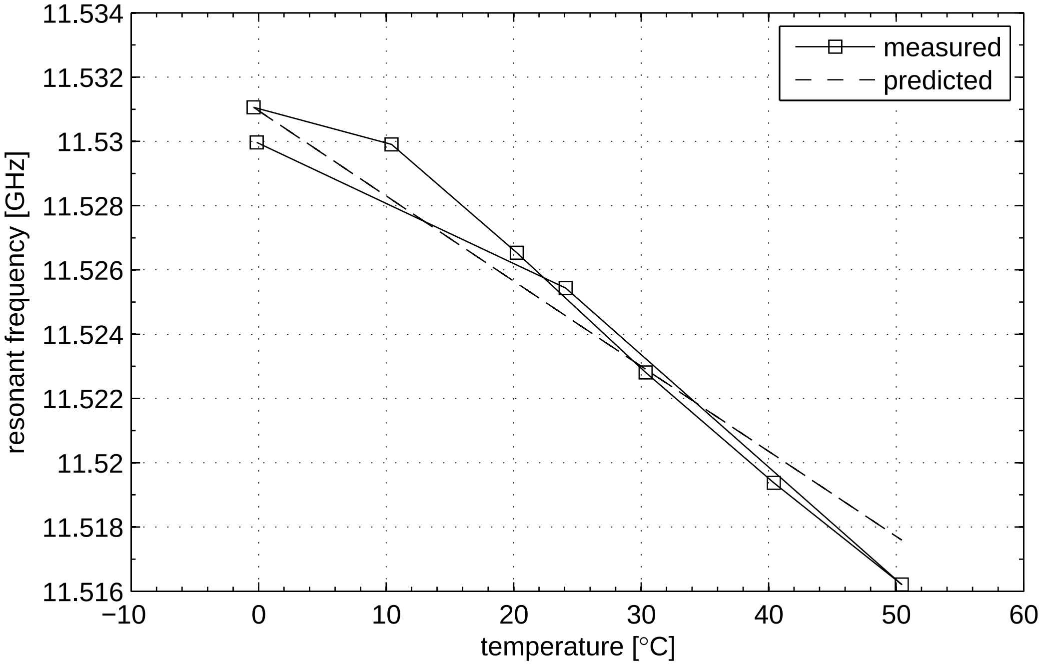

Figure 5.2: An uncompensated aluminum resonator after a 42 min pre-cycle

Table 5.3: Extended pre-testing temperature cycle

Step	**Type**	**Time**	**Details**
1.	ramp	6 min	20 — 80 °C, 10 °C/min
2.	soak	5 min	—
3.	ramp	10 min	80 — −20 °C, 10 °C/min
4.	soak	5 min	—
5.	ramp	10 min	−20 — 80 °C, 10 °C/min
6.	soak	5 min	—
7.	jump	60 min	Jump to step 3, jump count 2
3.	ramp	10 min	80 — −20 °C, 10 °C/min
2.	soak	5 min	—
Total		**116 min**	

frequency, as well as ambient, device and setpoint temperatures with respect to time. The setpoint temperature and ambient temperature read from the environmental chamber via the Watlow controller are T_{set} and T_{amb} respectively. The temperature of the device under test T_{dev} is read from the Fluke thermometer. Resonant frequency is measured by setting the VNA marker to track the minimum of the S_{11} signal. Thermal steady state occurs when the both ambient and device temperature have converged.

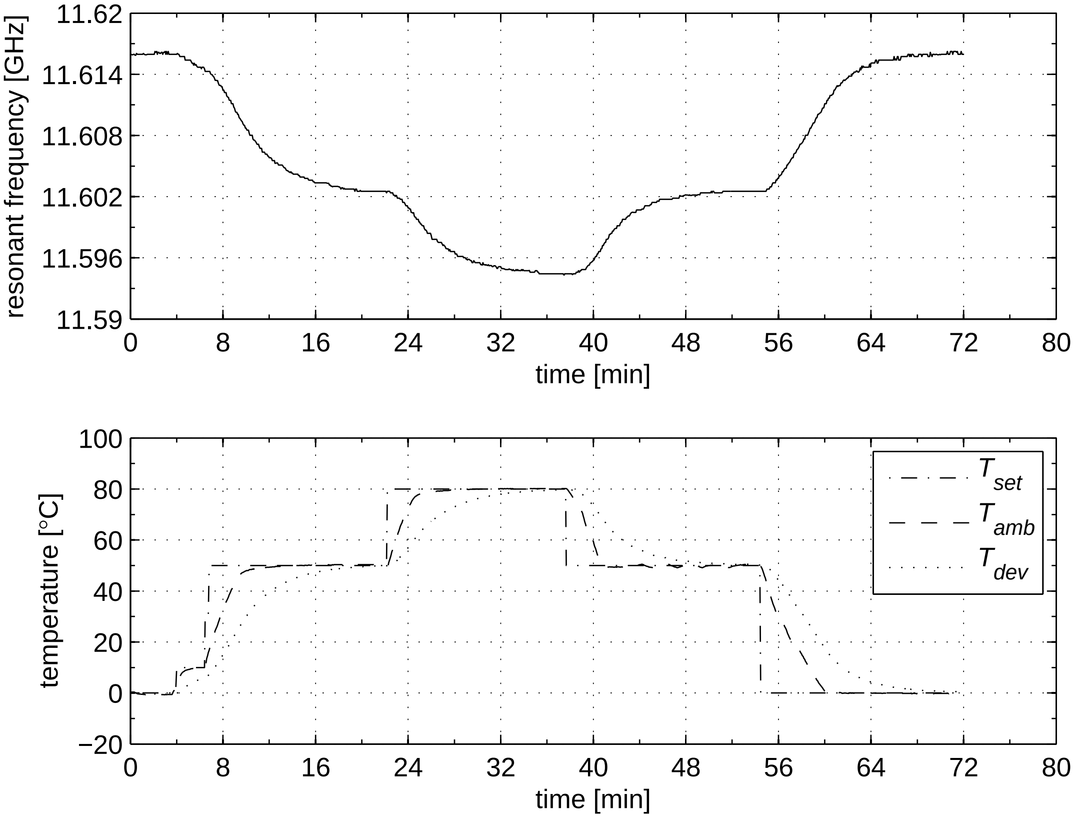

Figure 5.3: Full data set for an aluminum resonator after a $116\ \mathrm{min}$ pre-cycle

The steady state resonant frequency response from the data in Figure 5.3 is shown in Figure 5.4 along with the expected temperature drift for an uncompensated aluminum resonator with a coefficient of thermal expansion of $23\ \mathrm{ppm}/^{\circ}\mathrm{C}$. Measured drift is $-23.2\ \mathrm{ppm}/^{\circ}\mathrm{C}$ compared to a predicted drift of $-23\,\text{ppm}/^\circ\text{C}$. The longer pre-cycle has completely eliminated any hysteresis, and the measured response of the uncompensated resonator closely matches the expected drift.

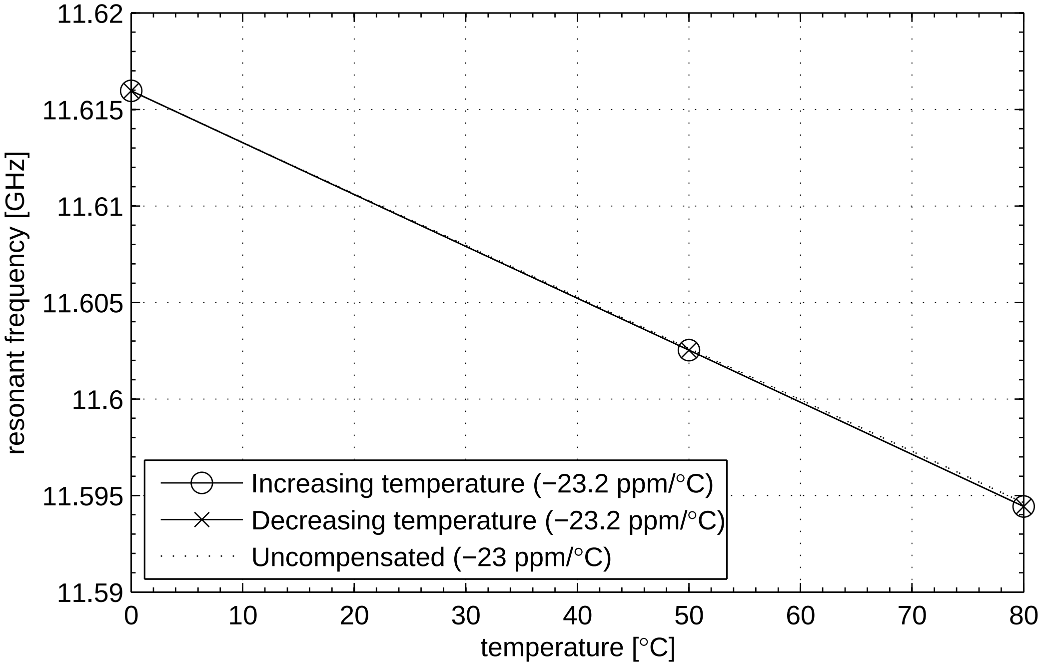

Figure 5.4: An uncompensated aluminum resonator after a $116\ \text{min}$ pre-cycle

From this and other testing experience, along with consultation with engineers in industry, the following guidelines for pre-testing thermal cycling were formed.

- Cycle temperature range should exceed the testing range
- Run cycles until the resonant frequency response is stable (5 to 10 cycles)
- More cycling will be required after tuning the component
- Ramp rate must be finite to prevent thermal shock, but the exact rate is not important
- When using a high ramp rate, ensure the soak between ramps is sufficient for the device temperature to reach the setpoint

- Further cycling is required if hysteresis if observed

Following these guidelines for temperature cycling will ensure accurate measurements for both resonators and filters, free from the effects of residual stresses.

Chapter 6

Resonator Compensation

In this chapter, bimetal compensation of a single resonator is discussed. A prototype WR-62 resonator is described. The procedure for fixturing and adjusting bimetal compensation is described. Experimental results are presented for a single bimetal-compensated resonator.

6.1 Rectangular resonator prototype

In order to prove the concept of bimetal compensation in resonators, a simple prototype resonator is required. An aluminum WR-62 waveguide cavity 0.83 inches in length is chosen for this purpose.

Figure 6.1 shows scale drawings of the prototype design. The waveguide is constructed from an upper and lower half which are connected by a bolted horizontal flange. An iris plate and end plate are also constructed from aluminum. All wall and iris thicknesses are 0.04 inches.

The prototype described in Figure 6.1 is designed so that the bimetal can be positioned arbitrarily with respect to orientation and depth. This is accomplished using nested mounting screws; an outer positioning screw, and the inner screw on which the bimetal is mounted. Locking nuts are used on each nested screw to fix them in place once adjusted. Note that the nested mounting screws were used to assess the sensitivity of the bimetal compensator to orientation.

Figure 6.2 shows a photograph of the prototype aluminum resonator. The thermocouple used to measure the device temperature is shown spot welded to the bimetal tuning screw. In later

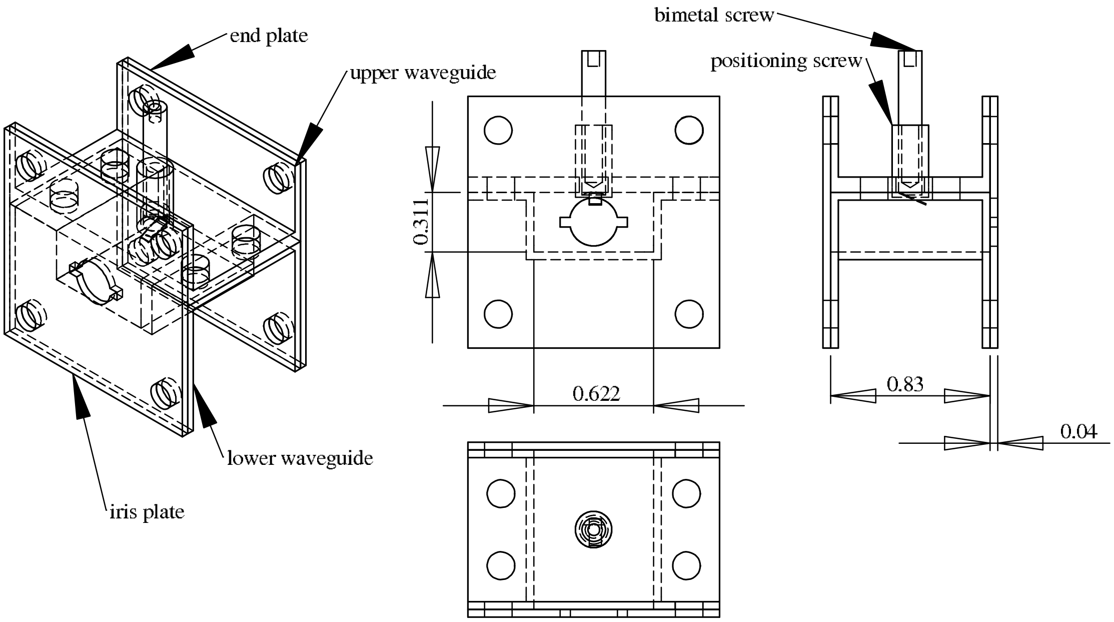

Figure 6.1: Scale drawings of the resonator prototype (1:1, all dimensions in inches)

testing, the thermocouple was affixed to the resonator itself using Kapton® tape. This allows for good thermal contact, with a less permanent and therefore more convenient fixture.

Excitation is provided by a coaxial to WR-62 transition, which is connected to the network analyzer. The external positioning screw is constructed from aluminum, however the bimetal mounting screw is a standard 4-40 steel machine screw.

6.2 Experimental Results

The resonator described in Figure 6.3 was used to implement bimetal compensation for a single resonator. The goal in implementing bimetal compensation was to minimize temperature drift while minimizing the intrusion of the bimetal into the cavity. The bimetal was mounted and adjusted as follows.

In simulation, an approximate length for the bimetal was calculated. The bimetal strip was mounted to the bimetal mounting screw. The bimetal initially was cut slightly longer than the

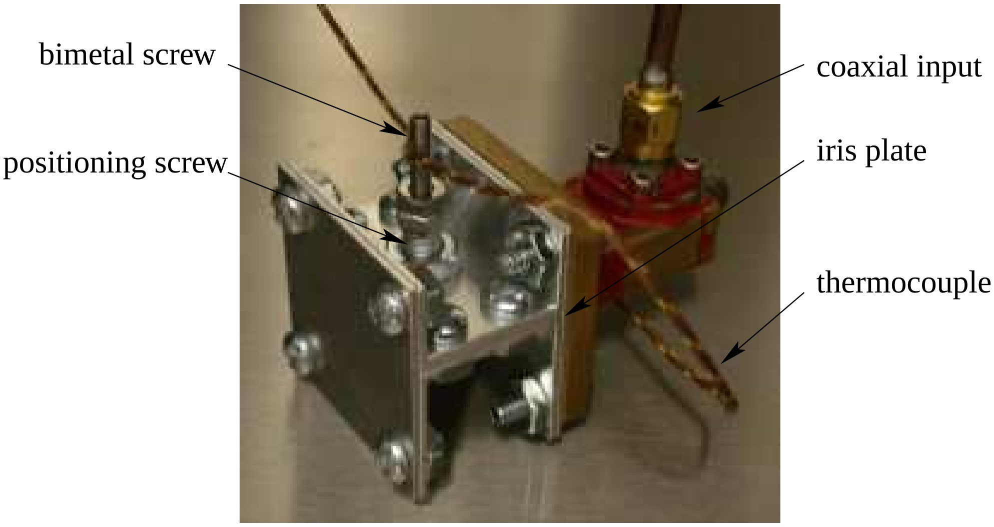

Figure 6.2: Prototype compensated resonator

desired length. The cavity should therefore be slightly over-compensated. The bimetal and positioning screw are locked using the nut so as to act as a single screw.

A zero-position for the screw is chosen so that the bimetal is as close to the cavity wall as possible, while still leaving room for actuation. The screw position is measured by inserting the screw as far as possible (until it touches the opposite wall) and noting the number of turns back from that point to the zero position.

An initial temperature cycle was performed with the bimetal at the chosen zero-position. Since the initial bimetal length is longer that the expected final length, the cavity should be over-compensated. The bimetal length is trimmed and this procedure is repeated until the resonator exhibits slightly negative temperature drift.

Since the field is stronger in the centre of the cavity, increasing the depth of the bimetal will provide increased compensation. Once the compensated cavity exhibits slightly negative temperature drift, the bimetal depth can be changed to adjust compensation so that the lowest possible temperature drift is achieved.

Figure 6.3 shows the resonant frequency drift with respect to temperature for a bimetal-compensated aluminum cavity after fixturing and adjusting the bimetal. The measured temperature drift is $-0.382\,\text{ppm}/^\circ\text{C}$ compared to an uncompensated drift of $-23\,\text{ppm}/^\circ\text{C}$. These results demonstrate that very low temperature drift can be achieved for a single resonator using bimetal compensation.

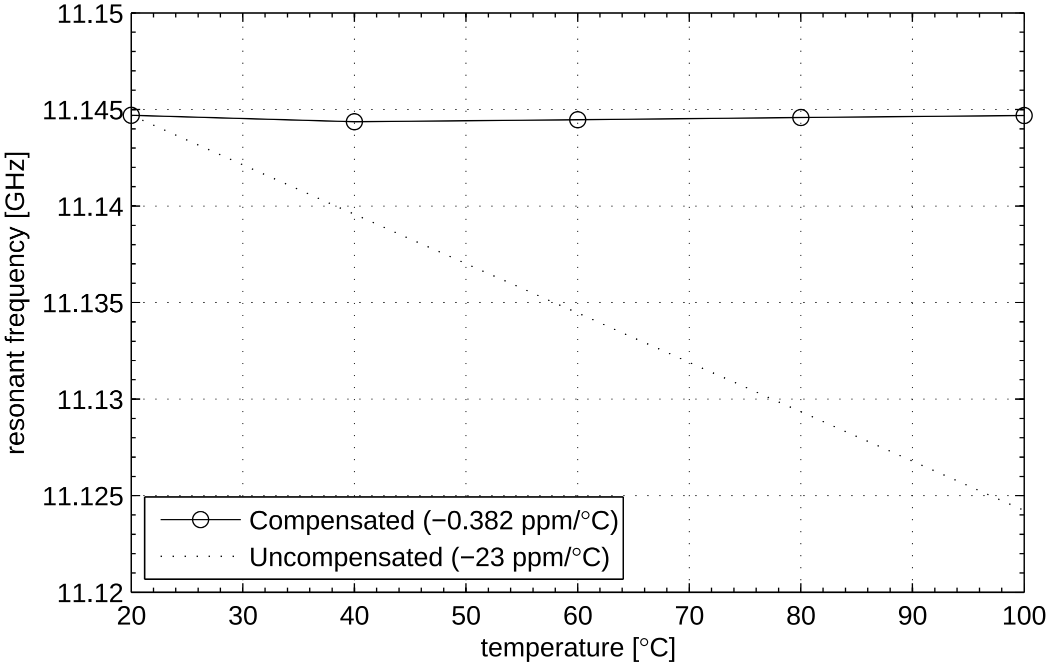

Figure 6.3: Resonant frequency response for a bimetal-compensated resonator

Chapter 7

Filter Compensation

In this chapter the implementation of bimetal compensation for a filter is described. The coupling between compensation and resonant frequency tuning is examined in simulation. A prototype bimetal-compensated filter is presented. A method for tuning filter compensation is presented which is based on the Ness method of filter tuning. Experimental results are provided for the bimetal-compensated prototype filter.

7.1 Independence of Bimetal Compensation

If bimetal-compensated resonators are to be used to produce compensated filters, implementation is simpler if compensation is independent of resonant frequency tuning. If resonant frequency tuning and compensation are found to be independent, then compensation can be adjusted followed by filter tuning without requiring iteration.

Figure 7.1 shows the simulated response of a compensated resonator using a parameterized geometry model in HFSS (c.f. Section 4.3). The response is tuned by inserting a 0.119 inch diameter tuning screw opposite the compensator to a depth of $0.5\ \mathrm{mm}$ and $1\ \mathrm{mm}$. This results in resonant frequency tuning of -0.6% and -1.8% respectively. From Figure 7.1 it can be seen that compensation is maintained as resonant frequency is tuned.

The normalized resonant frequencies for each level of tuning are shown in Figure 7.2. By superimposing the normalized resonances, the relative effect of frequency tuning on thermal compensation can be seen in more detail. The drift with no tuning is positive 0.80 ppm$/^{\circ}\mathrm{C}$

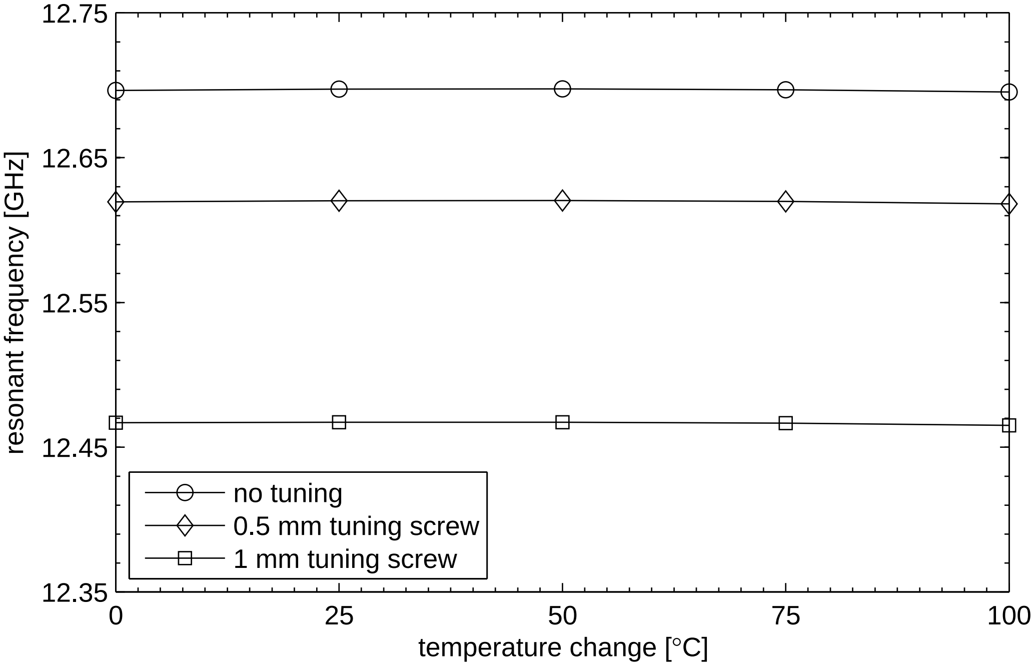

Figure 7.1: The effect of resonant frequency tuning on compensation

and negative 0.86. Inserting the tuning screw 0.5 mm, which tunes the resonant frequency by -0.6%, results in a drift of positive 0.65ppm/°C and negative 1.16ppm/°C. Finally, inserting the tuning screw 1 mm which, tunes the resonant frequency by -1.8%, results in a drift of positive 0.20 ppm/°C and negative 1.57 ppm/°C. A large resonant frequency tuning has a small effect on compensation, therefore iterative filter tuning and compensation adjustment is not required.

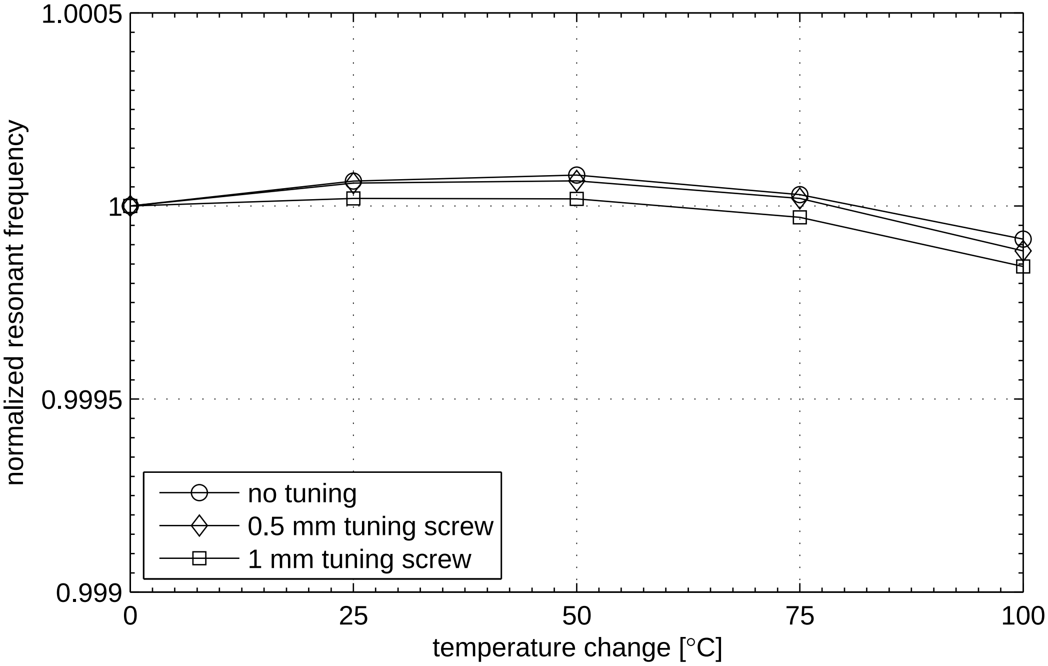

Figure 7.2: Normalized resonant frequency of a compensated resonator after tuning

7.2 Adjusting Compensation for a Filter

To implement bimetal compensation in a coupled-resonator filter, compensation must be applied and adjusted for each resonator. The resonant frequency of each cavity can not be easily obtained from the filter response. In order to adjust compensation for a filter however, the resonance of each cavity must be measured.

The following method for measuring resonance and adjusting compensation for each cavity is based on the Ness method of filter tuning [67]. If all but the first resonator are removed from a lossless Chebyshev bandpass filter, the group delay Γ_d is given by,

$$\Gamma_d = \frac{1\left(\omega^2+\omega_o^2\right) g_0 g_1}{\omega^2\left(\omega_2-\omega_1\right)\left(1+\left(g_0 g_1\right)^2\left(\frac{\omega_o}{\omega_2-\omega_1}\left(\frac{\omega}{\omega_o}-\frac{\omega_o}{\omega}\right)\right)^2\right)} \tag{7.1}$$

where ω is the angular frequency, ω_1 and ω_2 are the band edge frequencies, ω_o is the centre frequency, and g_0, g_1 are the normalized low-pass prototype values associated with the filter [67, 58]. The phase of S_{11} is,

$$\phi = -2\tan^{-1}\left(\left[-\frac{\omega_o g_1 g_0}{\omega_2-\omega_1}\left(\frac{\omega}{\omega_o}-\frac{\omega_o}{\omega}\right)\right]^{-1}\right) \tag{7.2}$$

Consider a six-pole Chebyshev filter with the characteristics shown in Table 7.1. The response of this filter calculated using the coupling-matrix model is shown in Figure 7.3. The theoretical group delay and phase at the input port for this filter with all but the first resonator removed (Equation 7.1 and Equation 7.2 respectively) are shown in Figure 7.4. The eigenfrequency of the first resonator is the frequency at which the peak group delay and the ± 180 zero-crossing of the phase occur.

Table 7.1: Design parameters six-pole Chebyshev filter

order	6
centre frequency	1200 MHz
passband ripple	0.01 dB
bandwidth	120 MHz

This information can be used to find the first-resonator eigenfrequency of a filter. Shorting all but the first resonator using a tuning screw will effectively remove these resonators by shifting their effect from the frequency range of interest.

Short-circuiting these resonators can be approximated in the coupling-matrix model. The resonance of each cavity is associated with the corresponding diagonal element in the coupling matrix. For resonator n, the diagonal element of the coupling matrix $M(n,n)$ is zero when the

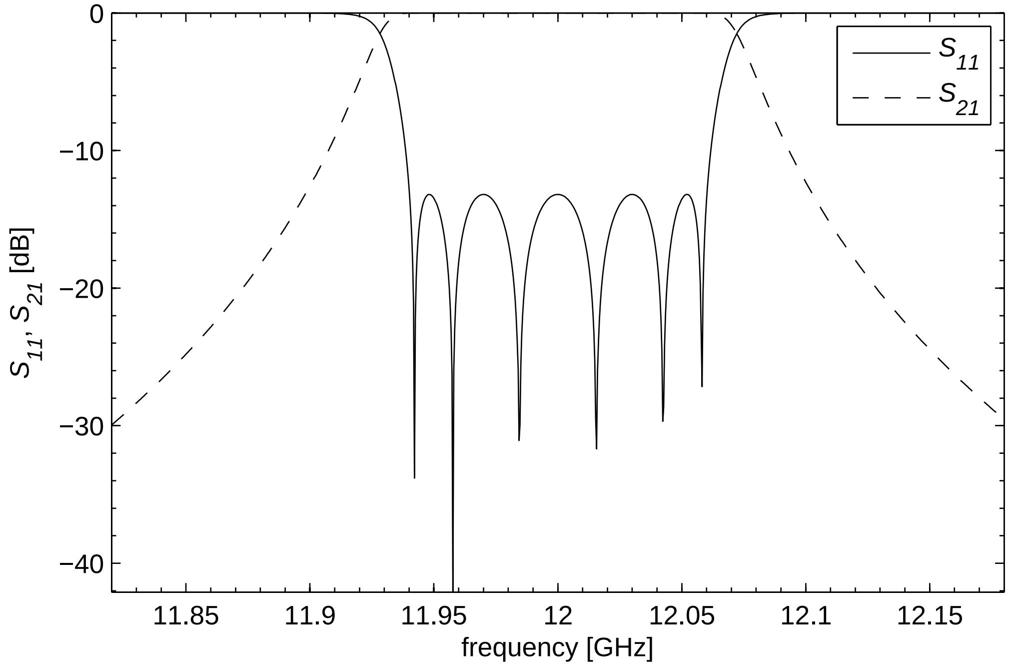

Figure 7.3: Calculated response of a six-pole filter using a coupling-matrix model

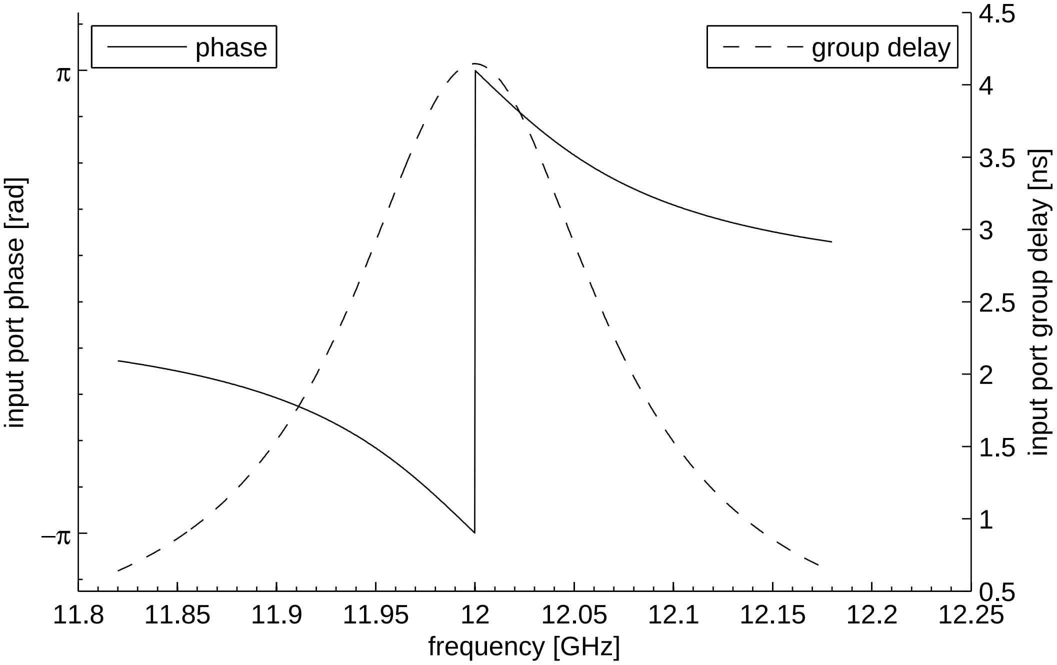

Figure 7.4: Theoretical phase and group delay with all but the first resonator removed

corresponding resonator is tuned. The shorting of a resonator can be approximated by highly detuning that resonator; in the coupling-matrix model this can be accomplished by setting the corresponding diagonal element to some large number, for example $M(n, n) = 100$.

Figure 7.5 shows the group delay and phase for the six-pole filter described above with resonators 2 through 6 shorted in the coupling-matrix model by setting $M(n, n) = 100$ where $n = 2 \cdots 6$. Comparing Figure 7.5 and Figure 7.4, it can be seen that sorting resonators 2 through 6 for a filter correlates well with the expected results. So experimentally, the eigenfrequency of the first resonator can be measured by shorting the subsequent resonators, and measuring the frequency at which the peak group delay or phase zero-crossing occur (12 GHz in this example).

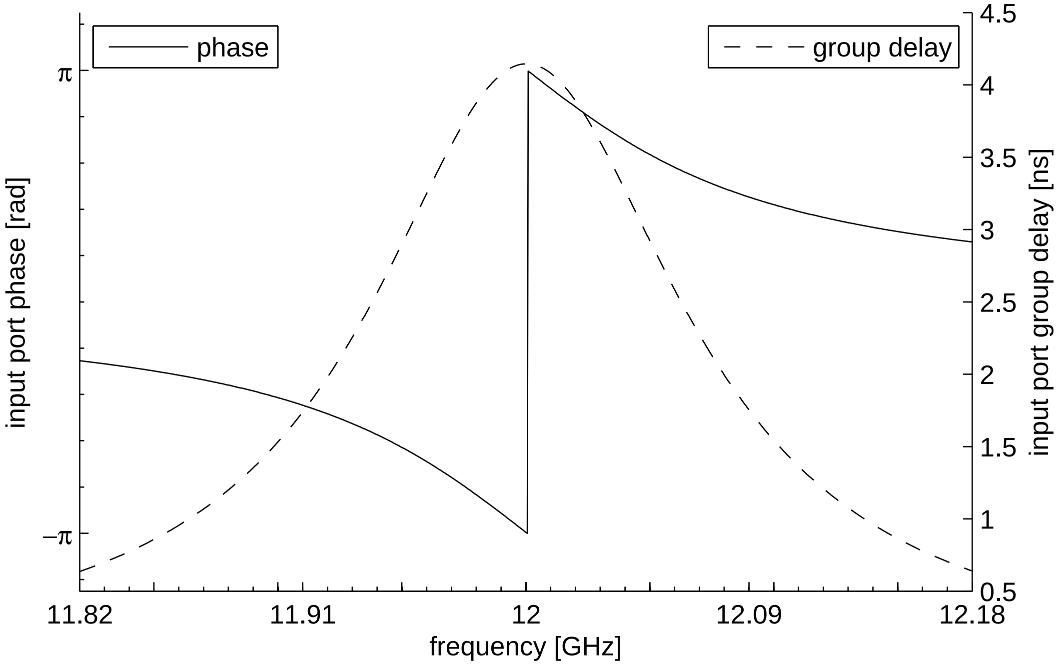

Figure 7.5: Filter with 2nd to 6th resonators shorted

By measuring the resonance at two or more temperatures over the range of interest, the temperature drift of a compensated filter can be measured. The depth of the bimetal compensator for that resonator can be adjusted, and the drift measurement repeated until the drift is zero, or below some acceptable threshold.

A similar metric for the subsequent resonators is required to apply this procedure to each resonator in the filter. Consider the second resonator. If resonators three through six are shorted, the group delay will exhibit two peaks; the lower-frequency peak is associated with the first resonator, and the higher-frequency peak is associated with the second resonator. There is also a phase zero-crossing associated with each of the first two resonances. The group delay and phase calculated using the coupling-matrix model for the six-pole filter with resonators three through six shorted is shown in Figure 7.6.

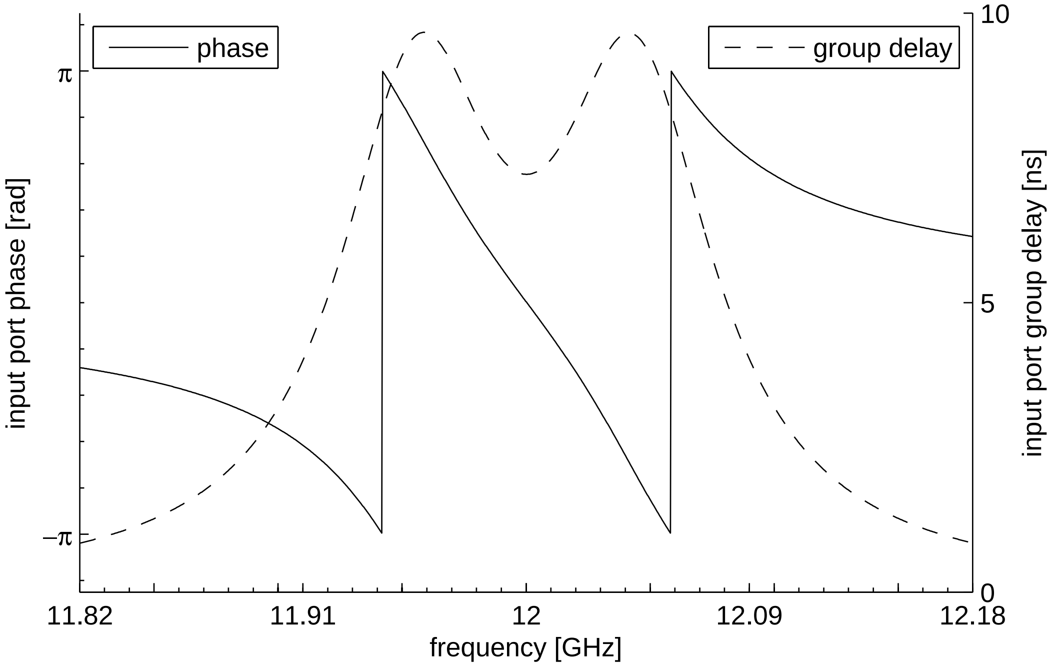

Figure 7.6: Filter with 3rd to 6th resonators shorted

It is undesirable to have any residual drift in the first resonator affecting the measurement of the second resonance. By detuning the first resonator, the peak and phase crossing associated with the first resonance is moved out of the frequency range of interest. The phase zero-crossing is similarly moved to a lower frequency.

As the first resonator is detuned, the group delay peak associated with the second resonance becomes higher and narrower. Similarly, the slope of the phase crossing becomes larger.

This detuning can be simulated by substituting the associated diagonal element of the coupling matrix $M(n,n)$ with a positive non-zero number. Figure 7.7 shows the phase and group delay for the six-pole filter with the third through sixth resonators shorted, and with the first resonator progressively detuned by setting $M(1,1)$ to 0.5, 1, and 5.

The frequency at which the peak of the group delay occurs, or the phase zero-crossing correspond to the resonance of the second cavity. This measurement will approach the resonant frequency as the second resonator is progressively detuned.

Experimentally, if the first resonator is detuned so far that it is effectively shorted, the peak and phase zero-crossing will disappear. In practice, the first resonator must be detuned just far enough that the measurement can be made.

This metric requires that the change in resonance be measured, and accurate measurement of the absolute value of the resonance is not required. From Figure 7.7, it can be seen that the phase-crossing and group delay peak are slightly higher than 12 GHz (the actual resonance). This measurement is still appropriate since it can be used to measure a relative change in resonance.

Again, by cycling the filter temperature and measuring the drift of the second resonator, the associated compensation can be adjusted to achieve acceptable drift.

A similar procedure is used to measure subsequent resonances. When end resonators are shorted, a local group delay peak and a phase zero-crossing is associated with the resonance of each un-shorted resonator, with the highest-frequency peak associated with the last tuned resonator whose resonance will be measured. This is shown for the third resonator of the six-pole filter in Figure 7.8. Be detuning the preceding resonators, a single group delay peak and phase zero-crossing will appear associated with the resonator of interest. This detuning is shown for the third resonator in Figure 7.9. The phase peak again becomes narrower and higher, while the phase zero-crossing also becomes narrower.

Note that resonance can be measured from either filter port. For a six-pole filter for example, resonances 1 through 3 can be measured from port 1, while resonances 4 through 6 are measured from port 2.

Theoretically, either of the phase or group delay signals can be used to measure resonance, and adjust compensation. The phase zero-crossing appears to be a superior metric. The $\pm 180^\circ$ zero-crossing is unambiguous, whereas any flatness in the group delay peak can lead to an imprecise resonance measurement. Furthermore, the group delay is calculated from the phase mea-

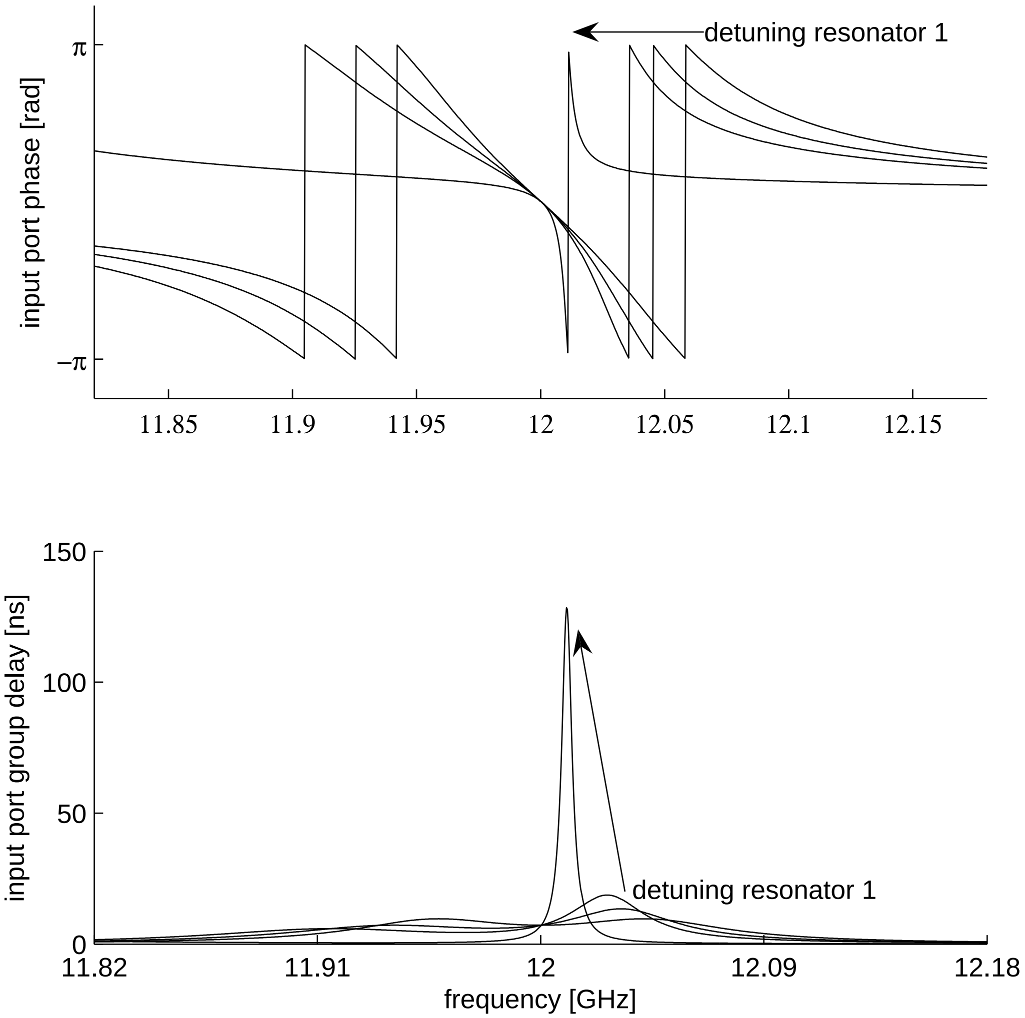

Figure 7.7: Filter with 1st resonator progressively detuned, resonators 3-6 shorted ($M(1,1) = 0.5,\ 1,\ 5$)

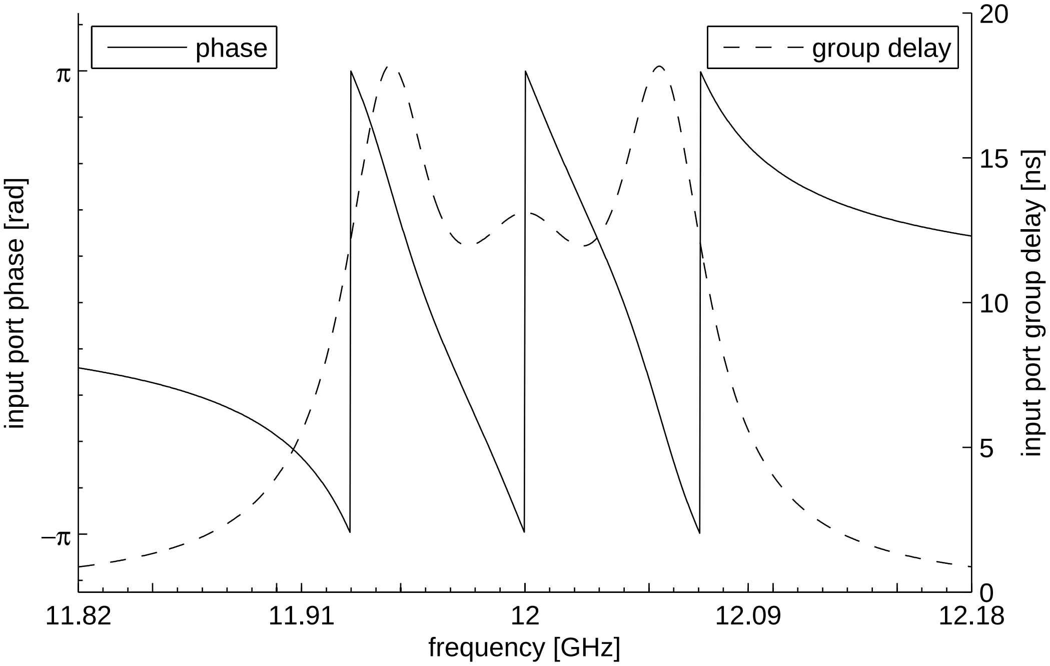

Figure 7.8: Filter with 4rd to 6th resonators shorted

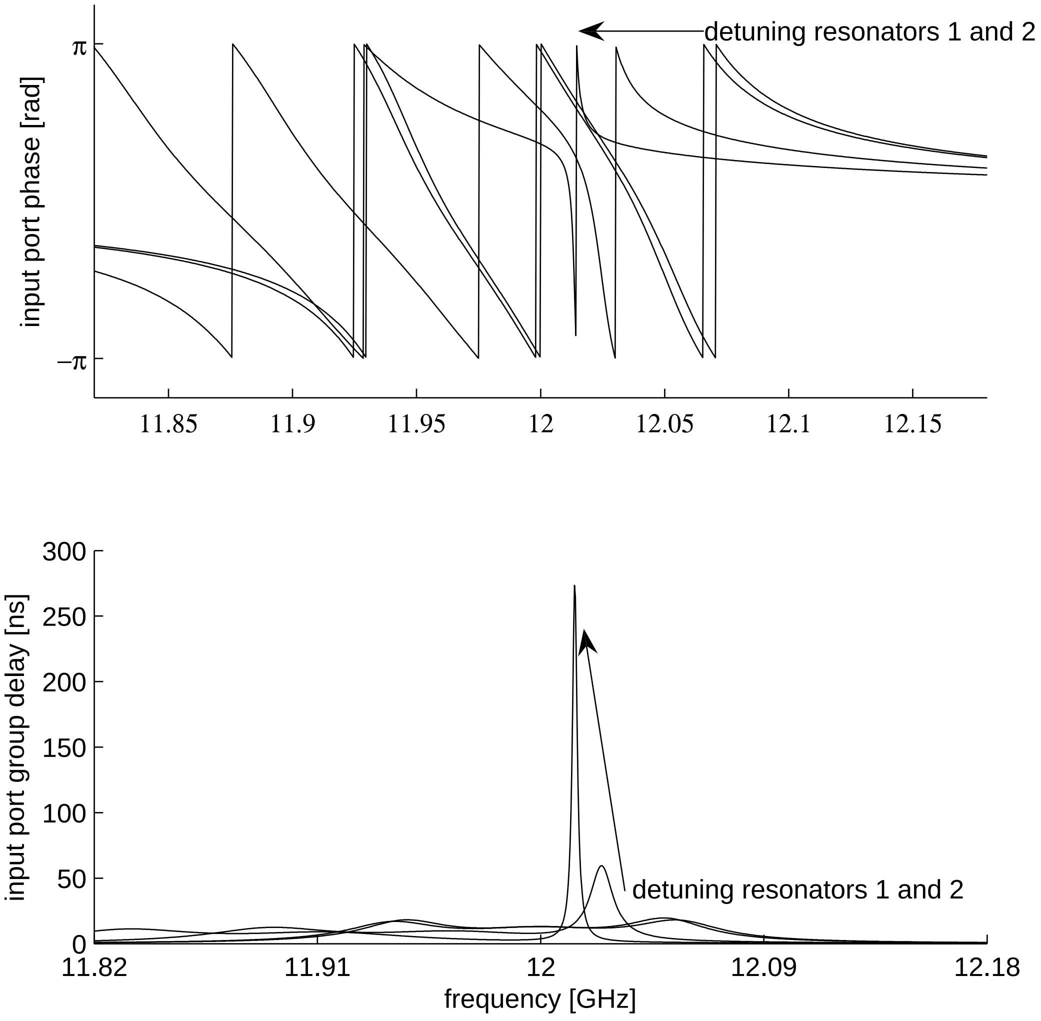

Figure 7.9: Filter with 1st and 2nd resonators progressively detuned, resonators 4-6 shorted ($M(1,1) = M(2,2) = 0.1,\ 1,\ 2$)

surement by the network analyzer. The group delay being a derivative of the phase, the calculated derivative is adversely affected by small amounts of noise in the phase measurement. The group delay signal therefore tends to be extremely noisy in practice.

The accuracy of the phase measurement however is adversely affected by temperature change in the input cables. Typical coaxial input cables exhibit large temperature dependence for phase measurements. The phase signal exhibits a positive shift as temperature increases. This renders the phase measurement unacceptably inaccurate unless specialized phase-stable input cables are used, such as silicone dioxide cables.

The group delay measurement however is not affected by this temperature-induced phase-shift, since it is a derivative of the phase. Therefore, when phase-stable coaxial cables are available, the phase zero-crossing should be used to measure resonance and adjust compensation. Otherwise, the peak group delay must be used.

The procedure for adjusting compensation for an N-pole filter can be summarized as follows:

- Short the second through Nth resonators.
- Measure the peak group delay or phase zero-crossing over a range of temperatures and calculate the drift.
- If the drift is positive, reduce the depth of the bimetal compensator. If the drift is negative, increase the depth. If the drift is positive and the compensator is too close to the cavity wall, the compensator is too long and the length must be trimmed.
- Repeat the drift measurement and compensation adjustment until the measured drift is acceptably low.
- Remove the short from the second resonator, and detune the first resonator until a single narrow group delay peak and phase zero-crossing are observed. If the group delay peak or phase zero-crossing disappear, reduce the detuning of the first resonator until it reappears.
- Measure the peak group delay or phase zero-crossing over a range of temperatures and calculate the drift.

- If the drift is positive, reduce the depth of the second bimetal compensator. If the drift is negative, increase the depth. If the drift is positive and the compensator is too close to the cavity wall, the compensator is too long and the length must be trimmed.

- Repeat the drift measurement and compensation adjustment until the measured drift for the second resonator is below the desired threshold.

- Remove the short from the subsequent resonator, and detune the preceding resonator until a single narrow group delay peak and phase zero-crossing are observed. If the group delay peak or phase zero-crossing disappear, reduce the detuning of the input resonators until it reappears.

- Measure the peak group delay or phase zero-crossing over a range of temperatures and calculate the drift.

- Repeat the drift measurement and compensation adjustment until the measured drift is below the desired threshold.

- Repeat this procedure for subsequent resonators until compensation for half the filter has been tuned.

- Repeat the entire procedure for the other half of the filter using the opposite port.

- Once compensation for each resonator has been tuned, tune the filter and measure the drift of the band edges and centre frequency.

7.3 Compensated Filter Prototype

In order to test bimetal compensation for an aluminum filter, a prototype filter is required. A four-pole WR-62 inductive-iris Chebyshev filter was constructed for this purpose. Scale drawings of the filter are shown in Figure 7.10. Detailed dimensions for the filter are shown in Table 7.2.

The filter is constructed in two halves from 2024 aluminum. Tuning screws for each resonator and iris are inserted into the top of the filter, while bimetal mounting screws are inserted into the bottom wall. Filter dimensions were chosen as a compromise between dimensions appropriate for an uncompensated and compensated implementation.

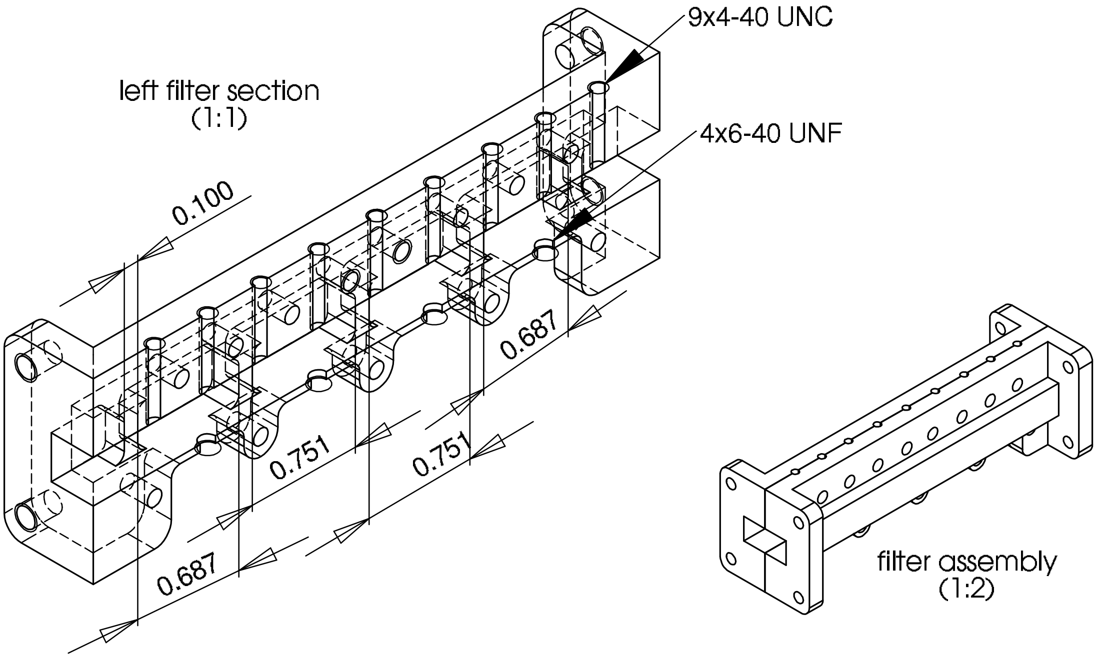

Figure 7.10: Scale drawings of a prototype compensated filter (all dimensions in inches)

Table 7.2: Filter prototype dimensions

order	4
waveguide	WR-62 (0.622 inch width, 0.311 inch height)
resonators 1 and 4	0.687 inches
resonators 2 and 3	0.751 inches
irises 1 and 4	0.346 inches wide, full height
irises 2 and 3	0.224 inches wide, full height

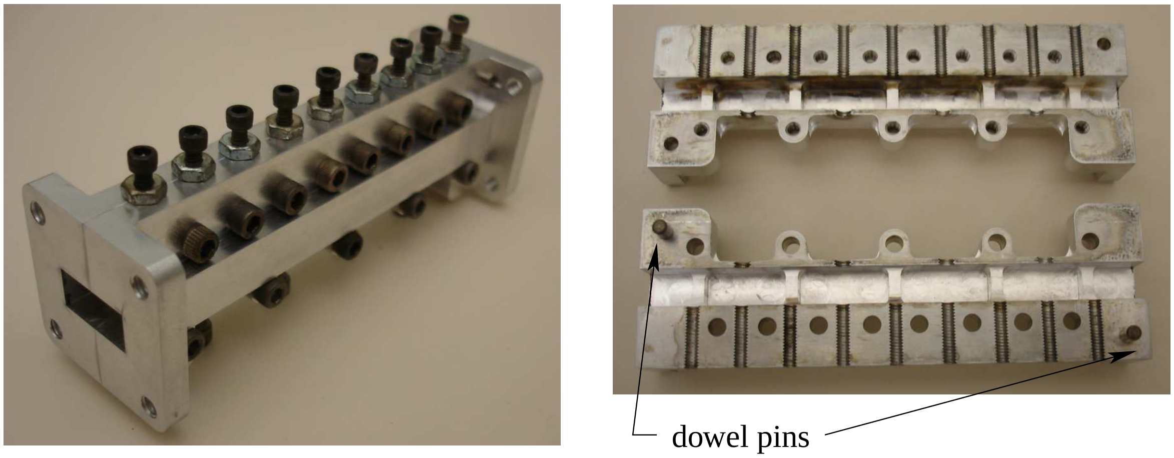

Figure 7.11: Prototype filter, assembled and disassembled

The filter prototype is shown assembled and disassembled in Figure 7.11. Two dowel pins are used to ensure the filter halves are aligned properly when assembled. This is particularly important for the screw threads that span both halves.

The prototype design initially used a larger diameter bimetal mounting screw to allow for easier insertion of the compensator into the cavity. An error in the drawings resulted in a bottom wall that was too thin to accommodate the desired screw size. A finer thread was required to reduce the chance of thread tear-out; a 4-40 UNF screw was used for this purpose.

7.4 Experimental Results

Bimetal filter compensation was implemented in the prototype described in Section 7.3.

The procedure for adjusting compensation described in Section 7.2 was used to adjust compensation for each cavity. The group delay metric was used to measure resonance since phase-stable input cables were not available at the time of testing.

Figure 7.12 shows the response for the compensated filter at ambient temperatures of 20, 50, 80, and $110\ ^\circ\mathrm{C}$. It can be seen that the filter is well-compensated; drift is difficult to distinguish from the full filter response. Figure 7.13 shows the $-15\ \mathrm{dB}$ band edges and centre frequency

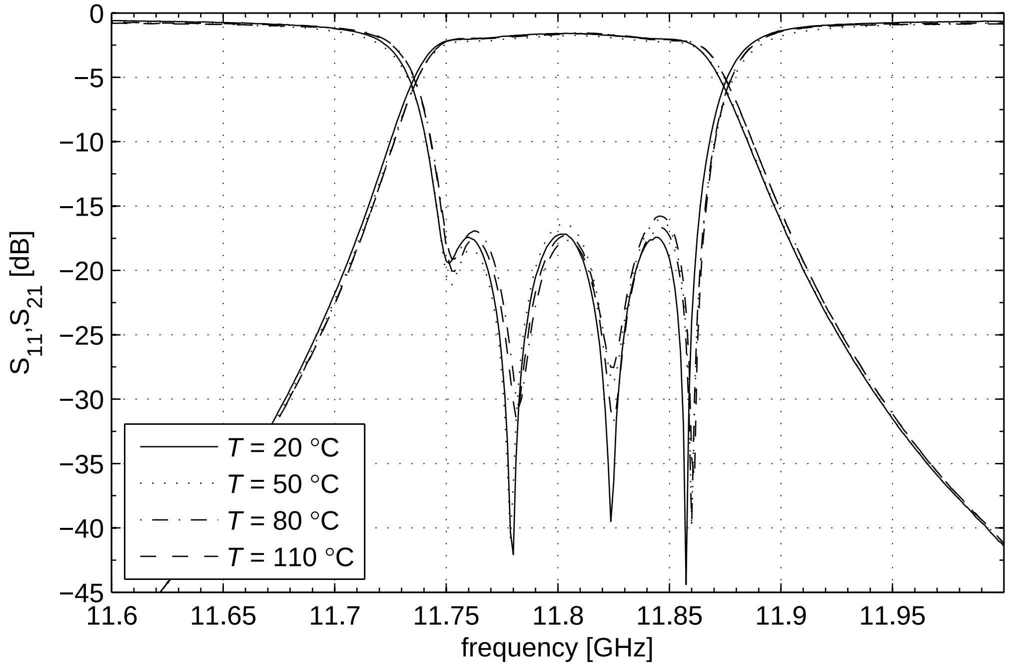

Figure 7.12: Filter response for a 4-pole bimetal-compensated filter

over a range of temperatures. From Figure 7.13 it can be seen that the filter is slightly over-compensated, exhibiting a positive drift of approximately 2.35 ppm$/^\circ\mathrm{C}$.

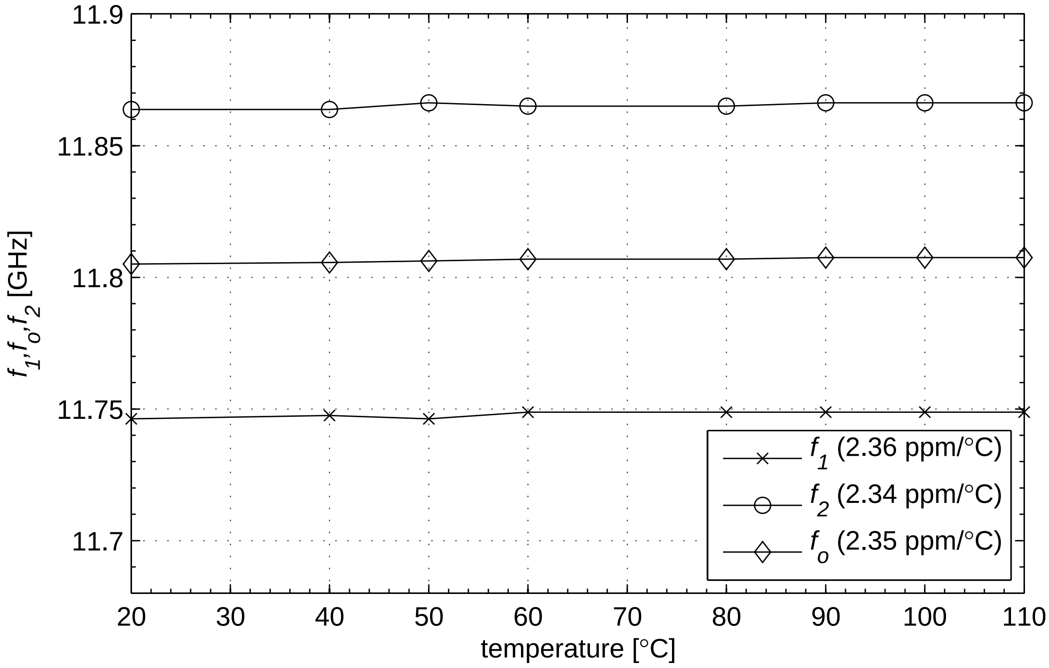

Figure 7.13: Band edges and centre frequency for a 4-pole bimetal-compensated filter

The peak group delay metric was used to measure resonance in each cavity and adjust compensation. The phase zero-crossing metric is more precise, however this metric can only be used when temperature-stable phase measurement is possible. Phase drift introduced by heating of the input cables renders the phase zero-crossing metric unacceptably inaccurate. The less precise peak group delay metric is likely the cause of the positive measured temperature drift of the filter.

A temperature drift of -0.382 ppm$/^\circ\mathrm{C}$ was achieved for a single compensated cavity (c.f. Chapter 6). Given a more precise measurement of the resonance of each cavity in the filter, it is expected that the drift of the compensated filter will approach this value.

From Figure 7.13 it can be seen that the lower and upper band-edges drift at 2.34 and 2.36 ppm$/^\circ\mathrm{C}$ respectively, while the centre frequency drifts at 2.35 ppm$/^\circ\mathrm{C}$. The difference between the drift of the band edges is 0.02 ppm$/°\mathrm{C}$. The fact that the band-edges drift at nearly the same rate, along with the fact that the return loss in the pass-band is quite constant show that the filter exhibits minimal detuning with temperature change.

Chapter 8

Multiphysics Modelling of Power Handling for Bimetal Compensated Filters

Thermal effects on RF devices involve complex coupling between thermal, mechanical, and electro-magnetic phenomena. A multiphysics approach is proposed which consists of interdependent mechanical, electrical, and thermal simulations. This approach uses the arbitrary Lagrangian-Eulerian (ALE) method to model the geometric interdependence. Models are provided to simulate temperature drift under uniform temperature conditions, distributed temperature profiles due to resistive microwave heating under high power, and finally, temperature drift given arbitrary thermal boundary conditions for compensated components under high-power.

These simulations are used to examine the power handling capability of bimetal compensated filters. The effect of input power on a cantilever bimetal compensator is simulated. The results of this simulation imply that a shorter compensator helps to improve power handling capability. Power handling is evaluated using a two-sided bimetal compensator with both one and two compensators.

8.1 Multiphysics Modelling

Parameterized modelling of thermal expansion and bimetal actuation requires a number of assumptions; for example uniform temperature distribution, unconstrained expansion, and constant bimetal curvature radius (c.f. Section 4.3). In applications where these assumptions are unacceptable, a more complex modelling approach is required. In the general case, thermo-mechanical simulation is required to model the dimensional changes that provide compensation.

As more complex approaches to temperature compensation are explored, a set of simulation tools are required that can account for complex thermal conditions including resistive heating and associated dimensional change. Furthermore, a full-wave electro-magnetic simulation must be solved on the deformed geometry to determine compensated response.

The geometric interdependence is problematic, particularly in cases where there is significant deformation. The arbitrary Lagrangian-Eulerian method can be used to model a moving interface between two simulations [68]. The arbitrary Lagrangian-Eulerian method was developed to model fluid-structure interactions. This method is used here to model interaction between an electromagnetic field and a structure. This can account for interdependence between thermo-mechanical deformation and RF simulations. Simulations which account for multiple coupled phenomena (such as electrical and mechanical) are often referred to as multiphysics simulations [69].

In this work, these simulations are implemented in the COMSOL Multiphysics software package (previously known as FEMLAB) which can solve structural, full-wave RF, thermal, and arbitrary Lagrangian-Eulerian simulations [57]. Each simulation module can be solved separately or simultaneously, and can be coupled arbitrarily.

8.1.1 Uniform Temperature Mechanical-RF Simulation

Many approaches to temperature compensation exploit thermally-induced dimensional change to reduce temperature drift by combining materials with different thermal expansion coefficients [28, 35]. By assuming uniform temperature change, a baseline temperature drift can be established. In order to model these devices in the general case, a combined mechanical-electrical simulation is required.

This multiphysics simulation is constructed as follows. A component's dimensions are given at some nominal temperature. Change from that temperature ΔT will cause thermally-induced stress and strain. The relevant output from the mechanical simulation is the dimensional change (u, v, w) at each point in the geometry. Although ΔT can be specified arbitrarily at each point, consider first the case of uniform temperature change.

The electro-magnetic problem must be solved on the deformed geometry. The arbitrary Lagrangian-Eulerian method is used to calculate a deformed mesh corresponding to the output of the mechanical simulation [57].

Finally, a full-wave RF simulation is performed on the deformed mesh. A schematic of the uniform-temperature RF simulation is shown in Figure 8.1.

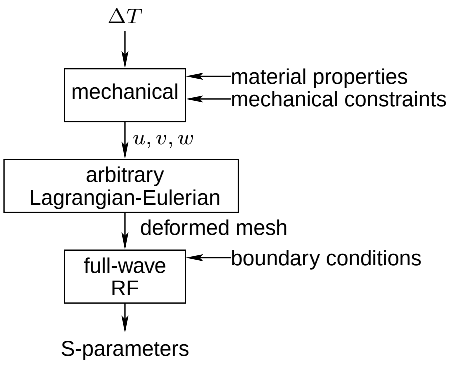

Figure 8.1: Multiphysics uniform-temperature mechanical-RF simulation routine

8.1.2 Resistive Heating Simulation

In high-power applications, resistive heating is a significant thermal factor. A multiphysics approach is required to model this phenomenon since the resistive heat flux must be extracted from the RF solution.

Given input power P_{in}, an RF simulation is used to calculate the time-average resistive heat flux distribution Q_{sav} at the interior boundaries.

The resistive heat flux from the RF simulation is input to the thermal simulation. Given the thermal boundary conditions, the thermal simulation produces the temperature distribution. A schematic of this multiphysics simulation is shown in Figure 8.2.

8.1.3 Resistively heated Thermal-Mechanical-RF Simulation

In order to quantify the performance of a thermally-compensated component undergoing resistive heating, the interaction between the RF domain and the thermo-mechanical domain must

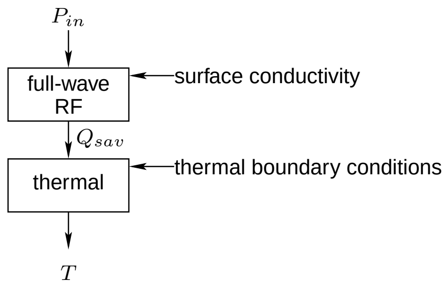

Figure 8.2: Multiphysics resistive heating simulation routine

be considered. The interdependence of the RF, thermal and structural modules complicates the solution procedure. COMSOL Multiphysics is capable of solving modules simultaneously, however the resulting solution matrix for the simulation proposed below has a degree of freedom so large that it cannot be solved on a desktop computer. An iterated solution must be used to handle the interdependence.

Consider a component with input power P_{in}. An initial RF solution is required to find the nominal resistive heat flux Q_{sav}.

The thermal simulation must then be solved using the calculated heat flux. The output of the thermal simulation is the temperature distribution, which is input to the mechanical simulation. The arbitrary Lagrangian-Eulerian method uses the dimensional change from the mechanical simulation to calculate the deformed mesh.

The RF simulation is solved on the deformed mesh, and the resulting S-parameters can then be compared to the previous RF solution. If the S-parameters have converged, the simulation is finished. Otherwise, the simulation starts again with the thermal simulation, using the surface resistive heating from the most recent RF solution. A schematic of this simulation is shown in Figure 8.3.

How fast this simulation converges depends on how much coupling there is between the thermal and RF simulation. By definition, a well compensated device will exhibit low coupling between the thermal and RF simulations, and will converge quickly. In practice, these simulations converge in no more than three passes.

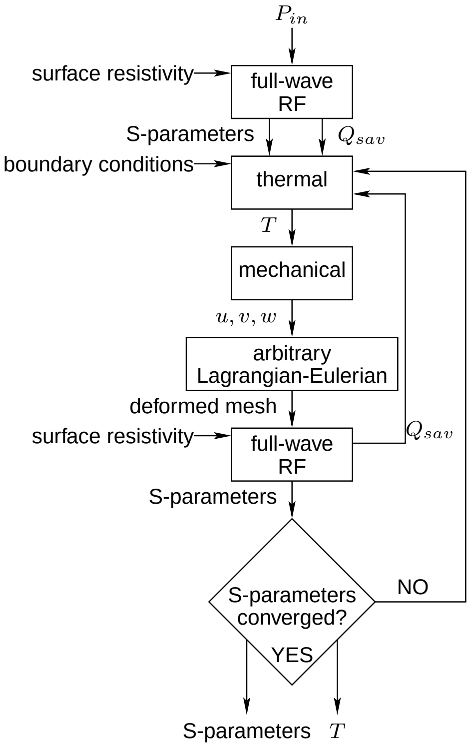

Figure 8.3: Multiphysics resistively heated mechanical-RF simulation routine

8.2 Power-handling and Bimetal Compensation

In order to design bimetal-compensated filters for high-power applications, a number of factors must be accounted for. Firstly, the nominal compensated performance of a design must be evaluated. The nominal performance is best described by the compensated drift under uniform temperature change, which corresponds to the results of the uniform-temperature simulation (c.f. Figure 8.1.)

The field will be highly concentrated around the compensator, resulting in more resistive heating at the bimetal. It is therefore useful to quantify the local heating at the bimetal under typical thermal conditions and input power. This can be calculated using the resistive heating simulation (c.f. Figure 8.2).

Finally the effect of local heating on compensated performance must be determined for a given design, which can be determined using the resistively heated mechanical-RF simulation (c.f. Figure 8.3). The multiphysics simulations applied as described will provide a full accounting of compensated performance. This information can be used to identify problem areas, and refine the design for improved performance, as is demonstrated in this chapter.

8.2.1 Boundary Conditions

Boundary conditions for the mechanical simulation require only sufficient point constraints to eliminate rotation. Material properties for the mechanical simulation in each case are for 3003-H18 aluminum for the filter and screws, and corresponding material properties for each layer of the Truflex P675R bimetal manufactured by Engineering Materials Solutions. The subdomain temperature is provided either by a constant temperature change ΔT or an absolute temperature T given by the thermal simulation. Nominal dimensions are given at $20\ ^{\circ}\mathrm{C}$.

For the RF simulation, the input and output ports are set to TE_{10} mode, and the input power P_{in} is specified. To model the silver plating of the filter, all other boundaries are set to the impedance of silver.

Thermal boundary conditions are meant to model a filter mounted on a large heat-sink aboard a satellite in orbit. Assuming the heat sink is infinitely large, the lower external boundary of the filter is set to a constant temperature T_{ext}. Such a filter would be radiating to other equipment with an average temperature the same as the heat sink, T_{ext}. All other exterior thermal boundaries are therefore set to radiate to T_{ext} with an assumed emissivity of 0.8.

8.2.2 Cantilevered Bimetal Compensator

Consider the bimetal-compensated filter shown in Figure 8.4 which uses a cantilever-configured bimetal compensator. A bimetal length of $l_b = 3.72\ \mathrm{mm}$ is chosen for all resonators based on eigenmode simulations of a single resonator.

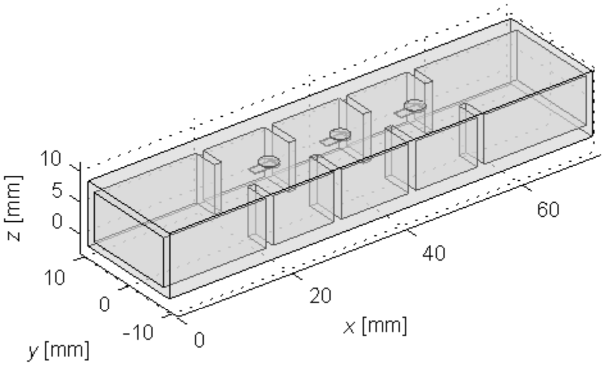

Figure 8.4: Cantilevered bimetal-compensated 3-pole filter geometry

The results of a uniform-temperature simulation shown in Figure 8.5 show a compensated centre-frequency drift of -1.14 ppm/°C. The lower and upper band edges f_1 and f_2 denote the $-20\mathrm{dB}$ bandwidth. The compensated drift can be further reduced by adjusting compensation for each cavity as described in Section 7.2, however further refinement will not affect the power handling.

The compensated response under high input-power will be affected by local resistive heating in the filter. Since the field is concentrated at the bimetal tip, the resistive heating will be highest there. The resistive heating simulation confirms this to be the case. Figure 8.6 shows the bimetal tip temperature in each cavity with respect to frequency, for an input power of $100\ \mathrm{W}$ and $T_{ext} =$

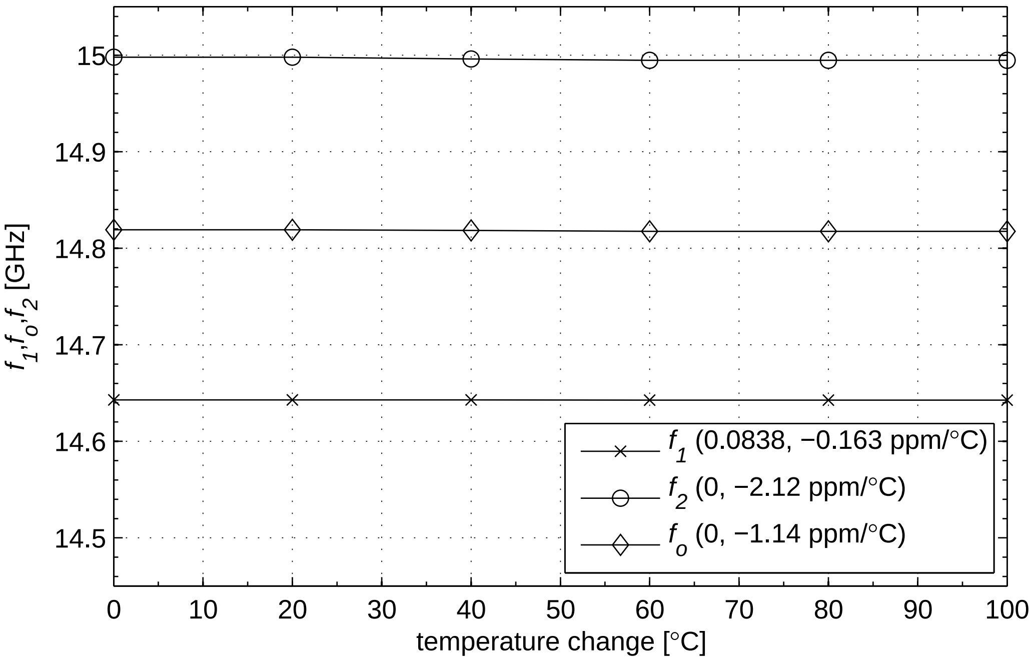

Figure 8.5: Simulated drift of $-20\,\mathrm{dB}$ band edges and centre frequency for a cantilevered bimetal-compensated aluminum filter under uniform temperature

$85\ ^\circ\mathrm{C}$ (where T_{ext} is both the sink and ambient temperature). It can be seen that the bimetal tip temperature is as high as $197\ ^\circ\mathrm{C}$ for the second resonator at the band edges. The maximum temperature change at the bimetals from ambient temperature is $112\ ^\circ\mathrm{C}$. As predicted in the lumped element heating model from [70], resistive heating is highest for the second resonator at the band edges.

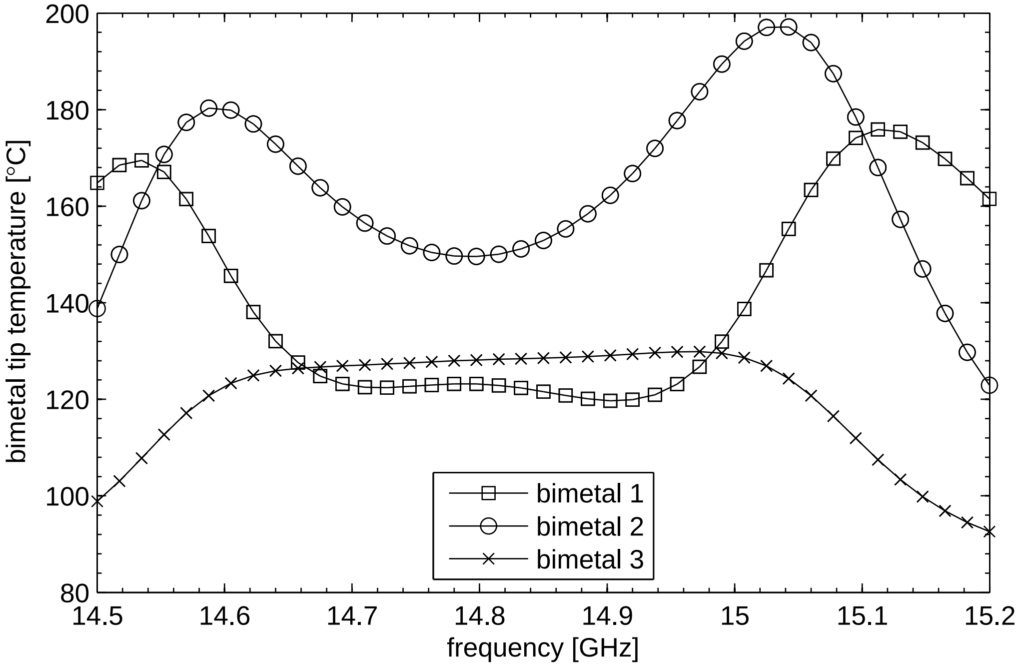

Figure 8.6: Simulated cantilevered bimetal heating compared to resonator temperature

Consider the maximum bimetal tip temperature that occurs at 15.04 GHz in the second resonator. The temperature change along the bimetal edge can be determined from the RF heating simulation since a full temperature distribution is calculated. Figure 8.7 shows the temperature change for the cantilevered bimetal along the bimetal edge in the second resonator. It can be seen that the maximum temperature of $197\ ^\circ\mathrm{C}$ drops nearly as low as the external temperature $85\ ^\circ\mathrm{C}$ along the length of the bimetal, due to heat conduction along the bimetal to the filter body. The bimetal tip temperature is maximum as expected, however the average bimetal temperature is substantially lower than the tip temperature. The bimetal tip temperature is however a useful metric to quantify bimetal heating.

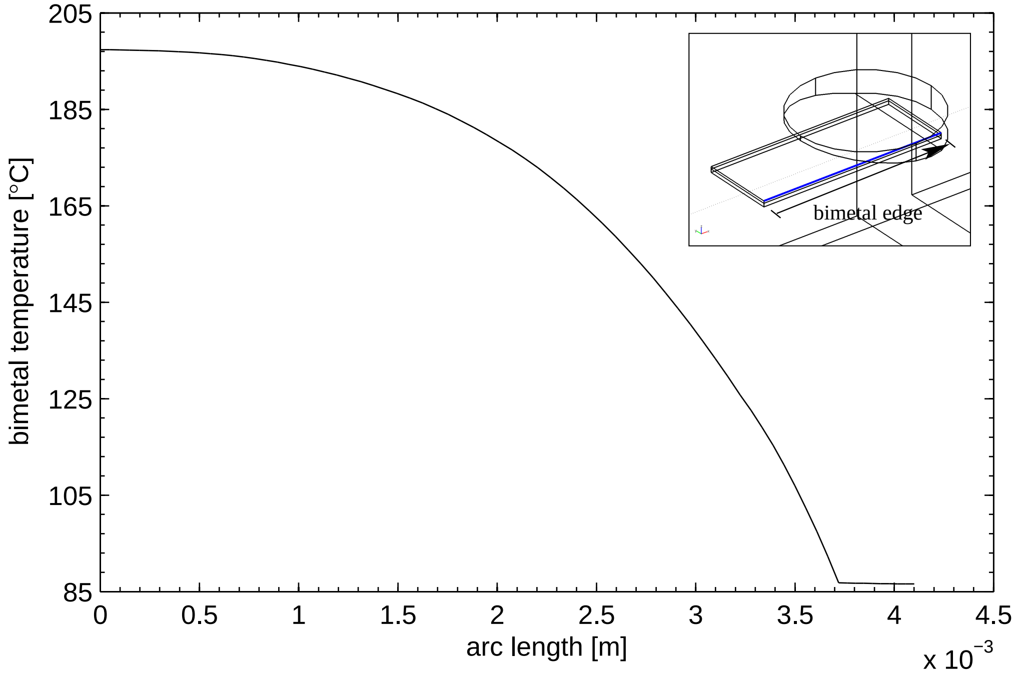

Figure 8.7: Simulated heating along cantilevered bimetal edge

A thermal-mechanical-RF simulation can be used to determine the effect of local resistive heating on compensated response. The filter parameter drift with respect to T_{ext} at 100 W of input power is shown in Figure 8.8, along with the nominal filter parameters ($Pin = 1$ W and $T = 20\ ^{\circ}\mathrm{C}$). It can be seen that the filter response is shifted upward in frequency as the local heating of the bimetal compensator leads to over compensation. The centre frequency drift at 100 W of power is -6.16 ppm$/^{\circ}\mathrm{C}$.

The largest change in centre frequency between the nominal value and the centre frequency at 100 W is 1357 ppm. In comparison, an uncompensated aluminum filter undergoing $100\ ^{\circ}\mathrm{C}$ temperature change would experience a -2300 ppm change in centre frequency, or between -160 ppm and -200 ppm for an uncompensated Invar filter (depending on the coefficient of thermal expansion of the Invar alloy).

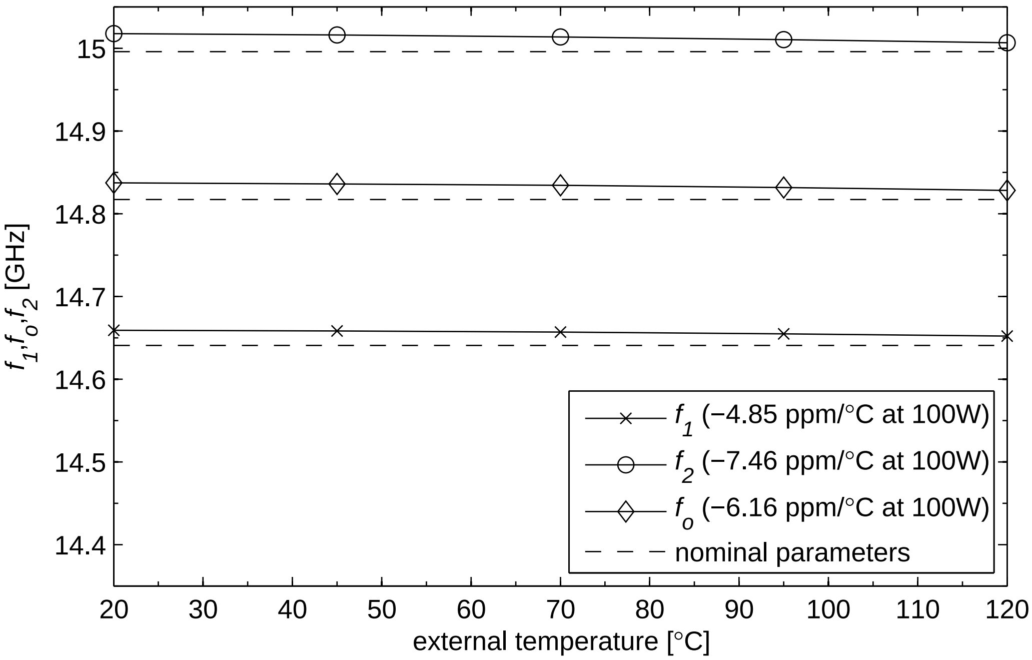

Figure 8.8: Simulated effect of resistive heating on a cantilever-bimetal compensated filter at $Pin = 100$ W, and nominal filter parameters ($Pin = 1$ W and $T = 20$ °C)

The filter responses at maximum and minimum input powers and external temperatures are shown in Figure 8.9. It can be seen that with the bimetal tip heated to nearly $200\ ^\circ\mathrm{C}$, the filter is only nominally detuned. The change in filter response comes largely as a frequency shift.

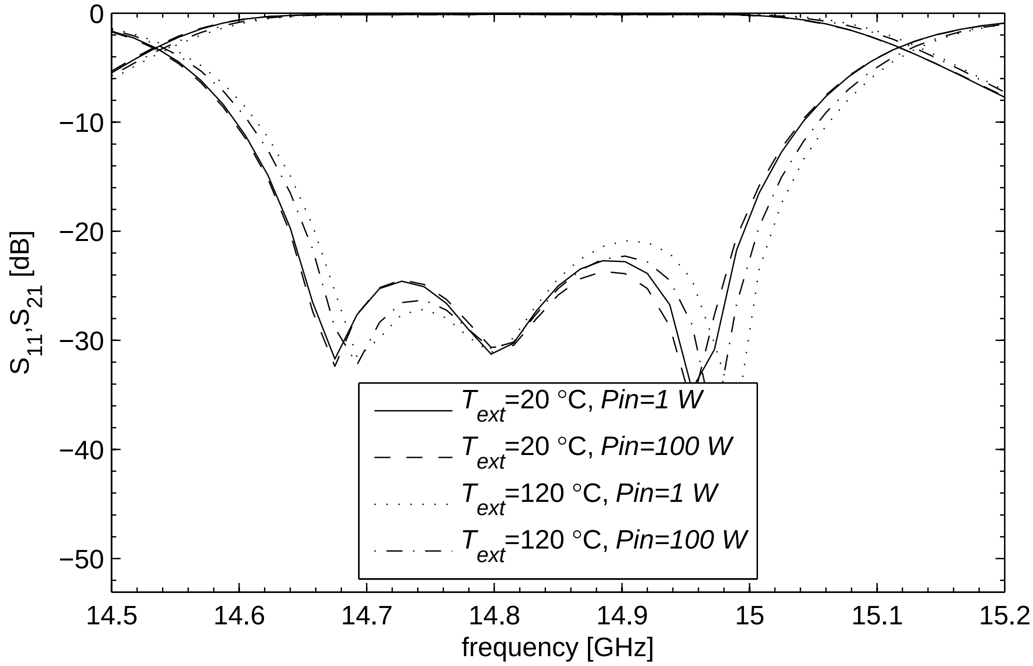

Figure 8.9: Simulated filter response for the cantilevered-bimetal-compensated filter

8.2.3 Double-Sided Bimetal Compensator

In order to reduce the effect of local resistive heating on the compensated filter, a compensator must be designed with a shorter effective length to allow for more effective heat sinking to the filter body. Consider a double-sided bimetal compensator as shown in Figure 8.10.

A bimetal length of $l_b = 3.0\ \mathrm{mm}$ is chosen using eigenmode simulations for a single compensated cavity. Figure 8.11 shows the compensated filter drift under uniform temperature change. This design shows a centre frequency drift of -6.57 ppm$/^\circ\mathrm{C}$. Although this filter is under-compensated it is suitable for evaluating susceptibility to resistive heating.

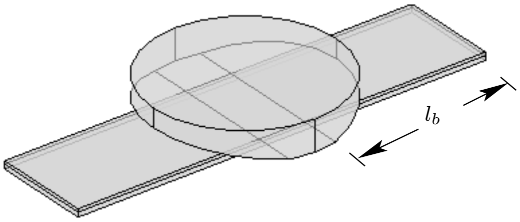

Figure 8.10: Double-sided bimetal compensator

Figure 8.12 shows the temperature at each bimetal tip over the frequency range. Again, maximum heating occurs for the second resonator at the band edges. The maximum heating for the $3\ \mathrm{mm}$ double-sided bimetal is $36\ ^{\circ}\mathrm{C}$ from $T_{ext} = 85\ ^{\circ}\mathrm{C}$, compared to $112\ ^{\circ}\mathrm{C}$ for the $3.72\ \mathrm{mm}$ cantilevered bimetal compensator.

Figure 8.13 shows the filter parameter drift at $100\ \mathrm{W}$ of input power, along with the nominal parameters (i.e. the filter parameters at $1\ \mathrm{W}$ of input power and $T = 20\ ^{\circ}\mathrm{C}$). At a constant input power of $100\ \mathrm{W}$, the compensated drift is degraded to -7.34 ppm/$^{\circ}\mathrm{C}$ from -6.57 ppm/$^{\circ}\mathrm{C}$. The drift calculated from the nominal parameters , is positive 3.91ppm/$^{\circ}\mathrm{C}$ and negative 3.42ppm/$^{\circ}\mathrm{C}$. Note that this drift is lower because the nominal parameters bisect the temperature response at $100\ \mathrm{W}$

The largest deviation from the nominal centre frequency up to $100\ \mathrm{W}$ of input power and $100\ ^{\circ}\mathrm{C}$ of temperature change is -654 ppm, compared to 1357 ppm for the cantilevered compensator. This confirms the possible improvement when the effects of local heating can be mitigated by reducing the effective length of the bimetal. However, further reduction in the effective length is required.

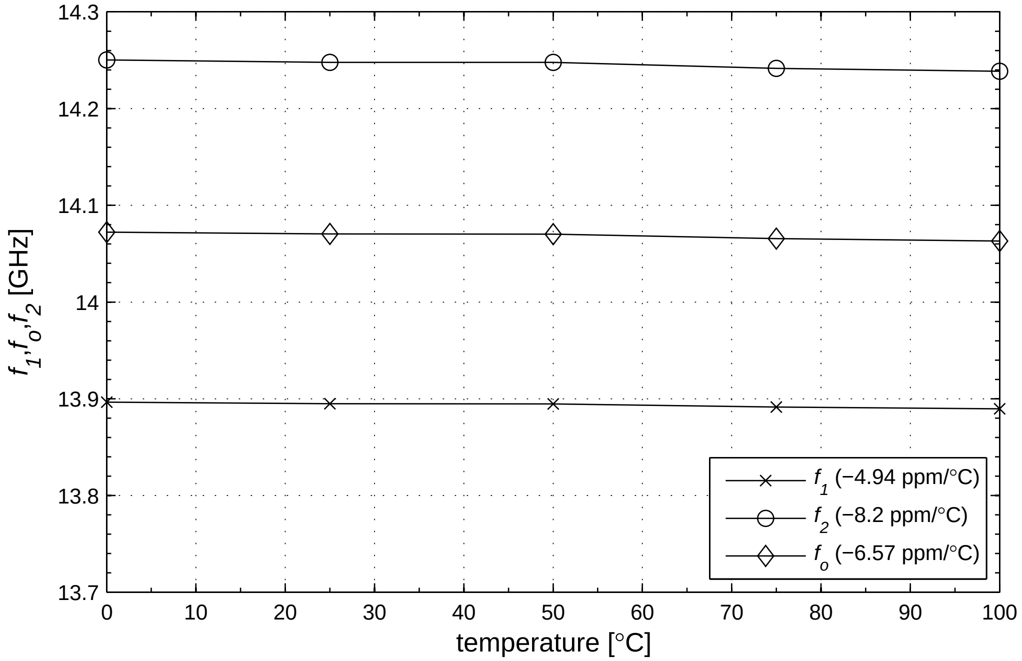

Figure 8.11: Simulated drift for a double-sided-bimetal compensated aluminum filter under uniform temperature

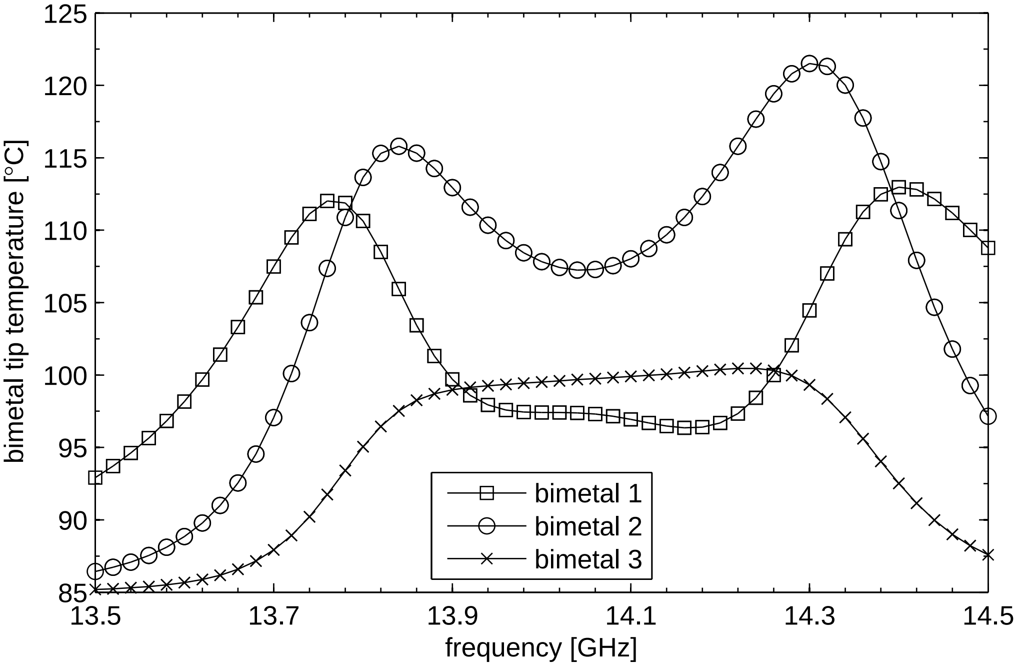

Figure 8.12: Simulated resistive heating for a double-sided bimetal-compensated filter

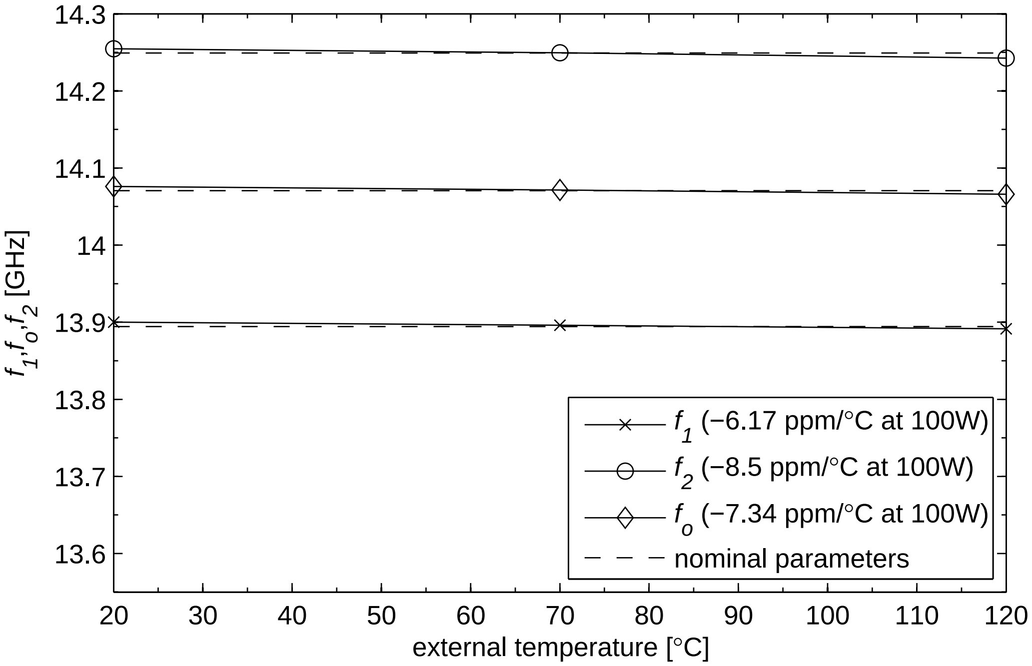

Figure 8.13: Simulated effect of resistive heating on a double-sided-bimetal compensated filter at $Pin = 100$ W, and nominal filter parameters ($Pin = 1$ W and $T = 20$ °C)

8.2.4 Two-Screw Double-Sided Bimetal Compensator

Although the double-sided compensator is less susceptible to resistive heating, the bimetal length must be further reduced to produce drift comparable to Invar filters. By using two double-sided compensators on the opposite broad-walls in each cavity of the waveguide filter, a shorter bimetal length can be used. Rather than using eigenmode simulations to choose the bimetal length, here an iris-loaded compensated cavity is simulated, using the peak group delay to measure resonance. This results in an approximate bimetal length of $2.8\ \mathrm{mm}$ for compensation.

Figure 8.14 shows the result of a uniform-temperature-change simulation. The centre frequency drift of $+1.02$ ppm/$^\circ\mathrm{C}$ shows the filter is slightly over-compensated.

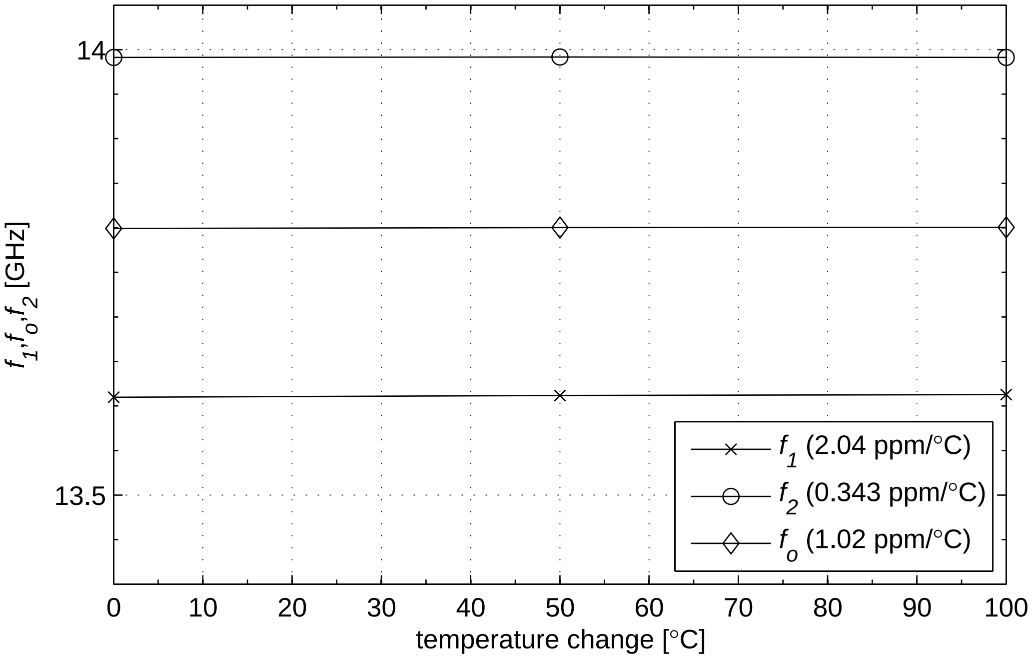

Figure 8.14: Simulated drift for a double-sided-bimetal two-compensator aluminum filter under uniform temperature

From Figure 8.15, it can be seen that this configuration results in substantially reduced local heating. Bimetal tip temperature is increased by $26\ ^\circ\mathrm{C}$ from $85\ ^\circ\mathrm{C}$ ambient temperature, with maximum heating again occurring in the second resonator at the band edge.

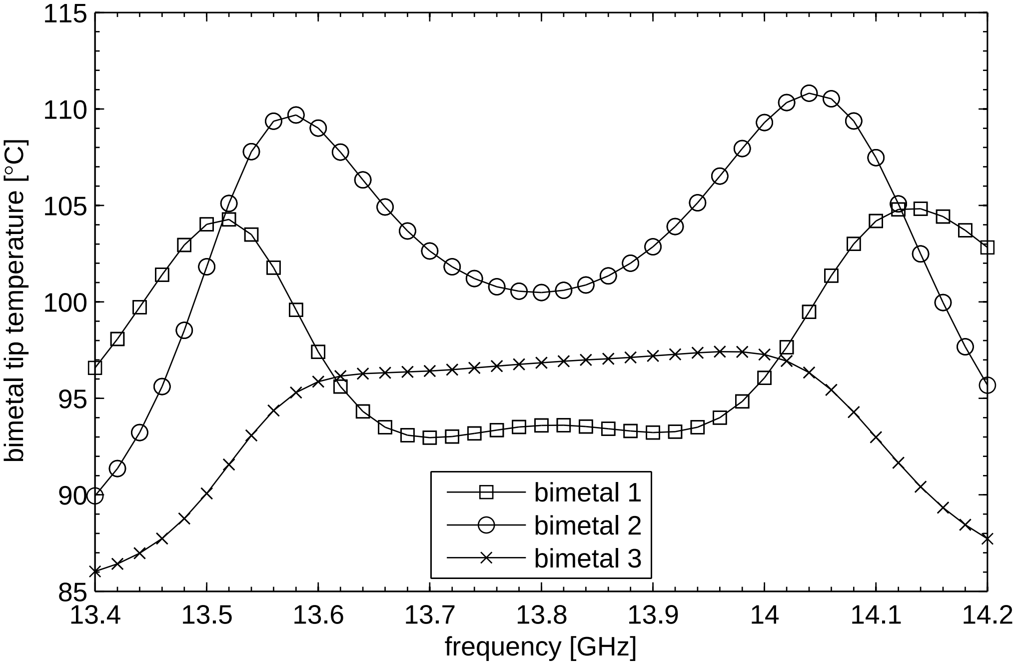

Figure 8.15: Simulated resistive heating for a double-sided-bimetal two-compensator filter

The effect of the resistive heating on compensation at 100 W of input power is shown in Fig. 8.16 along with the nominal filter parameters. It can be seen that centre frequency drift at 100 W is reduced to 0.7 ppm$/^\circ$C from 1.02 ppm$/^\circ$C. The largest change from the nominal filter parameters is $+277$ ppm for input power ranging from $0 - 100$ W, and a temperature change of 100 $^\circ$C. An uncompensated aluminum filter would exhibit -2300 ppm of drift over a 100 $^\circ$C temperature change, and an Invar filter would show between -160 ppm and -200 ppm depending on the alloy. Note that the overcompensation of the filter results in a larger overall drift. If the filter were slightly under-compensated, the positive frequency shift caused by resistive heating in the bimetal would be offset by the negative drift.

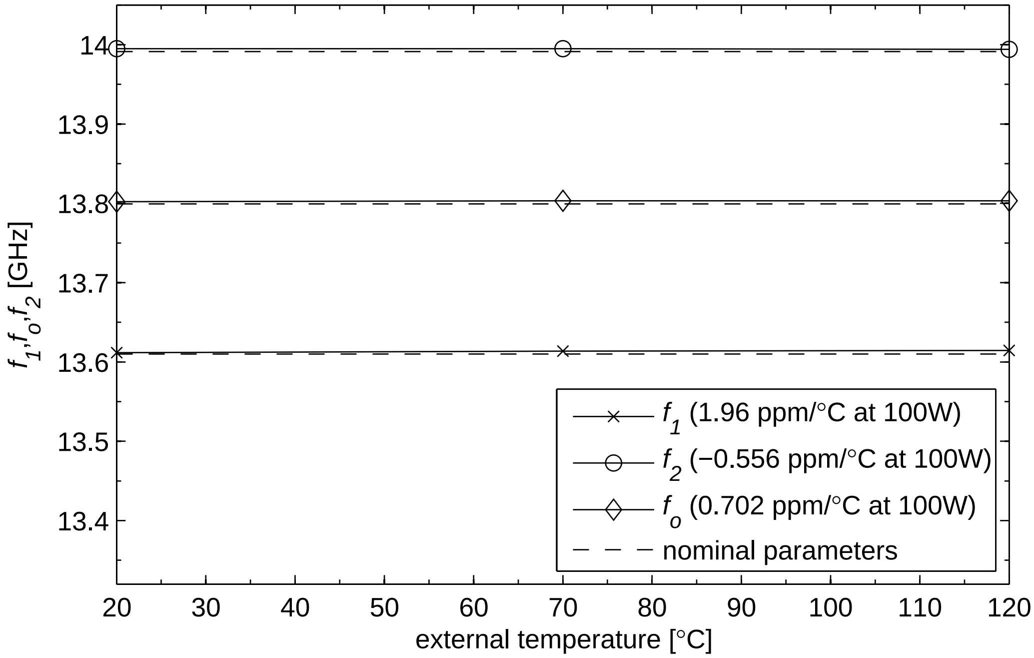

Figure 8.16: Simulated effect of resistive heating on a double-sided-bimetal two-compensator filter at $Pin = 100$ W, and nominal filter parameters ($Pin = 1$ W and $T = 20$ $^\circ$C)

Table 8.1 provides a summary of the power handling results for each bimetal compensator.

Table 8.1: Comparing temperature drift results

	drift, low power	drift, $P_{in} = 100$ W	max. Δf_o $\Delta T = 0 \ldots 100$ °C $P_{in} = 0 \ldots 100$ W
uncompensated aluminum	-23 ppm/°C	-	-2300 ppm
uncompensated Invar	-1.6 ppm/°C	-	-160 ppm
cantilevered bimetal 3.72 mm	-1.14 ppm/°C	-6.16 ppm/°C	1357 ppm
double-sided bimetal 3 mm	-6.57 ppm/°C	-7.34 ppm/°C	-654 ppm
2x double-sided bimetal 2.8 mm	$+1.02$ ppm/°C	$+0.7$ ppm/°C	277 ppm

Chapter 9

Conclusions and Recommendations

Temperature compensation continues to be a design issue in many RF applications. Effective temperature compensation can allow for the use of lighter, less expensive materials such as aluminum in lieu of more costly, heavier materials like Invar.

This thesis proposes that a bimetal tuning screw can be used to compensate for temperature drift in aluminum resonators and filters. The bimetal tuning screw consists of a bimetal actuator mounted on a screw inserted into the side wall of a filter or resonator. By orienting the bimetal element such that it actuates towards the wall with increasing temperature, a tuning screw with a variable effective length is formed whose actuation will compensate for the expansion of the aluminum structure.

Two configurations are proposed for the bimetal tuning screw; one with a cantilevered bimetal strip, and another with a double-sided bimetal compensator. The cantilevered configuration consists of a bimetallic strip attached to the mounting screw at the end of the bimetal. The double-sided compensator is attached to the mounting screw at the centre of the strip length, effectively producing two compensators.

This design for a compensator exhibits several favourable properties. It is a general approach that can be applied to existing filter designs. Mechanical eigenmode simulations demonstrate that the stiffness of the bimetal material is sufficient to limit any potential vibration.

Since the field is stronger near the centre of a resonator, the amount of compensation can be adjusted by rotating the mounting screw, which changes the depth of the tuning screw. It is demonstrated in simulation that any effect of rotation on resonant frequency is overwhelmed by the effect of the depth change. This conclusion was later borne out when implementing filter and resonator compensation. Since compensation is adjustable, any effects of manufacturing tolerances on compensation can be accounted for.

It is demonstrated experimentally that a bimetal tuning screw can be used to produced compensated resonators and filters. A cantilevered compensator is used to produce a compensated aluminum resonator exhibiting -0.38 ppm/$^\circ\mathrm{C}$ of temperature drift from $20\ ^\circ\mathrm{C}$ to $100\ ^\circ\mathrm{C}$. This is less than the temperature drift exhibited by an Ivar resonator (approximately -1.6 ppm/$^\circ\mathrm{C}$). An uncompensated aluminum cavity will exhibit -23 ppm/$^\circ\mathrm{C}$ of temperature drift.

A temperature compensated aluminum filter is also demonstrated experimentally. This filter, also using a cantilevered bimetal tuning screw, exhibits temperature drift of 2.35 ppm/$^\circ\mathrm{C}$. The positive temperature drift shows that the filter is slightly over compensated. The compensation adjustment for this filter was performed using the group-delay metric since phase-stable input cables were not available. By adjusting compensation using the more precise phase metric, it is expected that the temperature drift of the compensated filter can achieve temperature drift similar to the compensated resonator.

The power handling capability of bimetal-compensated filters is studied in simulation. When subjected to high input power, the strength of the field surrounding the bimetal results in significant resistive heating. For a cantilevered bimetal compensator implemented in a 3-pole WR-62 waveguide filter, an increase in input power from $1\ \mathrm{W}$ to $100\ \mathrm{W}$ results in an increase in bimetal tip temperature of as much as $112\ ^\circ\mathrm{C}$.

The increase in bimetal temperature causes the temperature response to shift upward in frequency, and a negative shift in the temperature drift for a constant input power. The frequency drift of the cantilevered bimetal compensated filter is $+1357$ with input power ranging from $1\ \mathrm{W}$ to $100\ \mathrm{W}$ and external temperature ranging from $20\ ^\circ\mathrm{C}$ to $120\ ^\circ\mathrm{C}$. The drift of the filter degrades from -1.14 ppm/$^\circ\mathrm{C}$ with no input power, to -6.16 ppm/$^\circ\mathrm{C}$ at $100\ \mathrm{W}$ of input power.

In order to address the resistive heating problem, the compensator must conduct heat more effectively to the filter body. Using the proposed double-sided bimetal tuning screw, and using two compensators for each resonator, compensation can be achieved using a shorter effective bimetal length.

Using this configuration, the temperature increase at the bimetal tip is no more than $26\ ^\circ\mathrm{C}$. The drift of the filter shifts from 1.02 ppm/$^\circ\mathrm{C}$ with no input power, to 0.7 ppm/$^\circ\mathrm{C}$ at $100\ \mathrm{W}$ of input power. The frequency drift of the filter is $+277$ ppm with input power ranging from 1 W to 100 W and external temperature ranging from 20 °C to 120 °C. A comparable Invar filter will drift at approximately -1.6 ppm/°C, and an aluminum filter will drift at -23 ppm/°C.

The impact of implementing these temperature compensated filters would be significant. Temperature compensated aluminum filters offer substantial mass and cost savings over Invar filters. In satellite applications in particular, the mass savings associated with replacing Invar filters with temperature-compensated aluminum filters results in a large decrease in either launch costs or life cycle costs. Also, aluminum stock is less costly than Invar, and less expensive to machine.

This work has demonstrated that temperature-compensated aluminum filters using a bimetal tuning screw can be constructed that exhibit temperature drift comparable to that of an Invar filter. In high-power applications, the problems associated with local resistive heating can be managed if care is taken to ensure that the compensator can efficiently conduct heat through the bimetal to the filter body.

Compensation must be adjusted for each resonator in the filter. This work provides a method for adjusting compensation using either phase or group delay measurements. The phase metric is more precise than the group delay metric since flatness at the group-delay peak can make the measurement of resonance ambiguous. Also, group delay measurements are noisy.

Heating in the input cables however will introduce a positive shift to phase measurements, leading to unacceptable inaccuracy. The phase metric can therefore only be used when temperature-stable phase measurements can be taken; for example, using phase-stable silicone dioxide cables. Otherwise, the less precise peak group delay metric must be used to measure the resonance of each filter cavity.

The approach proposed here for adjusting compensation is useful for any form of variable compensation. This tool is useful for applying the compensation approach proposed here, or any other form of adjustable compensation.

To model temperature drift in the general case, interactions between microwave, structural, and thermal domains must be accounted for. This work proposes three multiphysics simulations for use in modelling temperature drift and power handling for microwave components in general. Each is implemented in the COMSOL Multiphysics software package.

Given the dimensional change from a thermo-mechanical simulation, a full-wave electromagnetic simulation must be solved on the deformed geometry. The arbitrary Lagrangian-Eulerian (ALE) method is designed to model fluid-structure interactions. It is used in this work to model the interaction between a structure and an electromagnetic field.

The first of these models describes thermal drift under uniform temperature conditions. This model can be used to simulate compensated or uncompensated temperature drift of a component under arbitrary mechanical constraints. The temperature drift behaviour under uniform-temperature conditions is used as a base-line performance measure.

The second multiphysics simulation presented in this work is a resistive heating simulation. This simulation determines the thermal effect of resistive heat flux on a component under arbitrary thermal boundary conditions. This simulation can be used to quantify local resistive heating, and can be used to detect and address problem areas for high-power applications.

The final multiphysics simulation is a resistively heated thermal-mechanical-RF simulation that provides a full accounting of electromagnetic performance, while accounting for the effect of local heating and mechanical constraint. This simulation provides not only the local resistive heating for given thermal boundary conditions, but accounts for the effect of this heating mechanically. The electromagnetic simulation is solved on the deformed geometry, so this simulation will predict how a component will behave thermally, mechanically, and electrically under complex thermal and mechanical conditions.

The analysis of the power handling of a bimetal-compensated filter in simulation demonstrates how a multiphysics approach can be used to model complex thermal, structural, and electrical interaction. Although finite element simulations have limitations in quantifying real-world implementations, by coupling thermal mechanical and electrical simulations real-world conditions can be more closely approximated, with the same advantages and disadvantages inherent in more traditional approaches to RF simulation.

In order to compensate for temperature drift, it is useful to be able to quantify uncompensated drift. In the case of a linearly expanding component having a single linear coefficient of thermal expansion, an equation describing temperature drift is derived from Maxwell's equations.

This equation is strictly true if losses are ignored, and approximately true in the lossy case. Also, the quality of the approximation in the lossy case depends on the coefficient of thermal expansion times the temperature change being much less than unity. Since this is true for temperature ranges and thermal expansion coefficients for most practical applications, the approximation inherent in applying this equation to the lossy case is justifiable.

An approximate model for the effect of iris expansion on coupling coefficient drift is provided which assumes that the coupling iris is thin. This model is used to evaluate the contribution of iris expansion to temperature drift using a lumped-element coupling-matrix model. It is demonstrated that the contribution of iris expansion to temperature drift is extremely small. For a coupled-resonator filter therefore, the effect of iris expansion can be effectively ignored.

A parameterized model for bimetal compensated resonators and filters is provided. Parameterized modelling requires a number of assumptions; among them uniform temperature distribution, unconstrained linear expansion, and a constant radius of curvature for the bimetal actuator. Where these assumptions are valid, the parameterized model proposed here is a useful technique for simulating temperature compensated designs using bimetallic elements.

It has been demonstrated that a bimetallic actuator mounted on a tuning screw can be used to compensate for temperature drift in coupled cavity waveguide filters. The resulting drift of the compensated filter using a bimetal tuning screw is comparable to that of an Invar filter where temperature change is driven by ambient conditions. It is therefore recommended that temperature compensated filters using bimetal tuning screws be deployed for low-power applications in lieu of Invar filters (e.g. terrestrial radio).

It has been shown in simulation that the effect of local resistive heating can be mitigated by using multiple compensators with shorter overall lengths. Future work should include confirming these results with high-power testing.

The performance of the proposed bimetal tuning screw under high-power conditions depends on how efficiently resistive heating is conducted to the filter walls. The work presented here shows that conduction can be substantially improved by reducing the length of each individual compensator. Future work in this area should include engineering a bimetal specifically for this application. Such a material must exhibit high flexivity, as well as high thermal conductivity.

Bibliography

[1] D. M. Pozar, *Microwave Engineering*, 2nd ed. John Wiley & Sons, Inc., 1998.

[2] I. C. Hunter, L. Billonet, B. Jarry, and P. Guillon, "Microwave filters-applications and technology," *IEEE Transactions on Microwave Theory and Techniques*, vol. 50, pp. 794–805, March 2002.

[3] H.-W. Yao and A. E. Atia, "Temperature characteristics of combline resonators and filters," *IEEE Digest on Microwave Theory and Techniques*, vol. 3, pp. 1475–1478, May 2001.

[4] C. Wang and K. A. Zaki, "Temperature compensation of combline resonators and filters," *IEEE Digest on Microwave Theory and Techniques*, vol. 3, pp. 1041–1044, June 1999.

[5] E. W. Weisstein. (2005, Feb.) Maxwell, James (1831-1879). [Online]. Available: http://scienceworld.wolfram.com/biography/Maxwell.html

[6] (2007, Jun.) World war II: The physicists' war. IEEE MTT-S. [Online]. Available: http://www.ieee-virtual-museum.org/exhibit/exhibit.php?taid=&id=159265&lid=1&seq=6

[7] H.-W. Yao, K. A. Zaki, A. E. Atia, and T. Dolan, "Improvement of spurious performance of combline filters," *IEEE Digest on Microwave Theory and Techniques*, vol. 3, pp. 1099–1102, June 1997.

[8] (2007, Jun.) Precursor to microwaves: Wireless and radio. IEEE MTT-S. [Online]. Available: http://www.ieee-virtual-museum.org/exhibit/exhibit.php?taid=&id=159265&lid=1&seq=5

[9] (2007, Jun.) Microwaves, satellites, and the final frontier. IEEE MTT-S. [Online]. Available: http://www.ieee-virtual-museum.org/exhibit/exhibit.php?taid=&id=159265&lid=1&seq=11

[10] C. Kudsia, R. Cameron, and W.-C. Tang, "Innovations in microwave filters and multiplexing networks for communications satellite systems," *IEEE Digest on Microwave Theory and Techniques*, vol. 40, pp. 1133–1149, June 1992.

[11] A. E. Williams, "A four-cavity elliptic waveguide filter," *IEEE Transactions on Microwave Theory and Techniques Symposium*, vol. 18, pp. 1109–1114, Dec 1970.

[12] A. E. Atia and A. E. Williams, "Narrow-bandpass waveguide filters," *IEEE Transactions on Microwave Theory and Techniques*, vol. 20, pp. 258–265, April 1972.

[13] R. D. Richtmyer, "Dielectric resonators," *Journal of Applied Physics*, vol. 10, pp. 391–398, June 1939.

[14] S. J. Fiedziusko, "Dual-mode dielectric resonator loaded cavity filters," *IEEE Digest on Microwave Theory and Techniques Symposium*, vol. 82, pp. 1311–1316, September 1982, issue: 9.

[15] P. L. Lui, "Passive intermodulation interference in communication systems," *Electronics & Communication Engineering Journal*, pp. 109–118, June 1990.

[16] D. E. Foster, "A new form of interference-external cross modulation," *RCA review: a quarterly journal of radio progress*, vol. 1, pp. 18–25, April 1937, issue 4.

[17] S. Hienonen, "Piezoceramic and SMA hysteresis modeling and compensation," Ph.D. dissertation, Rensselaer Ploytechnic Institute, 1997.

[18] B. Rosenberger, "The measurment of intermodulation products on passive components and transmission lines," *IEEE Digest on Microwave Theory and Techniques Symposium*, vol. 50, pp. 57–62, February 1995.

[19] C. Kunes, "Microwave multiplexers for space applications," *Electronics & Communications Engineering Journal*, vol. 10, pp. 29–35, February 1998, issue 1.

[20] G. Pfitzenmaier, “Synthesis and realization of narrow-band canonical microwave bandpass filters exhibiting linear phase and transmission zeros,” *IEEE Transactions on Microwave Theory and Techniques*, vol. 30, no. 9, pp. 1300–1311, September 1982.

[21] C. Vicente and H. L. Hartnagel, “Passive-intermodulation analysis between rough rectanglular waveguide flanges,” *IEEE Transactions on Microwave Theory and Techniques*, vol. 53, pp. 2515–2525, August 2005.

[22] A. E. Atia, “A 14-GHz high-power filter,” *IEEE Digest on Microwave Theory and Techniques Symposium*, vol. 79, pp. 261–261, April 1979, issue: 1.

[23] R. J. Cameron, H. Gregg, C. J. Radcliffe, and J. D. Rhodes, “Extracted-pole filter manifold multiplexing,” *IEEE Digest on Microwave Theory and Techniques Symposium*, vol. 30, pp. 1041–1050, July 1982.

[24] D. Rosowsky and D. Wolk, “A 450-W output multiplexer for direct broadcasting satellites,” *IEEE Digest on Microwave Theory and Techniques Symposium*, vol. 82, pp. 1317–1323, September 1982, issue: 9.

[25] M. Klauda, T. Kässer, B. Mayer, C. Neumann, F. Schnell, B. Aminov, A. Baumfalk, H. Chaloupka, S. Kolesov, H. Piel, N. Klein, S. Schornstein, and M. Bareiss, “Superconductors and cryogenics for future communication systems,” *IEEE Transactions on Microwave Theory and Techniques*, vol. 48, pp. 1227–1239, July 2000.

[26] E. R. Soares, J. D. Fuller, P. J. Marozick, and R. L. Alvarez, “Applications of high-temperature-superconducting filters and cryo-electronics for satellite communication,” *IEEE Transactions on Microwave Theory and Techniques*, vol. 48, pp. 1190–1198, July 2000.

[27] S. Chen, K. A. Zaki, and R. G. West, “A tunable, temperature compensated hybrid mode dielectric resonators,” *IEEE Digest on Microwave Theory and Techniques Symposium*, pp. 1227–1230, 1989.

[28] ——, “Tunable, temperature compensated dielectric resonators and filters,” *IEEE Transactions on Microwave Theory and Techniques*, vol. 38, no. 8, pp. 1046–1052, August 1990.

[29] A. Karp, H. J. Shap, and D. K. Winslow, “Circuit properties of microwave dielectric resonators,” *IEEE Transactions on Microwave Theory and Techniques*, vol. 16, no. 10, pp. 818–828, October 1968.

[30] S. Fiedziuszko and A. Jelenski, “Double dielectric resonator,” *IEEE Transactions on Microwave Theory and Techniques*, vol. 16, pp. 818–828, October 1971.

[31] G. L. Matthaei, “Comb-line band-pass filters of narrow or moderate bandwidth,” *Microwave Journal*, vol. 6, pp. 82–91, Aug. 1963.

[32] ——, “Interdigital band-pass filters,” *IRE Transactions on Microwave Theory and Techniques*, vol. MTT-10, pp. 479–491, Nov. 1962.

[33] G. Craven and C. K. Mok, “The design of evanescent mode waveguide bandpass filters for a prescribed insertion loss characteristic,” *IEEE Transactions on Microwave Theory and Techniques*, vol. MTT-19, no. 3, pp. 295–308, Mar. 1971.

[34] D. J. Small and J. A. Lunn, “Temperature compensated high power bandpass filter,” U.S. Patent 6 529 104, Mar. 4, 2003.

[35] ——, “Temperature compensated high power bandpass filter,” U.S. Patent 6 232 852, May 15, 2001.

[36] S. B. Lundquist, “Temperature compensated microwave filter,” U.S. Patent 815 223, Feb. 2, 1999.

[37] W. Fitzpatrick, M. Yu, D. Smith, and A. Sivadas, “Microwave resonator having an external temperature compensator,” U.S. Patent 6 535 087, Mar. 18, 2003.

[38] (2007, Nov.) Space wings kit - jameco’s robotstore. [Online]. Available: http://robotstore.com/store/product.asp?pid=1&catid=11

[39] (2007, Nov.) High strain sma actuator. [Online]. Available: http://www.cim.mcgill.ca/~haptic/pictures/SMA-Actuator.html

[40] B. F. Keats, “Temperature compensation for cavity resonators using shape memory alloys,” Master’s thesis, University of Waterloo, Waterloo, Ontario, 2003.

[41] B. F. Keats, R. R. Mansour, and R. B. Gorbet, “Shape memory alloy temperature compensation for resonators,” *IEEE Digest on Microwave Theory and Techniques Symposium*, vol. 2, pp. 1259–1262, June 2003.

[42] B. F. Keats, R. B. Gorbet, and R. R. Mansour, “Design and testing of SMA temperature-compensated cavity resonators,” *IEEE Transactions on Microwave Theory and Techniques*, vol. 51, pp. 2284–2289, December 2003.

[43] R. V. Basil, L. Ondrups, and J. K. Shimizu, “Thermally compensated microwave resonator,” U.S. Patent 4 057 772, Nov. 8, 1977.

[44] R. E. Jachowski and L. E. Brown, “Compensating device for tuned cavities,” U.S. Patent 4 423 398, Dec. 27, 1983.

[45] R. Kich, “Temperature compensated microwave resonator,” U.S. Patent 4 677 403, Jun. 30, 1987.

[46] H. Schmid and L. R. Mannerstrom, “Temperature-compensated tuning screw for for cavity filters,” U.S. Patent 5 039 966, Aug. 13, 1991.

[47] R. G. Thomson, “Collapsible pocket for changing the operating frequency of a microwave filter and a filter using the device,” U.S. Patent 6 049 261, Apr. 11, 2000.

[48] J. Webster, *Mechanical Variables Measurement*. CRC Press, 1999.

[49] S. Timoshenko, “Analysis of bi-metal thermostats,” *Journal of the Optical Society of America*, vol. 11, no. 3, p. 233, 1925.

[50] ASTM B 388, “Standard specification for thermostat metal sheet and strip,” *ASTM International*, vol. 02-04.

[51] DIN 1715-1, “Thermostat metals; technical delivery conditions.”

[52] (2006, May) Catalog of formulas. HOOD & Co, Inc. [Online]. Available: http://www.hoodandco.com/HOOD%5fFormulas.pdf

[53] (2006, May) Cantilever beam. Engineered Materials Solutions. [Online]. Available: http://www.emsclad.com/diagrams/tech/cantilever-beam.html

[54] (2006, May) How thermostat metal works. Engineered Materials Solutions. [Online]. Available: http://www.emsclad.com/tech.html

[55] J. E. Shigley and C. R. Michke, *Mechanical Engineering Design*, 5th ed. McGraw-Hill, Inc., 1989.

[56] C. A. Balanis, *Advanced Engineering Electromagnetics*. John Wiley & Sons, Inc., 1989.

[57] *COMSOL reference manual*, COMSOL, Inc., Stockholm, Sweden, 2007, version 3.3a.

[58] G. L. Matthaei, L. Young, and E. M. T. Jones, *Microwave filters, impedance-matching networks, and coupling structures*. McGraw Hill, 1964.

[59] S. B. Cohn, "Direct-coupled-resonator filters," *Proc. IRE*, vol. 45, pp. 187–196, February 1957.

[60] P. Couffignal, H. Baudrand, and B. Théron, "A new rigorous method for the determination of iris dimensions in dual-mode cavity filters," *IEEE Transactions on Microwave Theory and Techniques*, vol. 42, no. 7, pp. 1300–1311, July 1994.

[61] (2007, Aug.) Clad metal from engineered materials solutions. Engineered Materials Solutions. [Online]. Available: http://www.cladit.com

[62] H. Jiandong, S. LIang, L. ShunZhou, M. QingDuan, Z. Qiang, L. Fei, Z. XueQiang, L. ChungGuang, H. AiSheng, L. Hong, G. ChangZhi, L. Qiang, S. QinFen, W. XiaoLin, S. YiFan, W. ZhiBing, W. YunFei, L. Sheng, and H. YuSheng, "Space qualification mechanical tests of hts filters for satellite application," *Chinese Science Bulletin*, vol. 52, no. 13, pp. 1771–1775, July 2007.

[63] (2007, Sep.) Benchtop environmental test chambers microclimate® from cincinnati sub-zero. Cincinnati Sub-Zero. [Online]. Available: http://www.cszindustrial.com/products/microclimate/microclimate.htm

[64] (2007, Sep.) Agilent | technical support overview: 8722es s-parameter vector network analyzer. Agilent. [Online]. Available: http://www.home.agilent.com

[65] (2007, Sep.) Virtual network computing | wikipedia, the free encyclopedia. Wikipedia. [Online]. Available: http://en.wikipedia.org/wiki/VNC

[66] (2007, Sep.) Windows xp: Get started using remote desktop. Microsoft.

[67] J. B. Ness, "A unified approach to the design, measurment and tuning of coupled-resonator filters," vol. 46, no. 4, pp. 343–351, Apr. 1999.

[68] T. Nomura and T. J. R. Hughes, "An arbitrary Lagrangian-Eulerian finite rigid element method for interaction of fluid and a rigid body," *Computer Methods in Applied Mechanics and Engineering*, vol. 95, no. 1, pp. 115–138, 1992.

[69] D. Peyrou, P. Pons, H. Granier, D. Leray, A. Ferrand, K. Yacine, M. Saadaoui, A. Nicolas, J. Tao, and R. Plana, "Multiphysics Softwares Benchmark on Ansys/Comsol Applied For RF MEMS Switches Packaging Simulations," *Thermal, Mechanical and Multiphysics Simulation and Experiments in Micro-Electronics and Micro-Systems, 2006. EuroSime 2006. 7th International Conference on*, pp. 1–8, 2006.

[70] R. R. Mansour, B. Jolley, S. Ye, F. S. Thomson, and V. Dokas, "On the power handling capability of high temperature superconductive filters," vol. 44, pp. 1322–1338, Jul. 1996.